



ALMA MATER STUDIORUM
UNIVERSITÀ DI BOLOGNA

DOTTORATO DI RICERCA IN

FISICA

Ciclo 37

Settore Concorsuale: 02/B1 – FISICA SPERIMENTALE DELLA MATERIA

Settore Scientifico Disciplinare: FIS/03 – FISICA DELLA MATERIA

**INNOVATIVE 2D MATERIALS FOR REDUCING
FRICTION IN TRIBOLOGICAL SYSTEMS:
AB INITIO SIMULATIONS COUPLED WITH EXPERIMENTS**

Presentata da: Edoardo Marquis

Coordinatore Dottorato

Prof. Alessandro Gabrielli

Supervisore

Prof. M. Clelia Righi

Esame finale anno 2025

Acknowledgements

I am deeply grateful to my supervisor, Prof. Clelia Righi, for her guidance and encouragement throughout this long journey. I am sincerely thankful for her support and for always pushing me to strive for excellence. I would also like to thank all my colleagues for the stimulating discussions and the collaborative spirit we shared. Working alongside such talented and dedicated individuals has enriched my research experience and challenged me to grow both as a researcher and as a person. The countless hours spent in discussions and debates, both in the office and beyond, make me feel incredibly lucky to have been part of such an inspiring group. Grazie a Pacio, Vito, Fra, Matte, Enri, Eli, Mike, Ste, Mauro, Paolo, Marghe.

I must extend my gratitude to Prof. Carsten Gachot, who supervised me during my six-month research stay at TU Wien. His guidance, expertise, and encouragement played a pivotal role in the success of my PhD. I am especially grateful for the genuine friendship he extended to me, which made my time in Vienna both professionally rewarding and personally enriching. I also owe a huge thank you to all my colleagues at TU Wien. The time we shared, both in and outside the lab, was invaluable. Our stimulating discussions, collaborative spirit, and unforgettable moments made my stay an essential part of my PhD journey. Thank you for making Vienna feel like a second home. The success of this journey is undoubtedly thanks to you: Hakan, Hanglin, Iris, Xudong, Christina, Philipp, Stefan, Martin. I feel immensely lucky to have met you.

The PhD period has been extremely stimulating and challenging. Lab teaching, student supervision, and conference talks have been the most enriching activities for me. I am truly grateful to all the people I had the chance to discuss things with: your curiosity and enthusiasm have been a source of motivation for me. However, my PhD period has not been all puppy dogs and rainbows. I must admit that I have found the immense pressure to publish, secure funding and compete in a brutally competitive landscape to be overwhelming. Doing a PhD means facing mental health struggles, with anxiety and depression knocking at the door almost every day. I have witnessed firsthand how such constant pressure can erode humanity, cooperation, and even critical thinking, which I always believed to be the foundation of scientific advancement. Saddest of all, I no longer find this surprising, it's simply a reflection of the inhumane era we are living in, where personal profit is valued more than people's well-being. This is why I want to thank all of my friends, who have been a constant pillar of support throughout this challenging period. I don't know the right words to express how much I love you, and I hope there is no need for that. The love you have given me has been essential in helping me shape the proper mindset throughout my professional journey. While society continues to judge me based on my "numbers", you have shattered this false metric and pushed me to be a better human being. The moments we shared hold a special place in my heart, and I believe they represent the true success of my PhD journey.

A Caro, Ale, Ma e Pa, siete parte di me. Provo per voi amore incondizionato, siete il mio sostegno incrollabile. Sarò per sempre infinitamente grato per tutto ciò che avete fatto per me. Dedico a voi ogni successo, frutto della fiducia che mi avete sempre trasmesso.

Thank you all for being part of this journey.



ALMA MATER STUDIORUM
UNIVERSITÀ DI BOLOGNA

Contents

Abstract	2
1. Theoretical Background.....	3
1.1 What is Tribology?	3
1.1.1 Historical Background	4
1.1.2 Fundamental concepts	5
1.2 Materials to reduce friction	8
1.2.1 Liquid Lubrication	8
1.2.2 Solid Lubrication	9
1.3 Density Functional Theory (DFT) applied to Tribology.....	16
2. Tribological properties of Ti-based MXenes by DFT simulations	19
2.1 Introduction	19
2.2 Methods	20
2.2.1 The zoo of dispersion correction methods.....	24
2.3 Results and Discussion.....	26
2.3.1 Characterization of interlayer slipperiness	26
2.3.2 Adhesion to ferrous substrates	32
2.3.3 The problem of water-induced oxidation	35
2.3.4 MXene hydrophilicity – effect of defects and edges.....	36
2.4 Conclusions	44
3. Synergistic effect of MXene-MoS composite coating	46
3.1 Introduction	46
3.2 Methods	47
3.3 Results and Discussion.....	51
3.3.1 DFT predicted adhesion behavior	51
3.3.2 Solid lubrication performance	53

3.3.3 Experimental characterization of hybrid interface.....	54
3.4 Conclusions	61
4. In Operando formation of Transition Metal Dichalcogenides (TMDs)	63
4.1 Introduction	63
4.2 Methods	65
4.3 Results and Discussion.....	67
4.3.1 An innovative lubrication method.....	67
4.3.2 Tribofilm characterization - MoSe ₂ and WSe ₂ formation	69
4.3.3 Mechanistic insights: Ab Initio Molecular Dynamics (AIMD)	72
4.4 Conclusions	75
5. Transition Metal Carbo-Chalcogenides (TMCCs) as solid lubricants.....	77
5.1 Introduction	77
5.2 Methods	79
5.3 Results and Discussion.....	82
5.3.1 Characterization of the TMCCs	82
5.3.2 Tribological performance	83
5.3.3 Tribofilm characterization.....	87
5.3.4 Interlayer sliding by DFT simulations	92
5.4 Conclusions	94
6. Final remarks and future perspectives.....	97
Bibliography.....	100

Abstract

Tribology, the science of friction, wear, and lubrication, plays a crucial role in improving energy efficiency across industrial and everyday applications. Controlling friction can lead to significant energy savings, as friction and wear contribute to nearly 20% of global energy consumption. Advances in tribology, particularly through innovative materials, offer substantial economic and environmental benefits, making it essential for technological progress and sustainability. Lubrication technologies rely on both liquid and solid lubricants. While liquid lubricants, such as synthetic oils, form protective films to reduce friction, they may fail under extreme conditions like high temperatures or vacuum. In such cases, solid lubricants, including graphite, diamond-like carbon (DLC), and transition metal dichalcogenides (TMDs) like MoS_2 and WSe_2 , provide a more effective solution. These layered materials facilitate low-shear interlayer sliding, making them ideal for aerospace and precision engineering. Emerging 2D materials, such as MXenes and Transition Metal Carbo-Chalcogenides (TMCCs), combine mechanical strength with self-lubrication, representing a promising frontier in tribology. Computational simulations, particularly quantum mechanical approaches, play a pivotal role in understanding tribological phenomena at the atomic level. These methods allow for the study of interlayer sliding, adhesion, oxidation, and tribochemical reactions, guiding the design of new lubricant materials while reducing experimental costs.

This thesis explores the tribological properties of advanced 2D materials through a combination of simulations and experiments. It investigates (i) the frictional behavior of titanium-based MXenes via density functional theory (DFT), (ii) the synergy between MXene- MoS_2 composite coatings, (iii) the in-operando formation of MoSe_2 and WSe_2 lubricious layers from selenium nanoparticles, and (iv) the promising tribological performance of TMCCs ($\text{Nb}_2\text{S}_2\text{C}$ and $\text{Ta}_2\text{S}_2\text{C}$). These findings contribute to the development of next-generation solid lubricants for demanding applications.

Chapter 1

1. Theoretical Background

The first chapter aims to overview the most relevant aspects of tribology, introducing the reader to this fascinating topic that permeates our everyday experience. After a brief summary of fundamental concepts, including common strategies to control friction, the role of numerical simulations will be examined. By the end of the chapter, the motivation for this dissertation will be made clear.

1.1 What is Tribology?

Tribology is defined as “the science of friction, lubrication, and wear phenomena, which occur whenever interacting surfaces are in relative motion”.¹ From this definition, the ubiquity of tribology in daily life becomes immediately evident: from the friction between our shoes and the ground as we walk, to the interaction of gears in machines, or the movement of engine components in a car. Without friction, fundamental activities like riding a bike, driving a car, or even writing with a pen would be impossible. Indeed, tribology permeates and enables our everyday lives, governing processes on Earth long before humans appeared. Natural phenomena such as water and wind erosion, which gradually wear down the Earth's surface, or earthquakes caused by the buildup of friction until tectonic plates shift, are prime examples of tribology in action.

Tribology has been the subject of documented studies and measurements for over half a millennium, but the term 'tribology' has a surprisingly recent origin. The word comes from the Greek 'τρίβος' (tribos), meaning “rubbing”. It was first introduced in a 1966 report by Peter Jost, who chaired a group of British lubrication engineers, highlighting the significant economic impact of friction, wear, and corrosion on the UK economy.² Nearly 60 years later, the economic implications of tribology remain a topic of debate. On a global scale, K. Holmberg and A. Erdemir estimated that friction and wear account for about 20% of the total energy produced.³ Even more strikingly, they predict that implementing new tribological solutions in road transport alone could reduce energy consumption by up to 17.5%, saving 11.6 exajoules of energy annually, 330 billion liters of fuel, and reducing CO₂ emissions by 860 million tonnes.⁴

Despite its apparently simple definition, tribology remains one of the most challenging areas of science, requiring a highly interdisciplinary approach that encompasses physics, chemistry, materials science, mathematics, biology, and engineering. Although friction is a constant presence in everyday life, its mechanisms under varying conditions remain unclear, as does our ability to accurately predict and control them. The complexity of frictional systems, influenced by many interacting variables, makes it difficult to develop a universal

theory. Instead, tribology often requires a case-by-case approach. In the following sections, I will present the main concepts of tribology, quickly retracing the scientists and technologies that contributed to their development.

1.1.1 Historical Background

Smart solutions to friction problems have been employed since the dawn of human history. One of the most famous examples is a drawing found in a grotto at El Bersheh in Egypt, dating back to around 1880 BC. It depicts a large colossus being hauled by numerous rows of slaves. In the illustration, a small figure is shown pouring a liquid, likely animal fat, onto wooden rollers to aid in the movement of the massive sledge carrying the statue.¹ The first systematic studies on dry friction, however, are attributed to Leonardo da Vinci (1452–1519). Da Vinci sketched various apparatuses designed to study sliding friction, although he never explicitly mentioned the term "friction force" in his notes. Since his studies were unpublished, they remained unknown for nearly two centuries until the rise of modern science.

The first two classical "laws of friction", typically credited to Guillaume Amontons in 1699, state that i) the force of friction is directly proportional to the applied load, and ii) the force of friction is independent of the apparent contact area. While these laws are not universally applicable, especially in extreme conditions like high speeds or varying normal loads, they have been foundational in understanding the behavior of machines. In 1750, Leonhard Euler, in his article "*Sur le frottement des corps solides*", clarified the distinction between static and kinetic friction, showing that the kinetic friction coefficient is much lower than the static one. The use of the Greek symbol mu (μ) for the friction coefficient is in fact credited to Euler. A few years later, in 1785, Charles Augustin de Coulomb experimentally validated Amontons' laws and investigated the dependence of friction on time, velocity, material properties, contact area, normal pressure and humidity in his timeless book titled "*Théorie des machines simples en ayant égard au frottement de leurs parties et à la roideur des cordages*". He also proposed that friction originates from microscopic asperities and the cohesion between surfaces, laying the groundwork for the theory of dry friction, which is still referred to as "Coulombic friction" in modern literature.¹

With the industrial revolution of the 18th and 19th centuries came an increasing number of practical friction challenges (especially in transportation technologies), highlighting the need for more effective friction control. Significant advancements were made in the late 1800s in the theory and application of lubricants. In particular, Osborn Reynolds⁵ and Richard Stribeck^{6,7} contributed to the understanding of liquid lubrication, leading to the introduction of the Stribeck curve. By the 1900s, tribological studies were further advanced by new instruments capable of examining friction, and scientists began to consider the role of adhesion and surface chemistry. In the 1950s, Frank Philip Bowden and David Tabor introduced concepts such as the real area of contact, adhesive friction, and wear, linking macro- and microscopic friction phenomena.^{8,9}

From the mid-20th century, with the development of commercial electron microscopes, tribology experienced rapid progress. New experimental techniques, such as atomic force microscopy (AFM),¹⁰ allowed for the study of surfaces and interfacial layers at the atomic scale. Additional methodologies, such as Auger Electron Spectroscopy (AES)¹¹ and X-ray Photoelectron Spectroscopy (XPS),¹² enabled the post-mortem analysis of tribological samples and thin films on surfaces (“tribofilm”). These advancements have given rise to new areas of tribology, such as *nanotribology* (the study of friction, wear, and lubrication at the nanoscale, with applications in micro- and nano-electromechanical systems and magnetic storage) and *biotribology* (focused on human joint prosthetics, dental materials, and skin). Additionally, the discovery of *superlubricity*,¹³ e.g. extremely low friction with a kinetic coefficient of friction $\mu_k < 0.01$, has raised hopes for significant energy savings. The advent of computational technologies has provided powerful tools for predictive and explanatory modeling. Today, computational methods enable the study of tribological phenomena across different time and length scales, using techniques such as finite element methods, boundary element methods, atomistic methods, and multiscale approaches.¹⁴ Details on atomistic methods, particularly in the context of Density Functional Theory (DFT), are discussed in Section 1.3.

1.1.2 Fundamental concepts

In this chapter, I will introduce the fundamental concepts and physical quantities related to tribology, i.e. the study of friction, wear, and lubrication. These phenomena arise from surfaces in contact, moving relative to each other under an external load. Surfaces are particularly challenging to study for two main reasons: (i) they consist of multiple layers with physical and chemical properties different from the bulk material, and (ii) they evolve over time, often undergoing significant microstructural changes in subsurface regions. **Figure 1.1** illustrates the complexity of a generic surface.

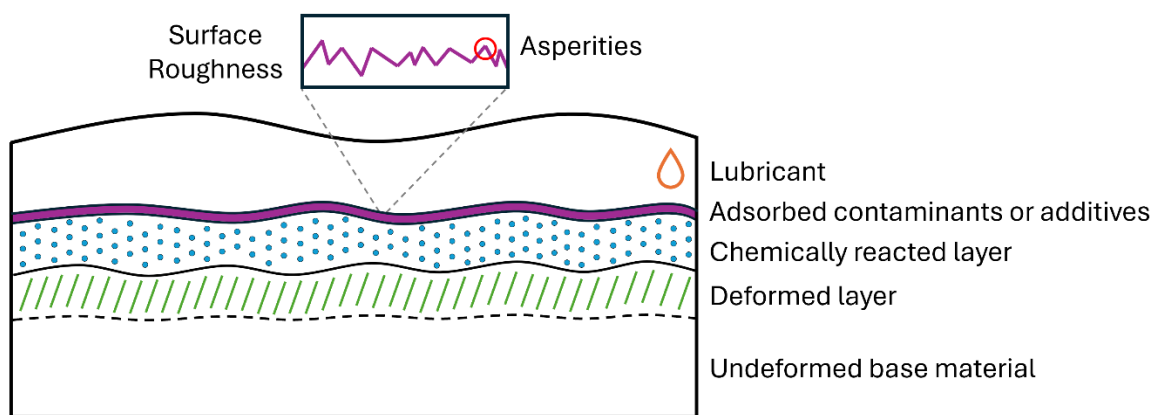


Figure 1.1: Schematic illustration of the complexity of a generic surface, highlighting the various layers involved in tribological phenomena. The scales range significantly, from the macroscale of the undeformed base material to the nanoscale of the adsorbed layer.

Macroscopic properties, such as hardness or strength, describe only the undeformed bulk material, but there are several layers on top of the bulk that form/erode during tribological processes. For instance, metallic surfaces often develop a passivating oxide layer, which has mechanical, chemical, and physical properties distinct from the metal underneath. Contact and friction with another surface can wear away these oxides, releasing particles that may either be removed or reincorporated into the surface layers, forming what tribologists call a chemically reacted layer or *tribofilm*. Similarly, contaminants from the environment or lubricants (e.g., lubricant additives) can contribute to tribofilm formation. The chemical reactions between lubricants or environmental molecules and surfaces in motion under load are known as *tribochemical reactions*. The complexity of a surface is not limited to its composition, as shown in **Figure 1.1**, but also includes its topography. No surface is perfectly smooth: even highly polished surfaces retain a degree of roughness. *Surface roughness* is a fundamental parameter in tribology, influencing the shape and density of asperities, which determines the real contact area between surfaces and the real contact stresses. The real area of contact (A_r) at the asperity level is typically 10^{-2} to 10^{-6} times smaller than the apparent area (A_a) measured macroscopically, depending on surface topography. Consequently, even low apparent stress can generate localized stresses that exceed the elastic limit at the asperity tips, causing localized plastic deformation.

The inevitable presence of asperities significantly affects tribological processes at the buried interface, often governing friction and wear. Friction arises from the resistance to relative motion between asperities in contact. This resistance stems from adhesion forces (electrostatic, van der Waals, or metallic bonds that may cause cold welding) and mechanical forces (elastic and plastic deformation). When studying friction, scientists measure the coefficient of friction (μ or COF), which is defined by Amontons' law as a constant of proportionality between the friction force and the applied load:

$$F_{\text{friction}} = \mu F_{\text{load}}$$

Despite this straightforward definition, the COF is far from being a “constant”. Even in simple tribological systems, such as steel-on-steel contacts, it is impossible to assign a specific COF value. This is because the COF is not a material property but rather a characteristic of the entire tribological system. Factors such as surface roughness, contact stress, sliding mode, velocity, temperature, environmental conditions, and whether the contact is lubricated or dry, they all influence the COF. For steel-on-steel, for example, the COF can range from 0.1 to 0.8, depending on these variables.

Like friction, wear is conceptually simple: it refers to the removal (or displacement) of material from one surface when in contact and relative motion with another. Tribologists aim to minimize wear by reducing wear volume and studying the wear mechanisms. Wear is typically quantified by weight loss and wear rate. While several equations describe wear volume, Archard's wear equation is the most widely used:

$$W_{\text{volume}} = k \frac{F_{\text{load}} \cdot d_{\text{sliding}}}{H}$$

where k is the wear coefficient, F_{load} is the normal load, d_{sliding} is the sliding distance, and H is the hardness of the softer material. To facilitate comparison, wear volume is often normalized with respect to the normal load and sliding distance. The most common wear modes are abrasive wear, where a harder material removes material from a softer one, and adhesive wear, where two surfaces adhere through cold welding. Other wear modes include fatigue wear (from rolling or impact), erosive wear, and fretting corrosion. These mechanisms often occur simultaneously, making wear measurements subject to high uncertainty.

So far, I have discussed friction and wear in dry contacts, mainly governed by asperity interactions. However, as we know from everyday experience, lubrication is key to reducing friction and preventing (or minimizing) wear. Since the late 1800s, extensive research has focused on lubricated friction, examining relationships between the coefficient of friction and variables such as speed, load, and lubricant viscosity. Tribologists use the Stribeck curve (shown in **Figure 1.2**) to classify lubrication regimes.

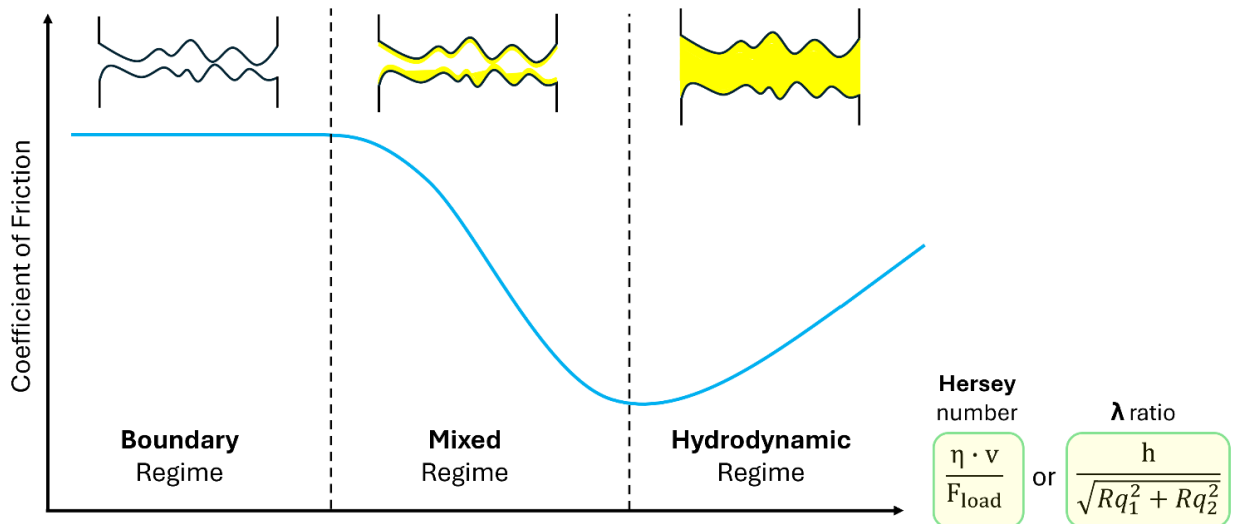


Figure 1.2: Example of Stribeck curve highlighting the three lubrication regimes: boundary lubrication, mixed lubrication and hydrodynamic.

The x-axis of the Stribeck curve, also known as the Hersey number, combines multiple factors: η is the lubricant viscosity, v is the entrainment speed, and F_{load} is the applied normal load. Since load and viscosity are usually kept fixed during experiments, the curve may also be intended as a COF against velocity plot. Alternatively, it can be viewed as COF versus the lambda ratio, defined as the ratio between the lubricant film thickness (h) and the root mean square of the surface roughness (Rq). According to the Stribeck curve shown in **Figure 1.2**, three lubrication regimes can be distinguished. In the *boundary lubrication* regime, low speeds and high loads lead to high friction coefficients as the lubricant is squeezed out, allowing asperities to come into contact. As lubrication conditions improve (e.g., reduced normal load), the lubricant film thickens, transitioning into the *mixed lubrication* regime,

where some asperities still make contact while part of the load is supported by the lubricant. As the film thickness increases further, the COF reaches a minimum, marking the onset of the *hydrodynamic* regime, in which a full lubricant film carries the load, preventing direct asperity contact. In this regime, the increase in friction with velocity is due to viscous shear within the lubricant. Having introduced the fundamentals of friction, wear, and lubrication, the next chapter will explore common strategies based on materials for reducing friction. After an overview, I will focus on solid lubricants, with particular attention to two-dimensional materials, the main subject of this thesis.

1.2 Materials to reduce friction

The term *lubricant* refers to any substance that reduces friction and wear while ensuring a satisfactory operational lifetime for a tribosystem. Lubricants can exist in solid, semi-solid, or even gaseous states depending on the system and application, but the majority are liquids.¹⁵ Besides reducing friction and wear, liquid lubricants also dissipate frictional heat, transport wear debris, and mitigate corrosion.¹⁶ Their efficiency in reducing friction is 1 to 3 orders of magnitude greater than that of solid lubricants.¹⁷ However, the use of conventional oils can be environmentally unfriendly, potentially toxic, or restricted due to physical limitations, particularly under extreme conditions (e.g., high temperatures, vacuum). In contrast, solid lubricants have gained considerable attention for their excellent friction and wear properties under such challenging conditions.¹⁸ This chapter provides a general overview of both liquid and solid lubricants, along with an introduction of the latest advancements in the design of two-dimensional (2D) layered materials for friction reduction.

1.2.1 Liquid Lubrication

Modern liquid lubricants typically consist of two primary components: a base fluid and a range of functional additives. The base fluid, which can be mineral oil, synthetic oil, or bio-based oil, provides essential lubrication properties such as viscosity and heat dissipation. However, base fluids alone often fall short of meeting the demanding requirements of high-performance systems, especially under extreme conditions like high or shock loads, elevated temperatures, slow rotation, or variable speeds. To enhance the performance of the base fluid, functional additives are incorporated into the formulation. These additives can either modify the lubricant's inherent properties or introduce new capabilities, as summarized below:^{15,19}

- *Antioxidants*: to delay the aging process caused by the oxidation of base fluid molecules (e.g., organosulfur and organophosphorus compounds).²⁰
- *Viscosity modifiers*: that influence the viscosity-temperature relationship of the lubricant, minimizing viscosity changes due to temperature fluctuations (e.g., functionalized polymers,²¹ olefin copolymers).

- *Antiwear (AW) and extreme pressure (EP) additives*: these form protective tribolayers on surfaces, preventing direct contact and wear (e.g., zinc dialkyl dithiophosphates - ZDDP²², molybdenum dialkyldithiocarbamate - MoDTC^{23,24}).
- *Friction modifiers*: which create lubricating tribofilms at the interface of sliding surfaces (e.g., organic friction modifiers derived from fats and vegetable oils,²⁵ oil soluble organomolybdenum compounds,²⁶ and dispersed nanoparticles²⁷).
- *Detergents and dispersants*: they prevent material deposition on metal surfaces and the formation of larger particles due to agglomeration.²⁸

In practical applications, lubricants are tailored according to the lubrication regime they are intended for (boundary, mixed, or hydrodynamic lubrication, see **Figure 1.2**). In the hydrodynamic regime, the primary concern is the lubricant's viscosity, as the lubricant film must be thick enough to fully separate the surfaces. High molecular weight polymers are commonly used as additives in this context, boosting the lubricant's film-forming capacity. In contrast, in the boundary and mixed lubrication regimes, where direct surface contact increases the risk of wear and friction, friction modifiers and anti-wear agents are essential.²⁶ These additives function by adsorbing onto the surface or forming protective tribofilms to prevent metal-to-metal contact.

1.2.2 Solid Lubrication

Solid lubricants become essential when operating conditions exceed the limits of liquid lubricants, such as in high-temperature environments or vacuum, or when liquids cannot be used, for instance, in surfaces under reciprocating motion where liquid lubricants are squeezed out.²⁹ With advancements in modern coating technologies, such as physical vapor deposition (PVD), chemical vapor deposition (CVD), and plasma-enhanced CVD, the efficiency and durability of solid lubricant coatings have significantly improved.³⁰ There are three main classes of solid lubricant materials commonly employed in industrial applications:

- Carbon-based materials, such as graphite and diamond-like carbon (DLCs).
- Polymeric composite coatings, including PTFE and PEEK.
- Transition Metal Dichalcogenides (TMDs), such as MoS₂ and WS₂.

Each class is discussed in a dedicated subsection of this chapter, in which their applications and functionalities are presented. Typically, solid lubricant coatings in tribological contacts result in the formation of a tribofilm, which can transfer from the coating's surface to the countersurface (transfer-film).³¹ The formation of such passivating tribofilm depends on stress-induced microstructural changes and tribochemical reactions with surrounding environmental molecules. Thus, factors such as environment, load, countersurface material, and sliding speed play a crucial role in determining the tribological performance of solid lubricants.^{31–34} For example, a coating with an exceptionally low

coefficient of friction (COF) and long wear life in one environment may fail to perform under different conditions.

In this context, research into solid lubrication follows a dual approach: extending the operational range of existing materials while also designing and developing new materials for tribological applications. In recent decades, materials scientists have synthesized new families of two-dimensional (2D) materials, including MXenes^{35–39} and Transition Metal Carbo-Chalcogenides (TMCCs).^{40,41} These 2D materials are promising candidates for solid lubrication due to their layered crystal structures, where strong intra-plane bonds exist, but the layers are weakly connected by van der Waals forces. Investigating the tribological performance of these novel 2D materials is the central topic of this thesis, and therefore, MXenes and TMCCs are discussed in detail within this introduction.

1.2.2.1 Carbon-based Materials

Carbon-based materials are among the most efficient and versatile solid lubricants because carbon can show a huge variety of chemical structures, such as graphite/graphene and diamond-like carbon (DLC).

Graphite exhibits a layered structure, with sp^2 -hybridized carbon atoms forming a hexagonal honeycomb structure. The carbon atoms within the basal planes are held together with strong covalent bonds, whereas the interaction between graphite layers, i.e. 2D graphene layers, is mainly driven by van der Waals forces, which allow easy shear capability. The presence of environmental species like water and oxygen are essential to facilitate the interlamellar shearing of graphite crystals.^{42–44} Indeed, graphite lamellae need moisture or adsorbed gases to passivate the dangling bonds of their high-energy edge sites.⁴⁵ Under vacuum conditions, graphite/graphene lose their lubricant properties since the reactive edge sites of the basal planes strongly bond each other during the tribological process, leading to increased friction.

DLC coatings are a large family of amorphous films characterized by low friction coefficients and low wear rates, relatively high hardness, and high elastic modulus.³¹ DLCs are defined according to the sp^3 - sp^2 -type bonding and degree of hydrogenation, as depicted in the ternary phase diagram shown in **Figure 1.3**. Depending on the hydrogen content, DLCs are classified into two main domains:

- DLCs that are hydrogen-free or that contain a negligible amount of H include *amorphous carbon* (a-C), which mostly presents sp^2 -type trigonal bonding typical of graphitic hybridization, and *tetrahedral amorphous carbon* (ta-C), showing a higher sp^3 content, i.e., tetrahedral bonding (see left axis of Figure 1.3). The best performance for these coatings is observed under humid air. Similarly to graphene, in fact, H_2O molecules can dissociate and passivate the dangling bonds of a-C and ta-C, thus reducing friction and wear during rubbing.⁴³

- Hydrogenated DLC coatings have a variable amount of H (between 10% and 50%), including *tetrahedral amorphous hydrogenated carbon* (ta-C:H) as well as *amorphous hydrogenated carbon* (a-C:H). These hydrogenated coatings do not need bond-passivation from humidity, thus showing better performance in dry (or inert gas) environment.³¹

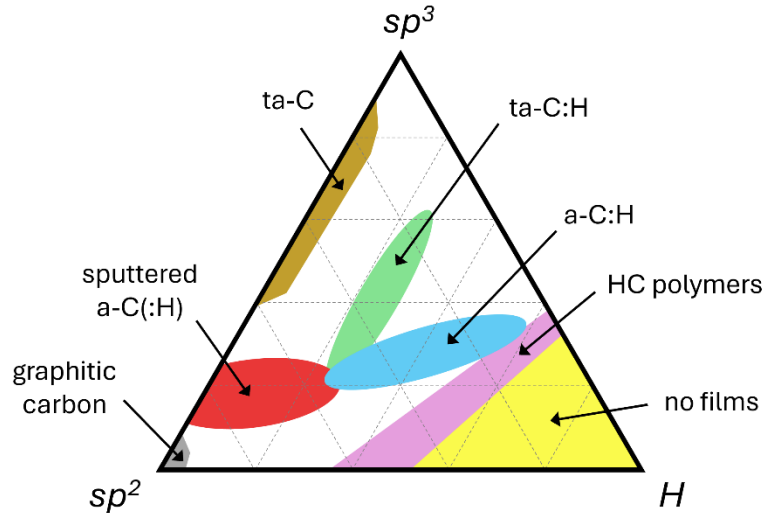


Figure 1.3: Phase diagram of DLC materials, considering carbon hybridization and hydrogen content.

Notice that if the hydrogen content is too high (bottom right of Figure 1.3), the material cannot form a fully connected network, and no film can be formed. In this short summary, only non-doped DLCs have been presented, although they may also be doped with metals (Cr, W, Ti) or lightweight elements (N, F, Si) to form nanoscale hard metal carbide phases, which improve the mechanical strength, hardness, and wear resistance.³¹ DLC coatings are commonly used in several industrial applications, including automotive, aerospace, electronics, optics, as well as for medical equipment.⁴⁶

1.2.2.2 Polymeric Materials

Polymer-based coatings, such as polytetrafluoroethylene (PTFE), polydimethylsiloxane (PDMS), polyetheretherketone (PEEK), polyimide (PI), and polyphenylene sulfide (PS), have gained significant attention as solid lubricants across various industrial applications. Due to their inherently low coefficients of friction, low shear strength, and low elastic modulus, polymeric materials are particularly favored in applications where low cost, light weight, corrosion resistance, and biocompatibility are crucial factors.⁴⁷ However, compared to hard coatings like ceramic and carbon-based coatings, polymers generally exhibit weaker wear resistance and shorter lifespans. To address these limitations, polymers are often used in multi-component materials to enhance their mechanical and physical properties. The addition of fillers to a polymeric matrix can greatly improve its tribological and mechanical

performance.⁴⁸ For example, PTFE exhibits an exceptionally low coefficient of friction in both vacuum and atmospheric conditions, thanks to its chemical inertness and self-lubricating properties. However, using PTFE alone results in unacceptably high wear.⁴⁹ By incorporating other fillers into the PTFE matrix, its wear resistance can be significantly enhanced.^{50–52}

An emerging issue concerning PTFE and fluorinated materials in general must be considered for the near future: the European Chemicals Agency (ECHA) is planning to ban perfluorinated and polyfluorinated alkyl substances (PFAS). This ban is driven by studies showing that PFAS contribute to soil and drinking water contamination, with certain PFAS compounds classified as persistent, bioaccumulative, and/or toxic.⁵³ Even during waste incineration, some of these substances cannot be fully degraded, as they are destroyed only at temperatures above 1000 °C. With the impending ban on PFAS-based products like PTFE, there is a need to explore alternative solid lubricant candidates with promising properties.

1.2.2.3 Transition Metal Dichalcogenides (TMDs)

Transition Metal Dichalcogenides (TMDs) are a class of layered materials with the chemical formula MX_2 , where M represents a transition metal (e.g., Mo, W, Re, Nb) and X is a chalcogen (e.g., S, Se, Te). The lubrication mechanism of two-dimensional (2D) TMDs is closely tied to their crystal structure, which consists of X-M-X layers that weakly interact with each other via van der Waals forces. This characteristic 2D structure, depicted in **Figure 1.4**, is responsible for the low shear strength and intracrystalline slip between layers.

Among the various TMDs, molybdenum disulfide (MoS_2) and tungsten disulfide (WS_2) are the most widely used for industrial solid lubricant applications.⁵⁴ Both materials exhibit excellent self-lubricating properties in high vacuum and dry environments, making them ideal for many space applications.⁵⁵ It is generally accepted that the primary lubrication mechanism of TMDs involves the creation of (0002) basal planes, which eventually re-orient parallel to the sliding direction, followed by the formation of a transfer film on the counterbody to facilitate interfacial sliding.³¹

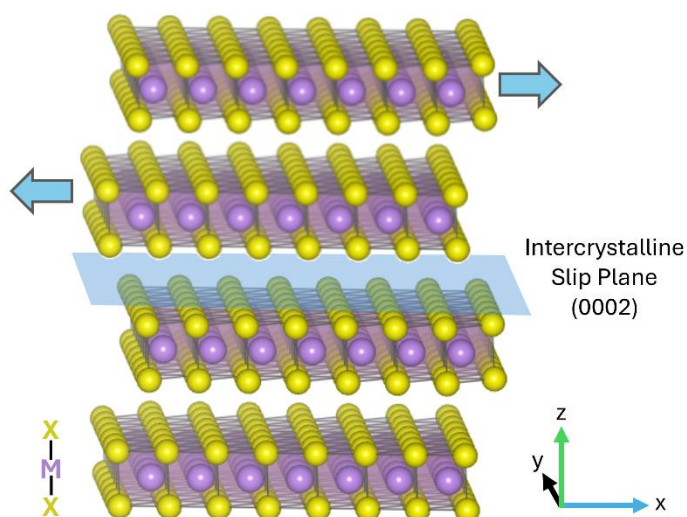


Figure 1.4: 2D TMD layers in an X-M-X sandwich-like structure, interacting via weak van der Waals forces.

Both MoS_2 and WS_2 coatings demonstrate extremely low friction coefficients ($\mu < 0.05$, with the potential for achieving superlubricity) and long wear life (lasting for several million sliding cycles), but only in high vacuum and dry environments.⁵⁶ However, in humid atmospheres, the dangling bonds at the edges of TMD flakes rapidly react with oxygen and water vapor, resulting in the formation of MoO_3 and WO_3 .⁵⁷ These tribo-oxidation processes accelerate with increasing temperature, leading to higher friction coefficients and significantly shorter wear life for MoS_2 above 300 °C and for WS_2 above 400 °C.^{58–60} Recent advances in coating technology, however, have produced lubricating coatings with notable improvements in mechanical properties and resistance to humidity, allowing TMD coatings to be used in terrestrial applications as well.⁵⁴ Additionally, TMDs have been tested in composite coatings with other phases, unlocking synergistic effects that provide very low friction and wear rates, or enhance resistance to higher temperatures and harsh environments.^{61–63} In Chapter 3 of this manuscript, I will present recently-published experimental and computational results on the synergistic effects of MoS_2 /MXene hybrid composite coatings.⁶⁴

In most practical applications, TMDs are either burnished onto the surface or applied as thin solid films using techniques like sputtering.⁵⁴ However, in Chapter 4, I will describe an innovative in-operando conversion of Se nano-powders into lubricious 2D selenides by sprinkling them onto sliding metallic surfaces coated with Mo and W.⁶⁵ This novel approach offers several advantages. First, using chalcogen powder instead of sputtered coatings prevents the degradation of lubricant properties caused by interaction with air humidity. Second, the tribological contact can be easily replenished by feeding nano-powders into the contact. Third, this approach is applicable in high-temperature conditions or at the nanoscale, where liquid media or sputtered coatings are not suitable.

1.2.2.4 MXenes

MXenes represent an almost infinitely large family of two-dimensional layered materials, with the first member, $\text{Ti}_3\text{C}_2\text{T}_x$, synthesized in 2011.³⁵ Despite having a small but finite thickness, MXenes are defined as 2D layered carbides, nitrides, or carbonitrides of transition metals. They are typically represented by the general formula $\text{M}_{n+1}\text{X}_n\text{T}_x$, where $n+1$ layers ($n = 1, 2, 3, \text{ or } 4$) of early transition metals (“M” = Ti, Nb, Mo, V, etc.) are interleaved with n layers of carbon or nitrogen (“X” = C and/or N) and are passivated by a variety of surface terminations ($\text{T} = \text{F}, \text{O}, \text{OH}, \text{Cl}, \text{ etc.}$, with x usually equal to 2).^{36,39} Since the value of n determines the number of M and X layers within a 2D flake, both the composition and the thickness of MXenes can be widely tuned, leading to a vast array of possible 2D structures.⁶⁶ MXenes are derived from 3D crystalline precursors, usually MAX phases, with the chemical formula $\text{M}_{n+1}\text{AX}_n$ ($n = 1$ to 4), where the M-X layers found in MXenes are sandwiched between layers of A elements (e.g., Al, Ga).⁶⁷ In MAX phases, the M-A bonds are purely metallic, while the M-X bonds are much stronger, exhibiting ionic/covalent character. Consequently, it is possible to selectively remove the A layers through chemical etching (e.g., using aqueous HF solutions) to break the M-A bonds. The bonding sites on the M layers left vacant after A-layer removal are passivated by surface terminations (T_x),⁶⁸ whose composition and distribution depend on synthesis conditions, such as the type and concentration of the etchant, as well as etching temperature and duration.⁶⁹ **Figure 1.5** illustrates the wide compositional space of MXenes. It should be noted that this overview only covers one branch of the vast MXene family (referred to as “ordered mono-M MXenes”). Other combinations have also been explored, such as in-plane and out-of-plane ordered double-M MXenes, solid solutions of M and/or X sites, and high-entropy MXenes.⁷⁰ However, for the purposes of this thesis, the discussion will be limited to mono-M MXenes, focusing specifically on $\text{Ti}_3\text{C}_2\text{T}_x$, the most widely studied MXene for tribological applications.

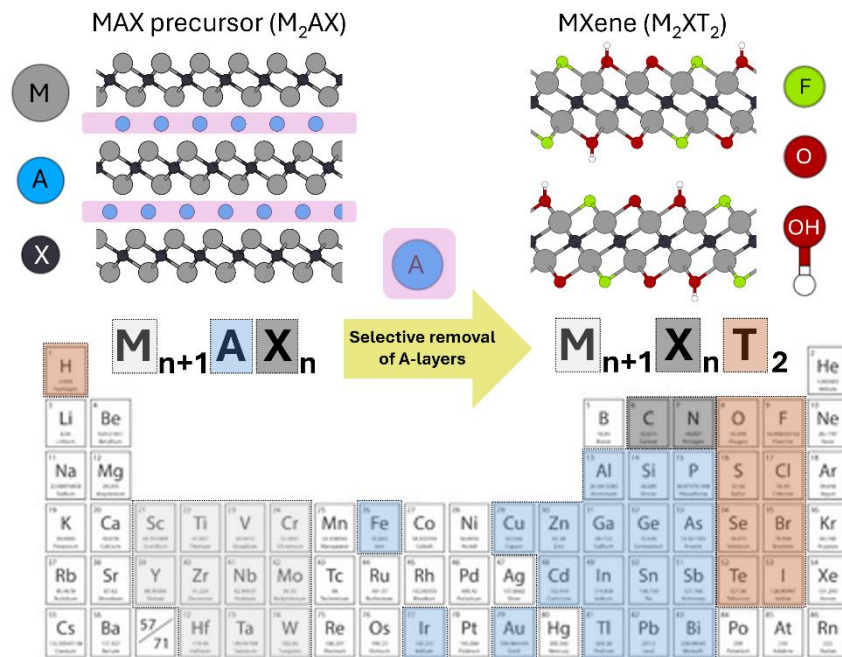


Figure 1.5: Schematic of selective etching of A-group elements in a MAX crystalline precursor, leading to MXene, with the elements that can form M, A, X, and T highlighted in the periodic table, and n being an integer number ranging between 1 and 4.

Thanks to their unique combination of 2D structure, electrical conductivity, tunable surface chemistry, and mechanical properties, MXenes have found applications in a wide range of fields, including energy storage devices (batteries and supercapacitors),^{71,72} electromagnetic interference (EMI) shielding,⁷³ water purification,⁷⁴ catalysis,^{75,76} biomaterials,⁷⁷ and, of course, tribology.^{78,79} The remarkable tunability of MXenes is a unique trait within the realm of 2D nanomaterials, especially given the simplicity and scalability of their fabrication process, which enables further scale-up and commercialization.⁸⁰ Furthermore, novel, milder, and more environmentally friendly synthesis routes beyond traditional carbide and nitride exfoliation processes have allowed for new compositions, chemistries, and property tuning.⁷⁰ Although an infinite number of MXenes may exist in principle, approximately 50 have been reported so far, with $\text{Ti}_3\text{C}_2\text{T}_x$ being the most prominent.⁸¹

In this context, while material scientists continue to explore new MXene compositions, tribologists have been investigating MXenes' tribological properties for the past decade, focusing on their use as lubricant additives, reinforcement phases in composites, and solid lubricants.⁸² To date, MXenes have demonstrated low shear strength, self-lubricating ability, rapid tribofilm formation during sliding, good mechanical strength, and higher Young's modulus and stiffness compared to other 2D materials, confirming their potential for tribological applications, particularly in solid lubrication.^{78,79} Numerous studies have confirmed the lubricating performance of MXenes, conducted both in laboratory test rigs^{83–88} and on real machine components.^{89,90} However, the mechanisms behind friction reduction and how these materials can be optimized in terms of frictional and wear behavior are still not fully understood. Moreover, material-related challenges such as adhesion to substrates, degradation due to tribo-oxidation, hydrophilicity, and performance under high loads, humidity, and temperature are still being investigated.^{78,79}

In Chapter 2 of this thesis, I will present numerical simulations of titanium-based MXenes,^{91,92} highlighting the role of layer thickness, carbon/nitrogen substitution, and surface terminations in influencing interlayer adhesion, shear ability, substrate adhesion, and hydrophilicity from a nanoscale perspective.

1.2.2.5 Transition Metal Carbo-Chalcogenides (TMCCs)

Transition Metal Carbo-Chalcogenides (TMCCs) can be regarded as a branch of MXenes that exhibit homogeneous sulfur termination.⁴¹ The family name was proposed by Majed et al. in 2022,⁴⁰ to highlight their similarity to Transition Metal Dichalcogenides (TMDs), as TMCCs represent an inherent and intriguing combination of a MXene core and a TMD surface. Their structural characteristics are illustrated in **Figure 1.6**, which also outlines their synthesis process. Multilayer niobium carbo-sulfide ($\text{Nb}_2\text{S}_2\text{C}$) and tantalum carbo-sulfide ($\text{Ta}_2\text{S}_2\text{C}$) can

be obtained from 3D bulk precursors ($\text{TM}_x\text{Nb}_2\text{S}_2\text{C}$ and $\text{TM}_x\text{Ta}_2\text{S}_2\text{C}$, respectively) through selective etching of the intercalated metals (TM = Fe, Cu, Ti, Co, etc.) using highly concentrated acid, such as HCl.⁴⁰

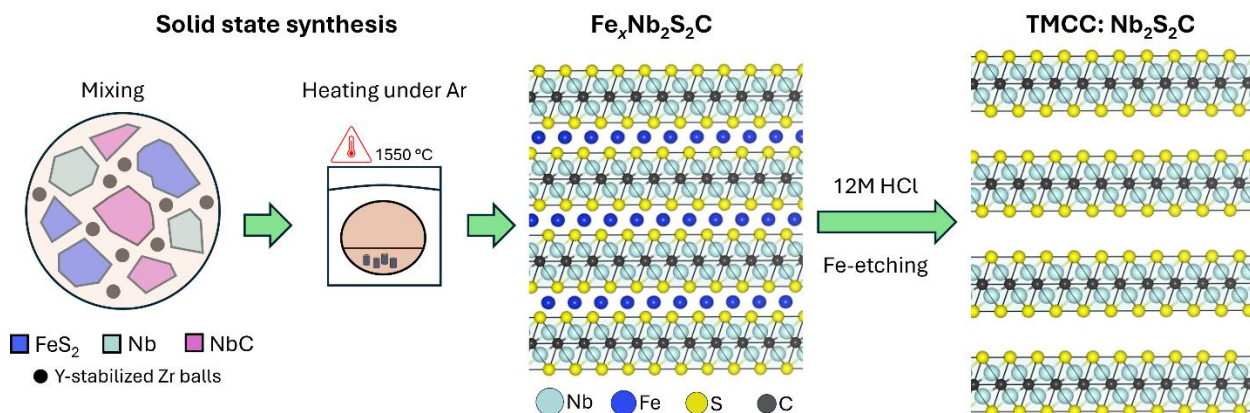


Figure 1.6: Schematic of the synthesis of multilayer $\text{Nb}_2\text{S}_2\text{C}$ by selective etching of Fe in $\text{Fe}_x\text{Nb}_2\text{S}_2\text{C}$ crystalline precursor, originally obtained from solid-state reaction of commercially available precursors in the ratio Nb:NbC:FeS = 1.0:1.0:1.5.

This family of 2D materials has been completely overlooked by the tribological community. Although the synthesis of several TMCCs in bulk 3D form, such as $\text{Ta}_2\text{S}_2\text{C}$ and $\text{Nb}_2\text{S}_2\text{C}$, was achieved in the last century,^{93,94} it wasn't until the successful exfoliation of TMCCs into single layers in 2022 that this family of materials began to attract attention, particularly in fields such as electrochemical energy conversion and storage.⁴¹ However, no comprehensive study on their application as solid lubricants has yet been reported in the literature. To date, only one study has investigated the tribological properties of $\text{Ta}_2\text{S}_2\text{C}$ and $(\text{Ta}, \text{Nb})_2\text{S}_2\text{C}$ transition metal carbo-chalcogenides.⁹⁵ In their 1998 work,⁹⁵ Wally and Ueki documented promising tribological properties for bulk carbo-sulfides, but further research was not pursued, leaving this class of 2D materials largely unexplored. An impactful experimental-computational study on the solid lubricant performance of multilayer $\text{Ta}_2\text{S}_2\text{C}$ and $\text{Nb}_2\text{S}_2\text{C}$ TMCCs will be presented in detail in Chapter 5 of this manuscript.⁹⁶

1.3 Density Functional Theory (DFT) applied to Tribology

Tribological events involve mechanical, physical, and chemical processes across different scales. While mechanical deformations, fractures, and wear are best described at the macro- and micro-scales, chemical bond transformations require a detailed analysis at the nanoscale. To fully understand how tribological surfaces interact with each other, as well as with lubricants, the environment, and substrates, a deep dive into the atomistic scale is necessary. Computational simulations provide the opportunity to study these phenomena in controlled conditions, free from the technical limitations often encountered in experimental setups. Moreover, *in silico* techniques allow us to monitor the evolution of tribochemical reactions occurring at buried interfaces, which are challenging to observe experimentally. First-principles or *ab initio* simulations are powerful tools for studying the quantum

mechanical behavior of tribological interfaces without relying on empirical parameters. In particular, Density Functional Theory (DFT) offers an efficient compromise between accuracy and computational cost, especially given the vast computational resources available today.⁹⁷ A detailed explanation of DFT's complex theoretical framework is beyond the scope of this introduction, as these theoretical foundations are well-documented in academic textbooks⁹⁸ and reviews.⁹⁹ However, I will provide a brief overview for non-experts, followed by an overview on key material properties related to friction that are reliably calculated using DFT methods.

In quantum mechanics, any three-dimensional system containing N electrons is described by a wave function depending on $3N$ variables. Simulating extended systems is, therefore, an extremely demanding task. The key quantity in DFT is the electronic density, which depends only on three spatial variables (x, y, z), independent of the number of electrons, providing a significant simplification to the many-body problem. DFT was formulated as an exact theory in 1964,¹⁰⁰ when Pierre Hohenberg and Walter Kohn proposed two fundamental theorems:

1. The total energy of a system is a unique functional of the electronic density of its ground state.
2. This functional reaches its minimum if and only if the input density is the true ground-state density (variational principle).

A year later,¹⁰¹ Walter Kohn and Lu Jeu Sham proposed that any interacting system could be described by a single-particle effective potential of a non-interacting system with the same ground-state density. Thus, the exact ground-state density is constructed from a set of orbitals, which are the eigenfunctions of a one-particle operator, known as the Kohn–Sham Hamiltonian. In this formalism, the challenge of finding an analytical expression for the energy functional is reduced to one specific contribution: the "exchange-correlation functional." While the theory remains exact at this stage, the analytic form of the exchange-correlation potential (V_{xc}) is unknown. Over the years, numerous approximations for V_{xc} have been developed, leading to a proliferation of functionals.¹⁰² Among these, the PBE functional (named after its authors, Perdew, Burke, and Ernzerhof)¹⁰³ is the most widely used in materials science.⁹⁹

DFT can be applied to both static and dynamic calculations, with the latter referred to as *ab initio* molecular dynamics (AIMD) simulations. In both approaches, external mechanical stresses are simulated by applying forces and velocities to specific atoms within the simulation cell. Static simulations are typically used to investigate electronic,^{104–106} vibrational,^{107–109} and mechanical properties,^{110–112} as well as to provide insights into reaction pathways and energy barriers.^{113–115} In tribology, static calculations are commonly employed to examine: i) interactions between surfaces, such as adhesion energy, Potential Energy Surface (PES), PES corrugation, minimum-energy paths (MEP) along the PES, shear strength, and charge transfer; or ii) interactions between molecules and substrates, such as physisorption or chemisorption energies, vibrational spectra, kinetic barriers, and charge

transfer.⁹⁹ In my PhD research, static DFT simulations have been used to explore the aforementioned tribological properties of MXenes, TMDs, and TMCCs, as detailed in Chapters 2, 3, and 4.

On the other hand, dynamic simulations allow for the observation of the time evolution of tribological systems, tracking atomic trajectories and temperature effects.^{116–121} While static DFT is effective in elucidating the adsorption and structural properties of individual molecules at zero temperature, AIMD provides insights into the structural properties of the full lubricating film, revealing mechanistic details of tribofilm formation under the influence of both temperature and external stresses. Chapter 4 of this dissertation presents AIMD simulations of selenium nanoparticles confined between molybdenum surfaces, investigating the *in operando* formation of MoSe₂, as observed in real experiments.⁶⁵ AIMD is also valuable for evaluating resistive forces to sliding, offering predictions of realistic coefficients of friction in agreement with experimental results,¹¹⁷ particularly at the nanoscale.¹²²

However, AIMD is often limited to short timescales (hundreds of picoseconds), whereas some tribological events require simulations over longer timescales (several nanoseconds). An example is the polymerization of lubricant additive molecules confined at a metallic interface.^{123,124} A recent approach adopted by the tribological community to overcome this limitation is the development of machine learning interatomic potentials (MLIP) for atomistic simulations, constructed from accurate DFT-based datasets.^{122,125} MLIP models offer remarkable performance, enabling simulations to scale up in both time and length, although their physical interpretation is often obscured by their "black-box" nature. With the Nobel Prize awarded to John J. Hopfield and Geoffrey E. Hinton in October 2024 for their foundational discoveries and inventions that enable machine learning with artificial neural networks, we can expect these methods to become a standard tool in computational science.

Chapter 2

2. Tribological properties of Ti-based MXenes by DFT simulations

The tribological performances of MXenes, have been increasingly investigated in last 10 years.⁷⁸ From the discovery of the progenitor in 2011 ($\text{Ti}_3\text{C}_2\text{T}_x$),³⁵ the first publication related to tribology only appeared in 2014, with $\text{Ti}_3\text{C}_2\text{T}_x$ used as lubricant additive in base oil.¹²⁶ The first application for solid lubrication is dated back to 2016,¹²⁷ with $\text{Ti}_3\text{C}_2\text{T}_x$ used as a reinforcement phase in MXene/polymer composites. However, the first pure MXene coating was reported in literature only in 2018,⁸³ when Lian et al. deposited $\text{Ti}_3\text{C}_2\text{T}_x$ onto a copper disk and observed the formation of a carbon-rich tribofilm able to prevent direct contact between sliding surfaces. Later on, the research on MXenes for tribology has rapidly developed, giving rise to a huge number of potential lubricating applications, especially for solid lubrication purposes.^{83–87} Despite the inherent tunability of MXenes in terms of chemical composition and structure, Ti-based ones remained the most studied, both experimentally and theoretically. While a general overview about MXenes has already been presented in Chapter 1.2.2.4, this chapter provides a wide exploration of the nano-tribological properties of Ti-based MXenes, carried out through numerical DFT simulations. All the results presented in this chapter are also part of two recently published articles.^{91,92}

2.1 Introduction

MXenes can be described by the general formula $\text{M}_{n+1}\text{X}_n\text{T}_x$, where M is an early transition metal (Ti, V, Mo, Nb, etc.), X represents carbon and/or nitrogen, n can generally vary from 1 to 3, while T_x identifies the terminating groups covering the surface (mainly $-\text{F}$, $-\text{O}$, $-\text{OH}$).^{36,39} MXenes are synthesized via a top-down synthesis approach from 3D crystalline MAX precursors with chemical formula $\text{M}_{n+1}\text{AX}_n$, by selectively removing the layers of the A-group elements (mainly group IIIA and IVA of the periodic table) using acidic aqueous solutions.^{37,66,67} The composition of the surface terminations depends on the etching conditions, in particular, the etchant type and concentration, as well as etching temperature and duration.⁶⁹ Experimental studies using nuclear magnetic resonance (NMR),^{128,129} X-ray photoelectron spectroscopy (XPS)¹³⁰ and thermal gravimetric analysis coupled with mass spectrometry (TGA-MS)¹³¹ have shown that the MXene surfaces are commonly terminated with a random distribution of $-\text{F}$, $-\text{O}$ and $-\text{OH}$ groups, at least when using aqueous HF as etchant.

Although experimental characterization verified a mixture of different surface terminations on MXenes, most of the computational studies related to tribology have considered only homogeneous terminations.^{132–136} Hu et al. investigated the interlayer coupling of $\text{Ti}_{n+1}\text{C}_n\text{T}_2$ (T: OH, O and F),¹³² by calculating the binding energies (B_e) of stacked $\text{Ti}_3\text{C}_2\text{T}_2$ considering both homogeneous and heterogeneous interfaces (e.g., $\text{Ti}_3\text{C}_2\text{T}_2@ \text{Ti}_3\text{C}_2\text{T}'_2$ with $\text{T} \neq \text{T}'$). They found

that the B_e of different terminations followed the order: $Ti_{n+1}C_n(OH)_2 > Ti_{n+1}C_nO_2 > Ti_{n+1}C_nF_2$. In subsequent works,^{133,134} the static friction coefficients for the interlayer sliding of $Ti_{n+1}C_nO_2$ bilayers (n : 1, 2 and 3) have been evaluated by deriving minimum energy pathways on the potential energy surface (PES). Serles et al. exploited friction force microscopy (FFM) combined with DFT studies to evaluate the lubricating properties of $Ti_3C_2T_x$ flakes against a diamond-tipped cantilever.¹³⁵ They demonstrated that a reduction of $-OH$ surface terminations in favor of $-F$ and $-O$ can be achieved by annealing $Ti_3C_2T_x$ flakes, leading to reduced frictional forces. However, a systematic study on nano-tribological properties of $Ti_{n+1}C_nT_x$ MXenes that considers the presence of mixed terminations has never been published.

In this context, in Chapter 2.3.1 we present DFT calculations to investigate the behavior of Ti-based MXenes with different types of surface terminations (combining $-F$, $-O$ and $-OH$). The influence of the carbon/nitrogen content and the layer thickness is also considered. We present several nano-tribological properties including interlayer adhesion for homo-, hetero-, and mixed-interfaces, its variation as a function of the relative lateral position of the layers (PES), as well as the PES corrugation in the presence of an external normal load applied.

Since the efficiency of a solid lubricant depends not only on the interlayer interactions, but also on the layer-substrate interaction, in Chapter 2.3.2 we describe the role of the MXene terminations (T) in affecting the adhesion on ferrous substrates, i.e., pristine iron (Fe) and hematite (Fe_2O_3), to get insights into their ability to lubricate steel.

The functionality of MXenes in technological applications hugely depends on their wettability. Indeed, their stability against degradative oxidation is notably reduced when stored in aqueous solutions, leading to the transformation into oxides.^{137,138} Therefore, within the last section (Chapter 2.3.3) we discuss the fundamental aspects concerning the interaction of MXenes with water. We unravel the hydrophilicity of MXenes as a function of the termination type (T), the carbon/nitrogen ratio (X) and the layer thickness (n), considering both defect-free and defective surfaces/edges.

2.2 Methods

General. We performed spin-polarized DFT calculations employing version 6.7 of the Quantum ESPRESSO package.^{139–141} The generalized gradient approximation (GGA) within the Perdew-Burke-Ernzerhof (PBE) parametrization under the consideration of dispersion interactions was adopted to describe the electronic exchange and correlation.¹⁰³ To properly consider the van der Waals (vdW) interactions, we used an *ad hoc* modification of the Grimme D2 dispersion correction scheme,¹⁴² which differs from the standard D2 only for the C_6 coefficient and the van der Waals radius R_0 of the metal atoms (Ti, Mo and Fe), which are replaced with those of the preceding noble gas in the periodic table (Ar). Hence, we named this variation D2_{NG}, which has been validated against other vdW corrections through deep benchmarking, as presented in chapter 2.2.1. The electronic wave-functions were expanded

on a plane-waves basis that was truncated with a cutoff of 50 Ry. A cutoff of 400 Ry was employed for the charge density. The ionic species were described by ultrasoft pseudopotentials, those of d-metal ions, i.e., Ti, Mo, and Fe, have 12, 14, and 16 explicit electrons for an accurate description of interfacial interactions. For the structural optimization, we adopted default criteria for energy and forces convergence, i.e., 10^{-4} Ry and 10^{-3} Ry/Bohr for the total energy and the atomic force components, respectively. We used a Gaussian smearing of 0.02 Ry to better describe the electronic states occupation around the Fermi level.

Models. MXene' hexagonal single cells have been sampled with a $12 \times 12 \times 1$ Monkhorst-Pack grid,¹⁴³ ensuring at least 15 Å of vacuum between periodic replicas along the z direction, so to avoid spurious interactions. However, single cells could only be employed for homogeneously terminated MXenes (e.g. Ti_2CO_2 , $\text{Ti}_2\text{C}(\text{OH})_2$, Ti_2CF_2 , $\text{Ti}_4\text{C}_3\text{F}_2$), while larger cells were needed when considering mixed terminations ($\text{Ti}_2\text{C}(\text{F}_{1/3}, \text{O}_{1/3}, \text{OH}_{1/3})_2$, $\text{Ti}_2\text{C}(\text{F}_{1/4}, \text{OH}_{3/4})_2$, $\text{Ti}_2\text{C}(\text{F}_{1/2}, \text{OH}_{1/2})_2$, $\text{Ti}_2\text{C}(\text{F}_{3/4}, \text{OH}_{1/4})_2$, etc.) or when studying low-coverage water physisorption over defected and not MXene surfaces. For the latter case, we employed $4 \times 4 \times 1$ orthorhombic supercells, adapting the Monkhorst-Pack grid density used for sampling the Brillouin zone. Indeed, single-atom defects have been introduced by removing a termination (V_T), a titanium atom (V_Ti), or a carbon/nitrogen atom (V_X). The resulting vacancies concentration corresponds to 6.25%, obtained by the removal of one atom from the employed 4×4 supercell, as modeled by other authors.¹⁴⁴ This value is compatible with data on $\text{Ti}_3\text{C}_2\text{T}_\text{x}$ monolayers obtained by scanning transmission electron microscopy (STEM) measurements that suggest a large range of defect densities depending on the synthesis conditions as well as the quality of the initial bulk precursor.^{145,146} MXene flakes with clusters of vacancies were modelled by removing at least two adjacent atoms from the surface. For instance, a " $p\text{V}_\text{Ti} + q\text{V}_\text{T}$ " cluster is obtained by removing p atoms of Ti and q termination groups ($p= 1,2$ and $q= 1,2,3$). MXene nanoribbons were built according to the work of Zhao et al.¹⁴⁷, focusing on zigzag nanoribbons having the empirical formula $\text{Ti}_8\text{C}_3\text{T}_8$ that showed the lowest edge energy. To model the analogous nitrogen-based ribbons, i.e., $\text{Ti}_8\text{N}_3\text{T}_8$, we kept the same geometrical structure, allowing the relaxation of the atomic positions. A summary of the models employed in this work is presented in **Figure 2.1**.

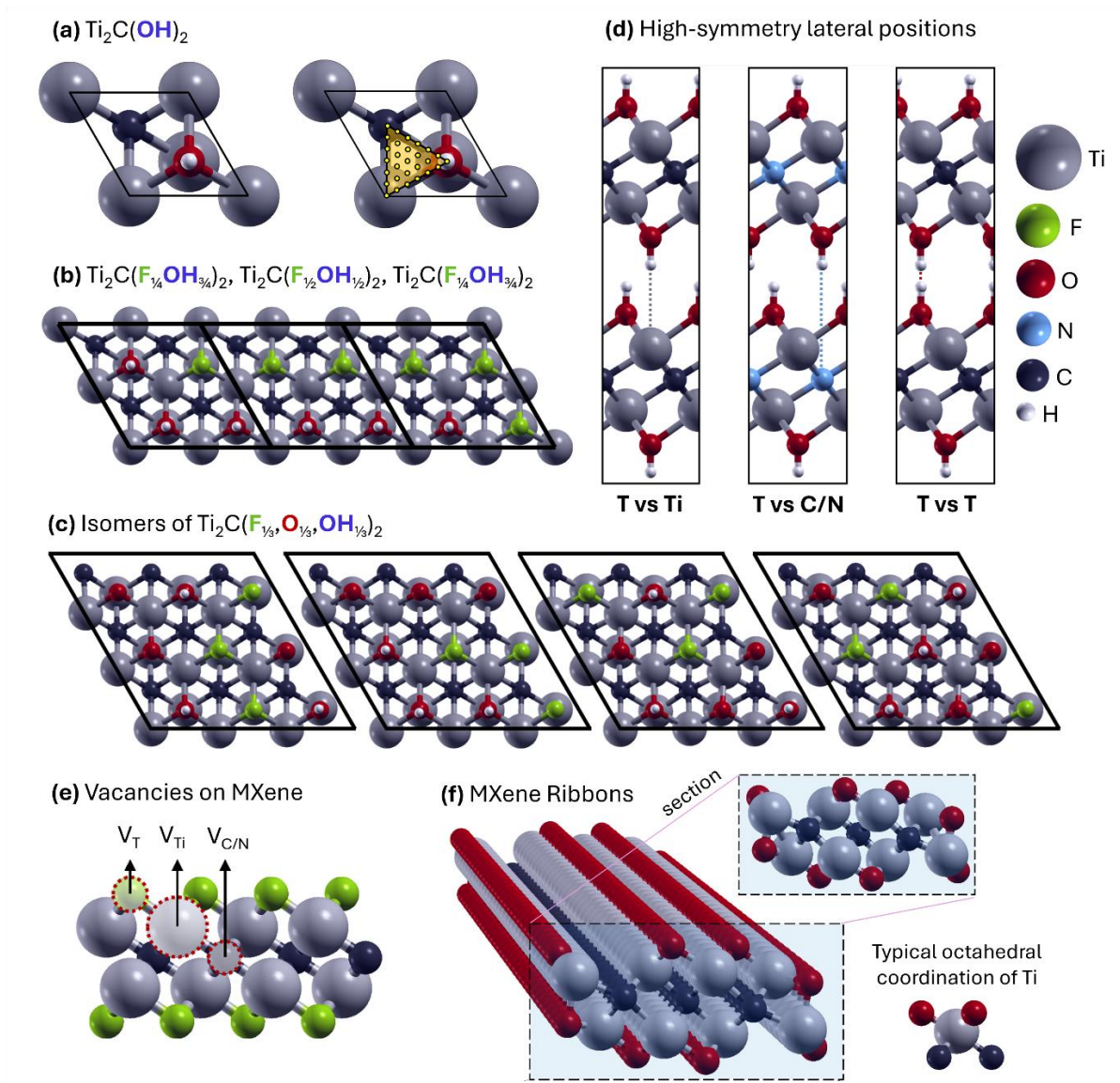


Figure 2.1: (a) Top-view of the hexagonal cell employed for MXenes with single-type terminations. The lateral displacements considered for the construction of the potential energy surfaces are also reported. The grid of points is then replicated using symmetry operators to fill the cell homogeneously. (b) Top-view of the unit cells employed for MXenes with two different types of termination on the surface. $\text{Ti}_2\text{C}(\text{F}_{1/4}\text{OH}_{3/4})_2$, $\text{Ti}_2\text{C}(\text{F}_{1/2}\text{OH}_{1/2})_2$ and $\text{Ti}_2\text{C}(\text{F}_{3/4}\text{OH}_{1/4})_2$ are exemplarily shown with a compact representation, but they have been considered individually for the calculations. (c) Top-views of the unit cells employed to model MXene surfaces simultaneously covered by $-\text{F}$, $-\text{O}$ and $-\text{OH}$, i.e., $\text{Ti}_2\text{C}(\text{F}_{1/3}\text{O}_{1/3}\text{OH}_{1/3})_2$. The models differ in the relative atomic position of the terminations with respect to M and C atomic sites. (d) Lateral view of the relative lateral positions with high symmetry, where the terminations (T) point towards Ti (left), C/N (middle), or towards each other (right). (e) Schematic of the single atomic defects considered: termination (V_{T}), titanium (V_{Ti}) and carbon/nitrogen ($V_{\text{C/N}}$) vacancies. (f) Perspective view and cross-section of the $\text{Ti}_8\text{C}_3\text{O}_8$ nanoribbon. In the lower right corner, the octahedral coordination usually found for Ti atoms in MXenes is shown, which instead is distorted in nanoribbons.

Interlayer adhesion. To evaluate interlayer adhesion, interfaces were obtained by stacking two MXenes layers. Each interface will be referred according to the mating surfaces: a “homo-interface” (“hetero-interface”) is formed by two identical (different) MXenes with single-specie terminations, e.g., $\text{Ti}_2\text{CF}_2@\text{Ti}_2\text{CF}_2$ ($\text{Ti}_2\text{CF}_2@\text{Ti}_2\text{CO}_2$). In contrast, a “mixed-interface” is built by mating two MXene layers that are covered by two or three different types of terminations (e.g., $\text{Ti}_2\text{C}(\text{O}_{1/4}\text{OH}_{3/4})_2@\text{Ti}_2\text{C}(\text{O}_{1/4}\text{OH}_{3/4})_2$ or $\text{Ti}_2\text{C}(\text{F}_{1/3}, \text{O}_{1/3}, \text{OH}_{1/3})_2@\text{Ti}_2\text{C}(\text{F}_{1/3}, \text{O}_{1/3}, \text{OH}_{1/3})_2$). To identify the most favorable stacking of parallel layers, we considered the high-symmetry lateral positions represented in **Figure 2.1d**. In these three configurations, the atom or group, belonging to the termination (T) of the upper layer is placed on-top the metal atom (T versus Ti), the carbon/nitrogen (T versus C/N) or another surface termination (T versus T) of the bottom layer. In the case of mixed-interfaces, the number of high-symmetry lateral positions considered for identifying the most stable stacking was increased, since several combinations were possible. The interlayer adhesion has been calculated as “work of separation (W_{SEP})”, i.e. the energy required to separate bilayers. W_{SEP} , which is the opposite of the adhesion energy (E_{ADH}), is obtained as:

$$W_{\text{SEP}} = -E_{\text{ADH}} = -\frac{2E_{\text{monolayer}} - E_{\text{bilayer}}}{A} \quad (2.1)$$

where $E_{\text{monolayer}}$ (E_{bilayer}) is the total energy of a single layer (bilayer) and A is the contact area.

Potential Energy Surface. For both homogeneous and heterogeneous interfaces, we constructed the PES experienced by the upper monolayer upon translation above the lower one. Due to the presence of several species with different chemical natures, we increased the number of relative lateral positions (x , y) to capture all features of the PES. For each lateral displacement, the x and y atomic coordinates were kept fixed, while the z coordinate was relaxed so that the equilibrium interfacial distance was reached for every lateral position. **Figure 2.1a** reveals the grid of points used to calculate the PES, which belongs to the irreducible zone of the hexagonal cell. To investigate the effect of increasing normal loads, we repeated the calculation of adhesion in the presence of a force perpendicular to the basal plane and applied to the highest Ti atom of the top layer. In this case, the lower Ti atom of the bottom layer was fixed during relaxation. The potential corrugation (ΔW_{SEP}), which represents the maximum energy barrier that needs to be overcome during sliding of two adjacent MXene layers, is evaluated as the difference between the maximum and minimum W_{SEP} experienced during the relative lateral displacement:

$$\Delta W_{\text{SEP}} = W_{\text{SEP}}^{\text{max}} - W_{\text{SEP}}^{\text{min}} \quad (2.2)$$

Adhesion to substrate. To explore the adhesion of MXenes layers to a hematite substrate (Fe_2O_3), we employed the PBE functional with the Hubbard correction (PBE+U).¹⁴⁸ The U value was set to 4.2 eV as suggested by previous adsorption studies on hematite.^{149,150} The spin of d electrons localized on Fe atoms was assigned to have wave functions with anti-ferromagnetic character.¹⁵¹ We forced Fe d -orbital occupation to ensure that the wave function converges

on non-metallic electronic states. We considered the (001) surface, which is a stable low-index hematite crystal facet, exposing a single Fe atom as termination.¹⁵² We ensured full convergence of the Brillouin zone sampling by using a 6x6x1 grid of k points. For pure iron substrate (Fe), we considered the most stable low-index Fe surface, i.e. (110).¹⁵³ In matching the 2D materials with the substrate, we allowed for a maximum deformation of 5% of the unit cell of the 2D materials. The partial atomic charges were evaluated by means of the Bader Charge analysis.^{154–157}

Interaction with water. To model the isolated water, we employed a cubic cell with about 25 Å side length, which was large enough to consider the molecule as isolated. The adsorption energy (E_{ads}) for water was calculated as the difference between the total energy of the interacting system and the sum of the energies of the substrate and the isolated water molecule. To study the dependence of E_{ads} on the water coverage, we normalized the energy value by the number n of adsorbed water molecules:

$$E_{\text{ads}}(n) = \frac{E_{\text{total}} - (n \cdot E_{\text{H}_2\text{O}} + E_{\text{substrate}})}{n} \quad (2.3)$$

We will refer to the “energy gain” (E_{gain}) as the absolute value of the adsorption energy (i.e., $E_{\text{gain}} = |E_{\text{ads}}|$). To increase the probability of finding the lowest energy configuration for the adsorbed water, we explored different starting molecular configurations, differing regarding the H₂O orientation relative to the surface (in-plane water, oxygen-up and oxygen-down), the H₂O rotation angle with respect to the perpendicular axis and the lateral position. Despite a large number of initial configurations, the final geometries were often equivalent, coinciding with a local minimum or global minimum.

2.2.1 The zoo of dispersion correction methods

To order to account for dispersion interactions, which are known to rule the interlayer adhesion of many 2D materials, we initially considered several correction schemes, such as the Grimme’s D2,¹⁴² and D3-BJ parametrizations,¹⁵⁸ the Tkatchenko-Scheffler with iterative Hirshfeld partitioning (TS-H),¹⁵⁹ Many Body Dispersion (MBD),¹⁶⁰ dDsC,¹⁶¹ as well as vdW-DF2¹⁶² SCAN functionals,¹⁶³ in which dispersion forces are included directly into the density functional. We compared the results with high-level theory methods, such as the Random Phase Approximation (RPA),¹⁶⁴ and the second order Møller–Plesset perturbation theory (MP2)¹⁶⁵ from a previous work.¹⁶⁶ The scheme adopted in this work consisted of an *ad hoc* version of the D2 parametrization, referred to as D2_{NG}, in which the C_6 coefficient and the van der Waals radius R_0 of the metal atoms (Ti, Mo and Fe) are replaced with those of the preceding noble gas, i.e. argon. This approach demonstrated to give good results for similar 2D materials.¹⁶⁶ In particular, for the C_6 coefficient (in units of J nm⁶ mol^{−1}), we used a value of 4.61 instead of 10.80, while for the vdW radius R_0 we used 1.595 Å instead of 1.562 Å. All simulations related to the influence of the dispersion forces were carried out using the Vienna Ab initio Simulation Package (VASP) code.¹⁶⁷

In 2D inorganic materials like MXenes, the interlayer interactions comprise H-bonding, dipole-dipole, and dispersion London interactions (i.e. vdW interactions).¹⁶⁶ Dispersion forces are neglected by most of plain DFT functionals, although in the last two decades, several approaches have emerged to overcome this limitation.¹⁶⁸ However, most of the available dispersion correction methods for DFT have been developed for organic molecules, so they should be carefully applied to inorganic solid-state materials.¹⁶⁶ More advanced, parameter-free methodologies such as the Møller–Plesset perturbation theory (MP2) and the Random Phase Approximation (RPA) can capture the elusive dispersion forces in an accurate way in solid inorganic systems. These methods are computationally too demanding to be employed for systematic studies as presented in this chapter. However, they can be used as a benchmark for the proper choice of the parameters in DFT schemes, which include the dispersion interactions in a parametric way. Unfortunately, the direct application of the above-mentioned fully *ab initio* methods to conductive materials with a complex electronic structure as MXenes is not straightforward. In this regard, insulating materials, which have similar structures as MXenes, can be employed as more feasible test cases. Materials with these features are natural clays, such as Mg and Ca hydroxides. They have the same octahedral metal coordination as MXenes but an insulating electronic structure (**Figure 2.2a**).

For these materials (Figure 2.3a), we have computed accurate MP2 and RPA work of separation thus comparing the results with the most common dispersion-corrected DFT functionals available for solid state materials. The results clearly indicate that the choice of the dispersion scheme is crucial to obtain accurate adhesion energies. Grimme's D2, D3, Tkatchenko-Scheffler (TS-H) and Many Body Dispersion (MBD) *a posteriori* corrections overbind Mg and Ca hydroxides layers, almost doubling the interaction energy. Similar results are obtained with the vdW-DF2 functional, which has been employed to study the tribological properties of MXenes in Refs.^{133,134} Interestingly, SCAN functional gives remarkably accurate results. The drawback of the SCAN functional, belonging to the meta-GGA family, relates to its computational cost, which is roughly 8 times higher than the GGA PBE functional.

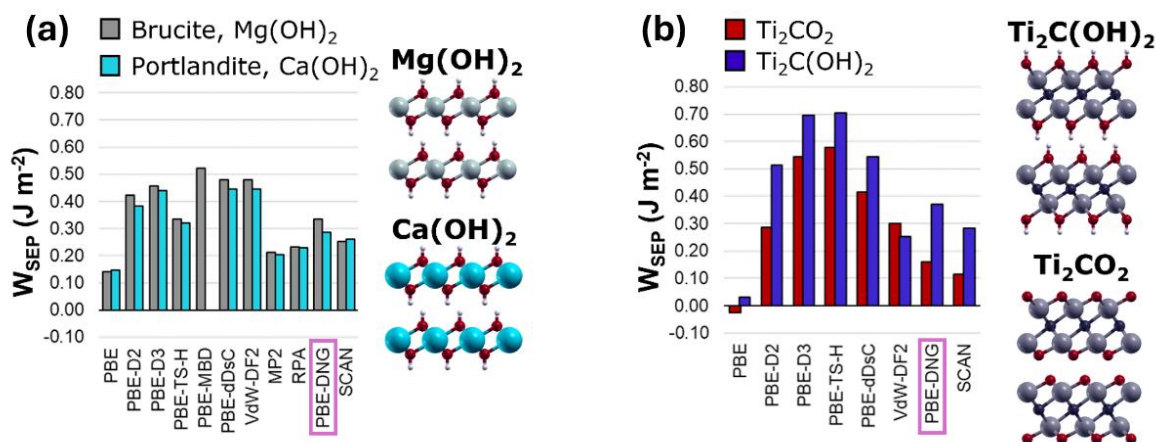


Figure 2.2: Work of separation for (a) brucite (grey), portlandite (light blue), (b) $\text{Ti}_2\text{C}(\text{OH})_2$ (blue) and Ti_2CO_2 (red) calculated with different dispersion correction methods. PBE- D_{NG} refers to the D2 scheme with the Ti parameters replaced by those belonging to Ar.

Aiming at finding a fast and accurate approach to investigate MXenes systematically, we have also tested the D_{NG} a posteriori correction. This approach employs the pairwise Grimme's -D2 scheme with the difference that the atomic parameters employed to describe the metal atoms are replaced with those of the proceeding noble gas. This is done to reduce the dispersion energy coming from metals atoms, whose standard parameters better describe a neutral isolated atom than a metal atom within a network of covalent-ionic bonds. Indeed, in this framework, the metal atom has lowered atomic polarizability due to the positive charge localized on the atom. A similar idea has been implemented in the very recent Grimme's D4 scheme,¹⁶⁹ which is nowadays unavailable in the Quantum Espresso suite. The computed adhesion energy for Mg and Ca hydroxides indicates that PBE- D_{NG} is a fast and accurate methodology for computing interlayer energy for MXene-type model materials.

After tuning the parameters of the PBE- D_{NG} scheme considering Mg and Ca hydroxides as a benchmark, we extended the method towards $\text{Ti}_2\text{C}(\text{OH})_2$ and Ti_2CO_2 MXenes (**Figure 2.2b**). In this case, MP2 and RPA methods cannot be applied straightforwardly. Consequently, we have considered the SCAN functional results as the reference method due to the good results obtained for Mg and Ca hydroxides. The results for MXenes agree well with the previous analysis: the PBE- D_{NG} approach is the only method capable of reproducing, with fair accuracy, both the overall absolute adhesion values and the order of stability of the SCAN reference method. These results indicate that the PBE- D_{NG} method provides a suitable approach for studying MXenes' interlayer interaction. Interestingly, the vdW-DF2 functional indicates that the O-termination induces higher W_{SEP} than the OH-termination in homogeneous interfaces, which disagrees with the reference method, i.e., SCAN, and all the other functionals employed in this work. Our result suggests that by employing the vdW-DF2 functional, spurious results can be obtained if the interfacial properties of MXenes are compared for different types of terminations.¹³³

2.3 Results and Discussion

2.3.1 Characterization of interlayer slipperiness

To evaluate the inherent interlayer slipperiness of Ti-based MXenes, we first evaluated the interlayer adhesion for homo-, hetero-, and mixed-interfaces. Then, we calculated its variation as a function of the relative lateral position of the layers, constructing the PES. The PES corrugation has been evaluated in the presence of an external normal load applied (from 1 to 10 GPa). Both interlayer adhesion and potential corrugation can be correlated to the shear strength of materials,^{105,112} thus providing a good estimation of the frictional properties. This nanoscale study is carried out in comparison with well-established solid lubricants such as MoS_2 and graphene.

2.3.1.1 Interlayer adhesion

In **Figure 2.3a**, we report the energies required to separate homogeneously terminated $Ti_{n+1}X_nT_x$ bilayers (with $n = 1$ and 3 ; $X = C$ and N ; $T_x = F, O$ and OH), sorted starting with the lowest energy configurations. The values of W_{SEP} obtained for Ti_2CF_2/Ti_2CO_2 and Ti_2NF_2/Ti_2NO_2 indicate that no differences occur between $-F$ and $-O$ terminated MXenes ($W_{SEP} \approx 0.16 \text{ J m}^{-2}$). Such behavior relates to the chemical similarities of the terminating atoms, which both possess a high electronegativity. When terminated with $-OH$, homo-interfaces of $Ti_2C(OH)_2$ ($W_{SEP} = 0.37 \text{ J m}^{-2}$) and $Ti_2N(OH)_2$ ($W_{SEP} = 0.26 \text{ J m}^{-2}$) show higher values. The increased values of W_{SEP} obtained when moving from $-F$ or $-O$ to $-OH$ terminated MXenes are consistent with the results of Hu et al.¹³²

In general, our calculations indicate that the substitution of carbon by nitrogen does not change the extent of the interaction when MXenes are F- or O-terminated, implying that the C/N ratio does not affect the interfacial properties for F/O-terminated MXenes. However, the changes become more noticeable for OH-terminated MXenes, for instance, $Ti_4C_3(OH)_2$ with $W_{SEP} = 0.39 \text{ J m}^{-2}$, which is higher than that of $Ti_4N_3(OH)_2$ with $W_{SEP} = 0.30 \text{ J m}^{-2}$. Our results demonstrate that, in the presence of hydroxyl groups, carbides tend to interact more than nitrides.

Finally, no remarkable differences stand out when comparing thin MXenes (Ti_2XT_x) with thicker ones ($Ti_4X_3T_x$). This suggests that the interaction between layers is mainly governed by the surface terminations of the outer layer, which are barely modified by increasing the thickness. However, thicker MXenes systematically show slightly higher W_{SEP} values (by $0.02/0.04 \text{ J m}^{-2}$), as the number of atoms interacting through long-range dispersion forces increases.

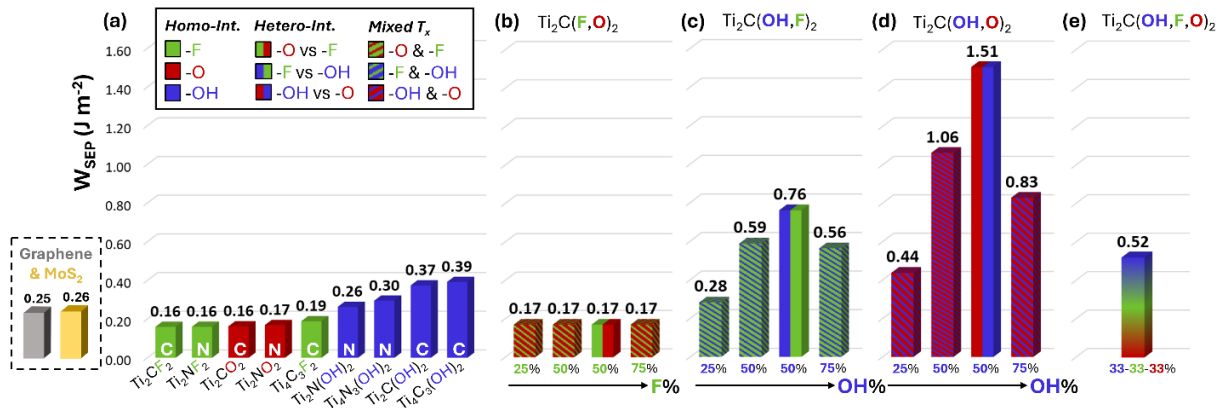


Figure 2.3: Work of separation W_{SEP} for (a) homo-interfaces with single-type terminations (in solid color bars), (b)-(d) mixed-interfaces combining different termination pairs (thin oblique lines motif) and hetero-interfaces (vertical line pattern). (e) Average value of W_{SEP} for $Ti_2C(F_{1/3}, O_{1/3}, OH_{1/3})_2@Ti_2C(F_{1/3}, O_{1/3}, OH_{1/3})_2$ interfaces considered. The W_{SEP} values for graphene and MoS_2 bilayers are included as references.

Figure 2.3b-d reports the cases in which two terminations are simultaneously present at the interface of thin MXene bilayers ($n = 1$, carbides i.e. $X = C$). The bars with the thin oblique lines pattern show the work of separation for mixed-interfaces composed by two identical MXenes each covered with two different terminations. The two colors of the thin lines follow the same color-code employed for the homo-interfaces: green, red, and blue highlight the presence of $-F$, $-O$ and $-OH$ terminations, respectively. We investigated all combinations between termination pairs: $-F$ and $-O$ (**Figure 2.3b**), $-OH$ and $-F$ (**Figure 2.3c**), $-OH$ and $-O$ (**Figure 2.3d**) with different coverages ranging between 25 and 75% for each termination group. The bars with the vertical line pattern refer to hetero-interfaces, which consist of two MXene layers, each terminated with a different type of termination. The values of W_{SEP} presented in **Figure 2.3b** are not influenced by the ratio between $-F$ and $-O$, as W_{SEP} is always equal to 0.17 J m^{-2} , which is almost the same value as previously presented for the $-F$ and $-O$ terminated homogeneous interfaces (**Figure 2.3a**). This result suggests that fluorine and oxygen confer almost the same properties to the bilayer. However, the presence of hydroxyl groups at the interface considerably increases W_{SEP} (**Figure 2.3c and d**). When a fully $-OH$ terminated MXene is coupled with a fully $-F$ or $-O$ terminated surfaces, the interaction is maximized ($W_{SEP} = 0.76 \text{ J m}^{-2}$ or $W_{SEP} = 1.51 \text{ J m}^{-2}$). Even for MXenes with mixed T_x ($-OH$ and $-F$, or $-OH$ and $-O$), the interaction is much stronger compared to the homogeneous interfaces. Interestingly, W_{SEP} does not increase linearly with the $-OH$ percentage but shows a maximum for a coverage of 50%. At 50% $-OH$ coverage, all hydroxyl groups can establish hydrogen bonds with the involved fluorine or oxygen atoms in an on-top configuration. However, when there is a lack of $-OH$ terminations ($-OH$ coverage lower than 50%), the number of hydrogen bonds formed at the interface is reduced. With an excess of $-OH$ terminations (above 50% $-OH$ coverage), the interaction is reduced due to the unavoidable steric hindrance of $OH-HO$ stacking.

The bar with fuzzy colors in **Figure 2.3e** refers to fully mixed interfaces, where the mated MXene layers are both passivated with a mixture of $-F$, $-O$ and $-OH$. Notice that $W_{SEP} = 0.52 \text{ J m}^{-2}$ represents the average value obtained by stacking the four isomers considered (see **Figure 2.1c**). Interestingly, the W_{SEP} values are very similar, ranging between 0.51 and 0.54 J m^{-2} (with a standard deviation of 0.01 J m^{-2}). This implies that the interaction between two “realistic” MXene layers does not depend on the relative position of the surface terminations, but only on their chemical composition. Even for MXenes with mixed terminations, we confirm that the interaction between layers is mainly driven by the concentration of hydroxyl groups on the surface.

In **Figure 2.4**, the optimized configurations of MXenes bilayers are reported, along with the equilibrium distances and partial atomic charges on the terminations (red and blue numbers). We also provide the perpendicular potential energy surfaces (pPES), which are obtained by calculating the adhesion energy between the paired surfaces at different fixed distances. Ti_2CF_2 (**Figure 2.4a**) and Ti_2CO_2 (**Figure 2.4b**) bilayers are characterized by

terminations with high electronegativity, thus presenting negative charges. The equilibrium interlayer distance reflects the magnitude of the partial negative charge of the termination. This implies that electrostatic repulsion governs the properties of the interface for F- and O-terminated MXenes. Indeed, for these systems, dispersion forces are essential to bind two MXene layers.

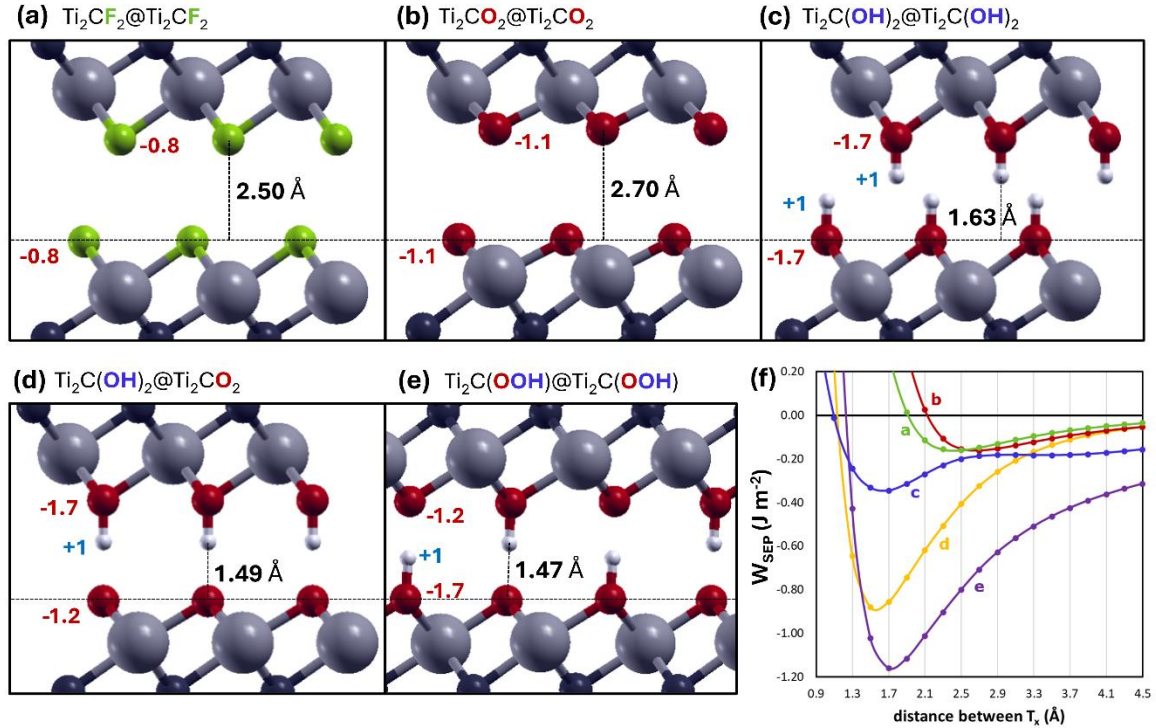


Figure 2.4: Optimized configurations of stacked MXenes with equilibrium distances and partial atomic charges of the terminations (expressed as a fraction of elementary charge unit “e”). (a)-(c) $\text{Ti}_2\text{CT}_2@ \text{Ti}_2\text{CT}_2$ interfaces with homogeneous terminations having different terminations including $\text{T} = \text{F}$ or O or OH . (d) refers to the heterogeneous interface $\text{Ti}_2\text{C}(\text{OH})_2@ \text{Ti}_2\text{CO}_2$, while (e) shows the pairing of MXenes with mixed O and OH terminations ($\text{Ti}_2\text{COOH}@ \text{Ti}_2\text{COOH}$). The partial charges of the innermost atoms range between $(+1.6\text{e})$ - $(+2.0\text{e})$ for Ti , and (-1.9e) - (-1.7e) for C , respectively, depending on the electronegativity of the termination. (f) Summary of the perpendicular potential energy surfaces (pPES) for all systems considered.

The presence of $-\text{OH}$ terminations, instead, induces a further dipole-dipole interaction between the layer terminations, which is not present for $-\text{O}$ and $-\text{F}$ terminations (**Figure 2.4c**). This additional attractive interaction moves both MXene layers closer to each other, while increasing W_{SEP} . In **Figure 2.4d-e**, the schematics of hetero- and mixed-interfaces with $-\text{OH}$ and $-\text{O}$ terminations are shown. The explanation for the higher W_{SEP} calculated for these systems lies in the formation of hydrogen bonds between the hydroxyl group (H-bond donor) and oxygen atoms (H-bond acceptor), leading to a reduced interlayer distance of about 1.5 \AA . The presence of H-bonds is also confirmed by the increase in the negative partial charge of oxygen atoms acting as H-bond acceptors (-1.2e in **Figure 2.4d-e** instead of -1.1e observed for the Ti_2CO_2 bilayer in **Figure 2.4b**). In **Figure 2.4f**, we reported W_{SEP} as a function of the

interlayer spacing. It becomes evident that the termination controls the nature of the layer attraction from pure dispersive (**Figure 2.4a-b**) to dipole-dipole (**Figure 2.4c**) and hydrogen-bonding (**Figure 2.4d-e**) interactions.

These results point towards the relevance of mixed terminations, which have not been considered in previous computational studies of MXenes' tribology. Li et al. measured the adhesion energy between Ti_2CT_x bilayers with atomic force microscopy (AFM),¹⁷⁰ finding W_{SEP} of about 0.6 J m^{-2} . This experimental value can only be compared to the average W_{SEP} calculated for MXenes with mixed surface terminations, i.e., 0.52 J m^{-2} . The slight difference between the experimental and calculated values probably relates to vacancy defects, which were not considered in our models, although being present in realistic surfaces.¹⁴⁵ Moreover, our calculations indicate that the interaction between MXene layers can be tailored by reducing the $-\text{OH}$ concentration on the surface. The respective interaction can be weakened down to values that are lower than those obtained for well-established solid lubricants such as graphene and MoS_2 (**Figure 2.3a**). We anticipate that this is a critical finding as the control of the distribution of terminations during synthesis and post-synthesis treatments would mark a turning point in the application of MXenes for tribological applications.

2.3.1.2 Potential Energy Surface (PES) and PES corrugation

Figure 2.5a shows the potential corrugation ΔW_{SEP} for homogeneous and heterogeneous MXene interfaces without any external load applied. In this regard, ΔW_{SEP} represents the maximum energy barrier that needs to be overcome during sliding of two adjacent MXene layers. Concerning homo-interfaces, F- and O-terminated MXenes have similar PESes with a low potential corrugation, ΔW_{SEP} , of about $0.06\text{-}0.07 \text{ J m}^{-2}$, which is as low as the corrugation of graphene and lower than that of MoS_2 bilayers. No difference can be observed between Ti_2CT_2 and Ti_2NT_2 for T being $-\text{F}$ or $-\text{O}$, as previously observed for W_{SEP} . Conversely, the potential corrugation for bilayers containing only $-\text{OH}$ groups depend on the C/N ratio. At 0.01 J m^{-2} , $\text{Ti}_2\text{N}(\text{OH})_2$ has the lowest potential corrugation among all MXenes and is significantly lower than that of the $\text{Ti}_2\text{C}(\text{OH})_2$ at 0.23 J m^{-2} .

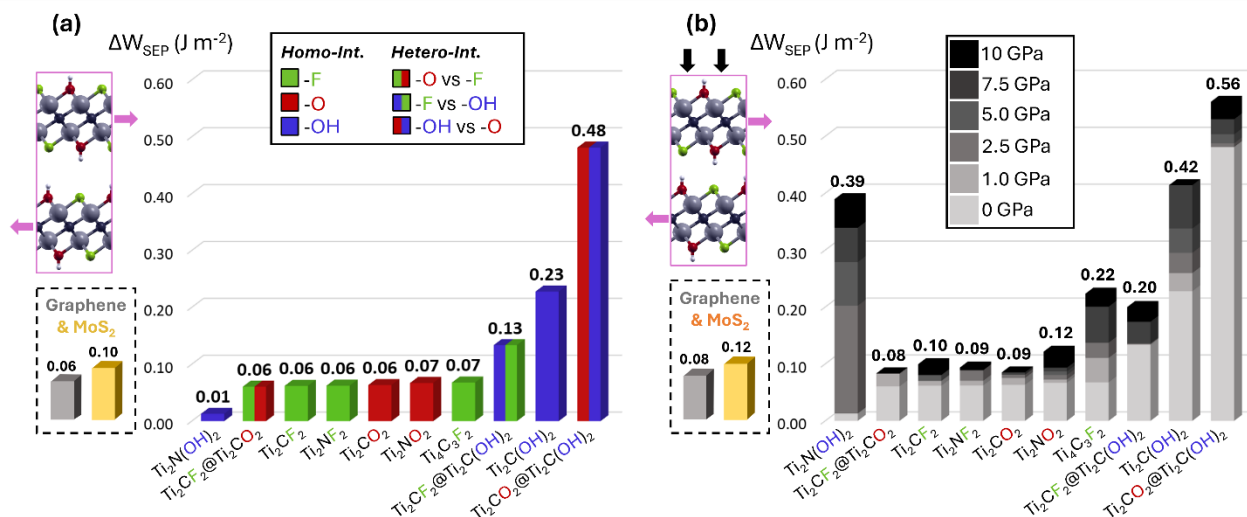


Figure 2.5: (a) PES corrugation values for homogeneous (solid color bars) and heterogeneous (vertical line pattern) interfaces. Green color refers to MXenes with –F terminations, red color stands for –O, while blue color represents –OH. (b) PES corrugation growth as a function of the normal load applied. The grey-scale coding reflects the applied load with a maximum of 10 GPa. ΔW_{SEP} values for graphene and MoS₂ bilayers refer to normal loads of (a) 0 GPa and (b) 10 GPa.

The bars with the vertical-line pattern in **Figure 2.5a** refer to hetero-interfaces. We notice that the combined presence of –OH with –F/–O increases the PES corrugation values. The high potential corrugation observed for Ti₂CO₂@Ti₂C(OH)₂ (0.48 J m^{–2}) is consistent with the strong directionality of the hydrogen bonding interaction (unlike dispersive forces). In this regard, to make the layers sliding, all the hydrogen bonds at the interface must be completely broken to induce sliding of adjacent layer before being reformed, thus generating high energetic barriers. This also happens for Ti₂CF₂@Ti₂C(OH)₂, but as the interaction between –OH and –F is weaker, the energetic barrier is lower (0.13 J m^{–2}).

Figure 2.5b shows the variation of the potential corrugation as a function of the normal load applied to the upper slab of the MXene bilayer. Bars are organized from left to right based on the ΔW_{SEP} value at 0 GPa, and every increment is shown on a grey scale. Due to compressive forces, the corrugations increase with load, which is more consistently seen for the bilayers containing –OH groups at the interface. For loads above 2.5 GPa, the behavior of Ti₂N(OH)₂ gets closer to its carbon-based analogue Ti₂C(OH)₂. Among F- and O-terminated MXenes, Ti₄C₃F₂ is the only candidate, for which the energy barrier increases with pressure, whereas the thinner bilayers keep their ΔW_{SEP} values almost constant, which aligns well with the findings for graphene and MoS₂.

Finally, **Figure 2.6** demonstrates the PES experienced during sliding for two homogeneous bilayers: Ti₂C(OH)₂ and Ti₂CF₂. For Ti₂C(OH)₂, we observe a color change towards red when moving at higher loads. This clearly implies an increase in the potential corrugation with the load. In contrast, the external pressure does not induce large variations in the corrugation for

Ti_2CF_2 . However, it is worth mentioning that minor electronic effects on the PES motif can be seen. Further charge density analysis is necessary to clarify the origin of these peculiar PES features, which is beyond the scope of this contribution.

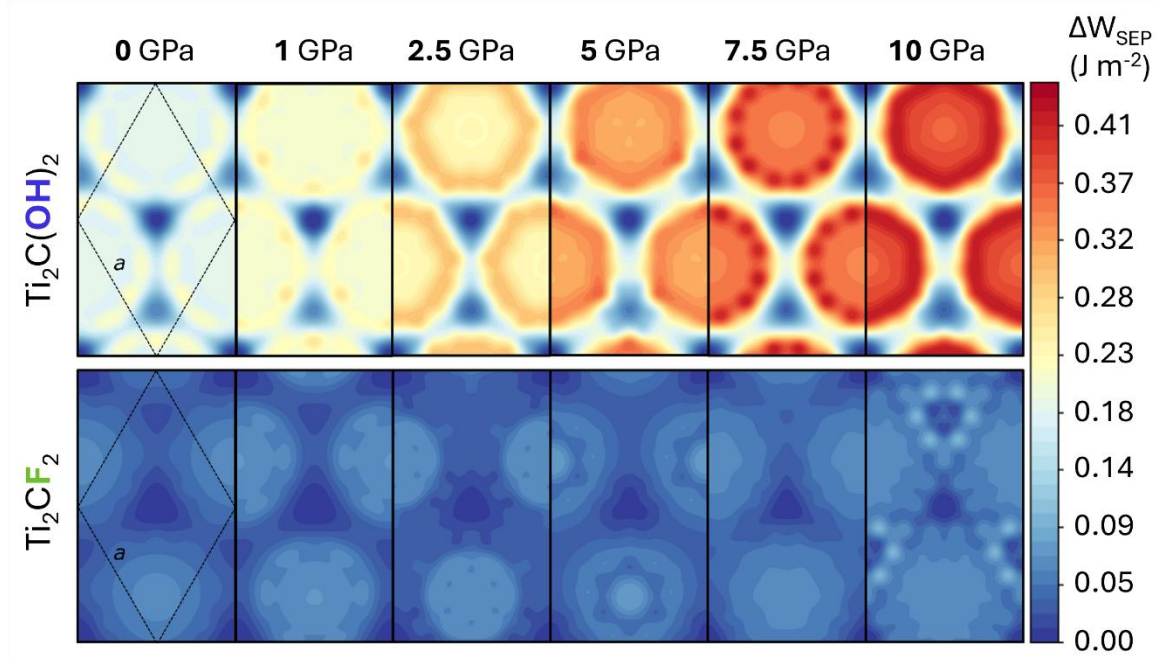


Figure 2.6: Potential energy surfaces for the sliding motion of $\text{Ti}_2\text{C}(\text{OH})_2$ (above) and Ti_2CF_2 (below) bilayers, from zero to 10 GPa load. The color scale is the same for both MXenes. The hexagonal unit cell is schematically shown with black lines in the panels on the very left-hand side.

Since both quantities explored and evaluated in this study (i.e., adhesion and potential corrugation) can be correlated to the shear strength of materials,^{105,112} we hypothesize that MXenes' interfacial properties can be tailored by manipulating the existing surface terminations. Especially, we theoretically predicted that reducing/limiting $-\text{OH}$ groups lead to reduced bilayer adhesion. This fundamentally impacts MXenes' synthesis and delamination approaches because a reduced bilayer adhesion also implies a reduced energy for delamination. Moreover, we anticipate that MXenes' tribological performance can be further optimized by controlling and tailoring the existing surface terminations. We hypothesize that by limiting the percentage of $-\text{OH}$ groups, MXenes can provide similar or even better lubricity as other 2D-materials such as graphene or MoS_2 .

2.3.2 Adhesion to ferrous substrates

In this section, we unravel MXenes' interaction with ferrous substrates, e.g., iron and hematite (Fe_2O_3). We considered the effect of homogenous $-\text{F}$, $-\text{O}$ and $-\text{OH}$ terminations on both substrates. We also investigated mixed terminations for the iron substrate. The optimized adsorption configurations are shown in **Figure 2.7**, where the adhesion energies are also reported. The dispersive ($-\text{D}$) contribution to W_{SEP} is explicitly indicated to provide an

estimate of the physical forces acting across the interface. The transfer of electronic charge occurring upon layer deposition is also reported. It has been shown that this electronic property correlates very well with interfacial adhesion.¹⁰⁵ The results indicate that Ti_2CF_2 is highly inert and adheres to iron and hematite only via dispersion forces. The long interfacial distance, the minimal charge perturbation occurring with the interface formation, and the predominance of the -D component (reported in brackets in **Figure 2.7a**) support this interpretation. Ti_2CO_2 and $\text{Ti}_2\text{C}(\text{OH})_2$ chemisorb on iron as indicated by the higher value of W_{SEP} . This outcome arises from different electronic effects occurring across the interface (**Figure 2.7b**). Ti_2CO_2 partially oxidizes the topmost Fe layer, inducing a relevant charge flow from the substrate to the lubricant. Instead, $\text{Ti}_2\text{C}(\text{OH})_2$ injects charge into the substrate (**Figure 2.7c**), which induces a partial reduction of superficial Fe atoms. Similar effects are observed for the hematite substrates (**Figure 2.7d-f**). In this case, $\text{Ti}_2\text{C}(\text{OH})_2$ transfers both charge and mass (two H atoms per cell) to the substrate, establishing short and strong H-bonds across the interface and leading to a high value of W_{SEP} . A relevant charge transfer occurs at the interface for interfacial distances below 2 Å, independently from the nature of the interactions. In contrast, for larger distances, the charge transfer between the mated surfaces is hindered.

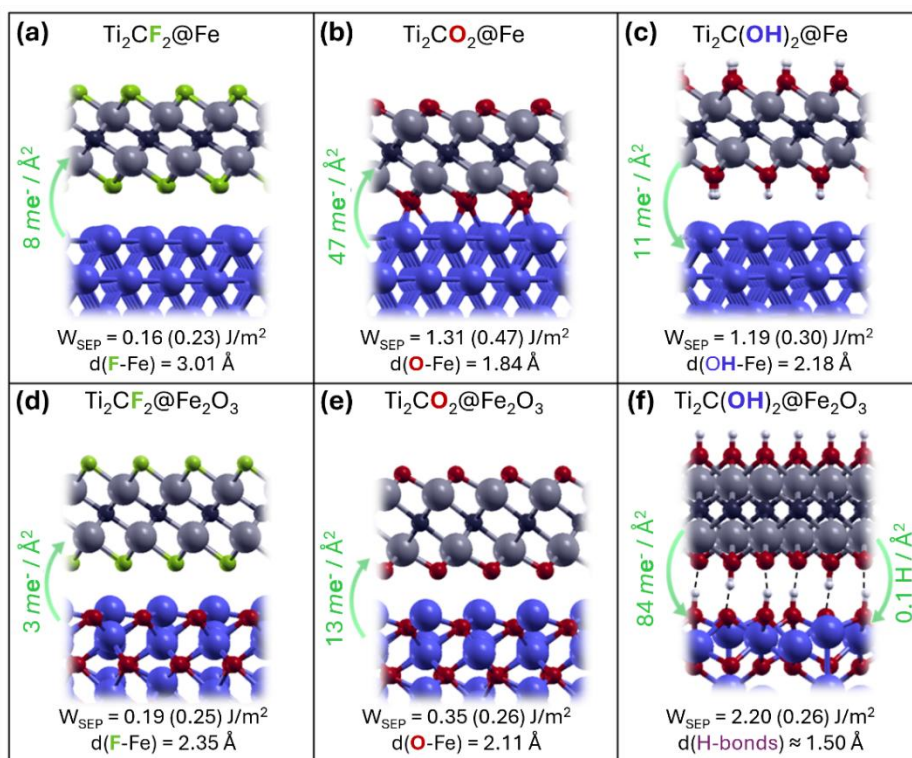


Figure 2.7: MXenes with -F, -O, and -OH terminations interacting with (a)-(c) pristine iron (Fe), and (d)-(f) hematite surfaces (Fe_2O_3). W_{SEP} is reported together with the pure dispersive contribution in brackets. The equilibrium distance, d , is reported along with the overall charge/matter transfer (green arrows). The atoms are colored as in the previous figures, while the Fe atoms in blue. Dotted lines indicate H bonds. Please note that the $\text{Ti}_2\text{C}(\text{OH})_2@ \text{Fe}_2\text{O}_3$ view is rotated by 30° around the z axes.

An effective solid lubricant should well adhere to the substrate to resist peeling-off during rubbing, but it should also be able to effectively reduce the metal-metal interaction at the micro-asperity contacts. The latter property can be estimated by calculating the reduction of the metal-metal adhesion that is obtained by covering one of the two mating surfaces with a MXenes layer. The results of this analysis are shown in **Figure 2.8**, where the MXenes adhesion on the substrates is also reported for comparison.

We observe that $\text{Ti}_2\text{C}(\text{OH})_2$ MXenes present high adhesion on the substrate (**Figure 2.8a**), but it poorly lubricates hematite-hematite contacts (**Figure 2.8b**) due to strong H-bond formation across the interface. Ti_2CF_2 MXenes demonstrates an outstanding lubricant capability, but weakly bind to both substrates considered (**Figure 2.8a**). The adhesion on ferrous surfaces is lower compared to graphene, suggesting a fast removal from the contact zone during rubbing. Interestingly, Ti_2CO_2 adheres to the substrate similarly to MoS_2 , and even better than graphene. It also efficiently lubricates the ferrous substrates considered, thus representing the best performing MXene termination among those considered (**Figure 2.8b**). The results obtained for the adsorption of MXenes with mixed termination on iron indicate that the simultaneous presence of $-\text{O}$ $-\text{OH}$ and $-\text{F}$ atoms reduces the layer adhesion to the substrate (**Figure 2.8a**) and enhance the adhesion-reduction capability (**Figure 2.8b**). The values of W_{SEP} and W_{SEP} -reduction for the mixed cases are very close to the averages of the corresponding homogenous cases. Intermixing $-\text{O}$ and $-\text{OH}$ produces, instead, lower adhesion and higher adhesion reduction than expected, considering the average values obtained for the corresponding homogeneous surfaces.

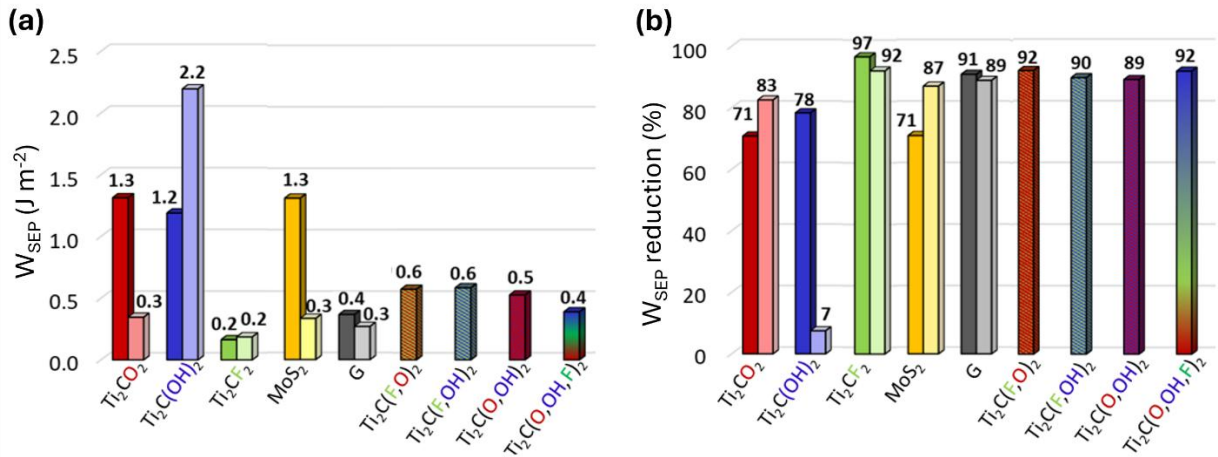


Figure 2.8: (a) W_{SEP} of MXenes with different terminations on Fe (dark color) and Fe_2O_3 (pale color). (b) Efficiency of MXenes in reducing the substrate-countersurface adhesion reported as percentage reduction of W_{SEP} with respect to the sealed Fe-Fe and Fe_2O_3 - Fe_2O_3 interfaces. The corresponding values obtained for MoS_2 and graphene are shown for comparison. Results for mixed termination are reported for Fe only.

2.3.3 The problem of water-induced oxidation

For many applications, the precise understanding of the wettability of 2D materials is essential to improve their functionality. It is well known that the properties of 2D materials depend on environmental conditions.^{171,172} For instance, the presence of water promotes low-friction sliding between graphene layers, while it worsens the tribological performance of molybdenum disulfide (MoS₂).^{31,173} The influence of humidity on the tribological behavior has been also investigated for Ti₃C₂T_x multi-layer coatings by Marian et al.,⁸⁶ finding that the friction and wear performance is detrimental for higher relative humidities. It is well accepted that MXenes show an intrinsic hydrophilicity, mainly attributable to the presence of hydroxyl, oxygen and fluorine terminations.³⁷ However, the hydrophilicity of this family of 2D materials has been scarcely investigated with both experimental and computational approaches.^{174–176} Contact angle measurements reveal that the wettability of MXenes is not homogeneous but can vary depending on local surface features as well as the presence of contaminations.¹⁷⁴ Apart from these general conclusions, a complete characterization of MXenes' hydrophilicity is lacking.

Another important issue concerning the interaction of MXenes with water relates to their degradative oxidation. This phenomenon, spontaneously occurring under ambient conditions, inevitably compromises the synthesis and subsequent applicability of MXenes.^{137,138} Many experiments and calculations have confirmed the intrinsic tendency of MXenes to transform into oxides, while harsh conditions tend to accelerate this process.^{177–181} Several factors affecting the oxidation rate of MXenes have been investigated, such as layer microstructure and atmosphere/solvent composition.¹³⁷ One of the critical factors in stability of MXenes is to know which oxidant species (O₂ or H₂O) is mainly responsible for the degradative process. In earlier studies, oxygen dissolved in MXenes' colloidal solutions was thought to play the major role.¹⁸¹ However, recent studies on oxidation kinetics performed by ultraviolet-visible and Raman spectroscopy revealed that water seems to be the key component leading to degradation.¹⁸² Recently, atomistic insights on MXenes' oxidation in aqueous solutions were provided by means of first principle molecular dynamics (MD) simulations.¹⁷⁶ Their results strongly support the experimental observation that water is an oxidant, which is strong enough to attack and degrade MXenes.

In this context, fundamental aspects regarding the interaction of MXenes with water need to be unraveled. The characterization of hydrophilicity for different sites, both defective and not, can be a starting point for further investigations. In this work, we exploit DFT calculations to study the interaction of H₂O with Ti-based MXenes (Ti_{n+1}X_nT₂). We mapped the hydrophilicity of defect-free surfaces by varying the termination type (T), the carbon/nitrogen ratio (X), as well as the layer thickness (*n*). The analysis is repeated for defective MXene flakes, as they are known for being prone to oxidation.^{183,184} The role of single atomic vacancies, cluster of defects, and edges in promoting the chemisorption of water is addressed and explained, focusing on both energetical and structural aspects. Since MXene surfaces are usually

terminated with a random distribution of $-F$, $-O$ and $-OH$ groups,^{128–130,184} we also map the hydrophilic areas for mixed terminated MXenes.

2.3.4 MXene hydrophilicity – effect of defects and edges

The hydrophilic character of a material at the atomistic level can be related to the energy gain associated with the adsorption of water molecules. Energy gains related to the adsorption of a single water molecule are displayed for the defect-free (**Figure 2.9a**) and single vacancy-containing MXenes (**Figure 2.9b**). We studied Ti_2XT_2 as the example MXene and investigated the effect of the surface termination ($T = F, O$ and OH), carbide vs nitride ($X = C$ and N), and the presence of vacancy on the metal site (V_{Ti}), on the X site ($V_{C/N}$) and the surface termination sites (V_T). We also studied MXenes with a higher thickness (i.e., $Ti_4C_3F_2$) but only to a limited extent, due to the increased computational effort required for simulating these larger systems. However, it is known that adsorption phenomena mainly affect the atoms closest to the surface, which agrees with our findings. Therefore, no remarkable differences were found when switching from a thinner MXene (Ti_2CF_2) to a thicker analogous ($Ti_4C_3F_2$).

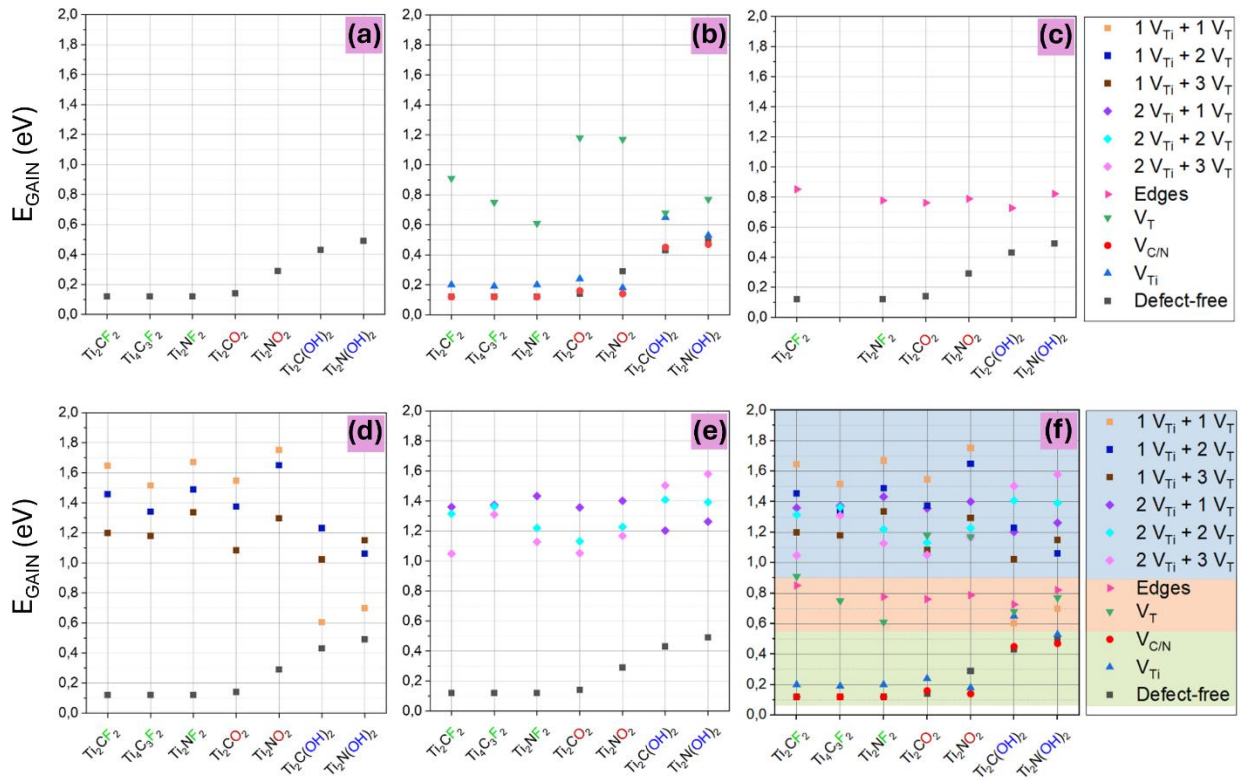


Figure 2.9: Absolute values of the adsorption energy of one single water molecule on different types of MXenes: (a) defect-free surfaces, (b) surfaces with single vacancy of C/N ($V_{C/N}$), Ti (V_{Ti}) or termination (V_T), (c) edges, (d)-(e) surfaces with cluster of defects ($pV_{Ti} + qV_T$), consisting of p Ti vacancies and q termination vacancies. Panel (f) summarizes all cases considered. The highlighted intervals reflect the extent of the interaction with water: blue stands for strong chemisorption and green reflects physisorption, while red points to an intermediate behavior.

The fully terminated surfaces interact with water via hydrogen bonds. Fluorine and oxygen terminations can act as weak H-bond acceptors, while hydroxyls can also play the role of the donor. This behavior leads to an increase in the energy gain by moving from $-F$ and $-O$ (0.12-0.29 eV) to $-OH$ (0.43-0.49 eV) terminated surfaces (**Figure 2.9a**). In any case, adsorption energies of H_2O are greater on MXene monolayers compared to other 2D materials such as graphene or MoS_2 (0.12-0.15 eV),¹⁸⁵ demonstrating their intrinsic hydrophilic behavior.

In general, the removal of an atom from a surface (i.e., single vacancy) was supposed to enhance its reactivity towards water adsorption.¹⁸⁶ However, for the internal MXene vacancies, including C/N vacancies ($V_{C/N}$ shown as red circles in **Figure 2.9b**) and Ti vacancies (V_{Ti} , shown as blue triangles), the interaction with H_2O appears to be almost the same as for the defect-free MXenes. The negligible change in energy could be explained by the fact that the water molecule is not small enough to approach these internal defects, resulting in negligible stabilization. In the case of termination vacancies (V_T , shown as green triangles in **Figure 2.9b**), the dangling bonds of the underlying Ti atoms make the surface extremely reactive. The oxygen atom of H_2O can physically fill the hole left by the missing T, and due to its two lone pairs, it can provide stability to the undercoordinated Ti atoms. For the T-vacancy, the associated energy gains range from 0.61 eV to 1.18 eV, depending on the reactivity of the MXene. It is worth noting that the water adsorption energy on MXene surfaces with T-vacancy is comparable to that of titanium dioxide (TiO_2) reported in literature. The most common polymorphs of TiO_2 , anatase and rutile, are both composed of distorted TiO_6 octahedra, with the Ti atoms showing octahedral coordination similar to MXene layers. As reported in Ref.¹⁸⁷, water interacts with the anatase (101) and rutile (110) crystal faces through the coordination of the water oxygen atom to the outermost Ti atoms. Indeed, the exposed Ti atoms are undercoordinated (5-fold-coordinated), thus prone to being stabilized by the oxygen atom of water. Interestingly, based on DFT calculations,^{188,189} the water adsorption on the (101) crystal face of anatase and (110) face of rutile is found to be 0.84 and 0.94 eV, respectively, which is within the E_{GAIN} energy range observed for MXene' surfaces with defects.

As the next step in our analysis, we considered the water interaction with MXene edges, as reported in **Figure 2.9c**. At the MXene edges, the outermost Ti atoms have lost their typical octahedral geometry, which become defects sites that can interact with H_2O . Because the edges are mainly undercoordinated Ti atoms, the strength of the interaction is almost independent of the MXene composition, ranging between 0.73 eV and 0.85 eV (red triangles in **Figure 2.9c**). This finding agrees with the fact that in almost all MXenes, 2D flakes' edge oxidation can be observed during storage regardless of the flake composition and the number of transition metal layers (n) in MXene, and edge capping has been utilized as a way to slow down the oxidation.^{190,191}

Finally, the energy gains concerning H_2O interacting with a cluster of defects are presented in **Figure 2.9d-e**. We explored a wide range of 2D flakes consisting of a single (or double) Ti vacancy and one, two and three termination vacancies. Generally, all energy gains are greater

than 1.00 eV, suggesting the strong chemisorption of the water. Some exceptions are found for those layers functionalized with $-\text{OH}$ with one Ti vacancy (**Figure 2.9d**), that are not reactive enough to promote the chemisorption of water. This peculiar deviation between $-\text{OH}$ and $-\text{F}/-\text{O}$ terminated MXene flakes will be addressed in detail soon.

Figure 2.9f shows a collective representation of the water adsorption energies on MXene flakes, from defect-free to vacancy clusters. We divided the energy values into three regions, according to the nature and strength of the molecule-surface interaction. The green region ranging between 0.10 to 0.55 eV includes pure physisorption of water via hydrogen bonds. For E_{GAIN} greater than 0.60 eV, the oxygen of water establishes chemical bond(s) with the undercoordinated Ti atom(s) of the surface, leading to chemisorption. We distinguished a weak chemisorption, $0.6 \text{ eV} < E_{\text{GAIN}} < 1.0 \text{ eV}$ (red region), from a stronger chemisorption, E_{GAIN} above 1.00 eV (blue region). Defect-free MXenes and single vacancies of Ti and C/N (in green) lead to adsorption energies that are mainly affected by the type of termination (T). For these surfaces, the interaction with water does not exceed 0.55 eV (green region). Intermediate energy values (0.60-0.90 eV) are mainly found for water on single-termination vacancies and edges. In contrast, the energy range associated with clusters of vacancies (0.90-1.80 eV), highlighted in blue, is the highest among all and compatible with strong chemisorption of water (i.e., shorter Ti- OH_2 bond distances). **Figure 2.9f** identifies defect clusters as the sites interacting more strongly with the H_2O molecule irrespective of the termination type and the carbon/nitrogen content. Insights into the interaction between H_2O and MXene layers are discussed in the following sections.

Water on defect-free surfaces.

The optimized adsorption configurations of water on defect-free surfaces are illustrated for Ti_2CO_2 and $\text{Ti}_2\text{C}(\text{OH})_2$ in **Figure 2.10a,b**. For these MXene surfaces, the role of layer thickness and carbon/nitrogen content are negligible compared to the effect induced by the termination. In particular, $-\text{F}$ and $-\text{O}$ behave similarly, acting as weak acceptors of hydrogen bonds. Due to the electrostatic repulsion between the passivating groups and the oxygen of water, only a slight approach is allowed (**Figure 2.10a**). Therefore, long-distance H-bonds are established (the distances between H_2O and $-\text{F}$ and $-\text{O}$ terminations are in the range 2.34-2.43 Å), resulting in weak interactions. In contrast, $-\text{OH}$ terminations (**Figure 2.10b**) can act as donors of hydrogen bonds, leading to shorter distances (1.97-2.03 Å) and stronger interactions.

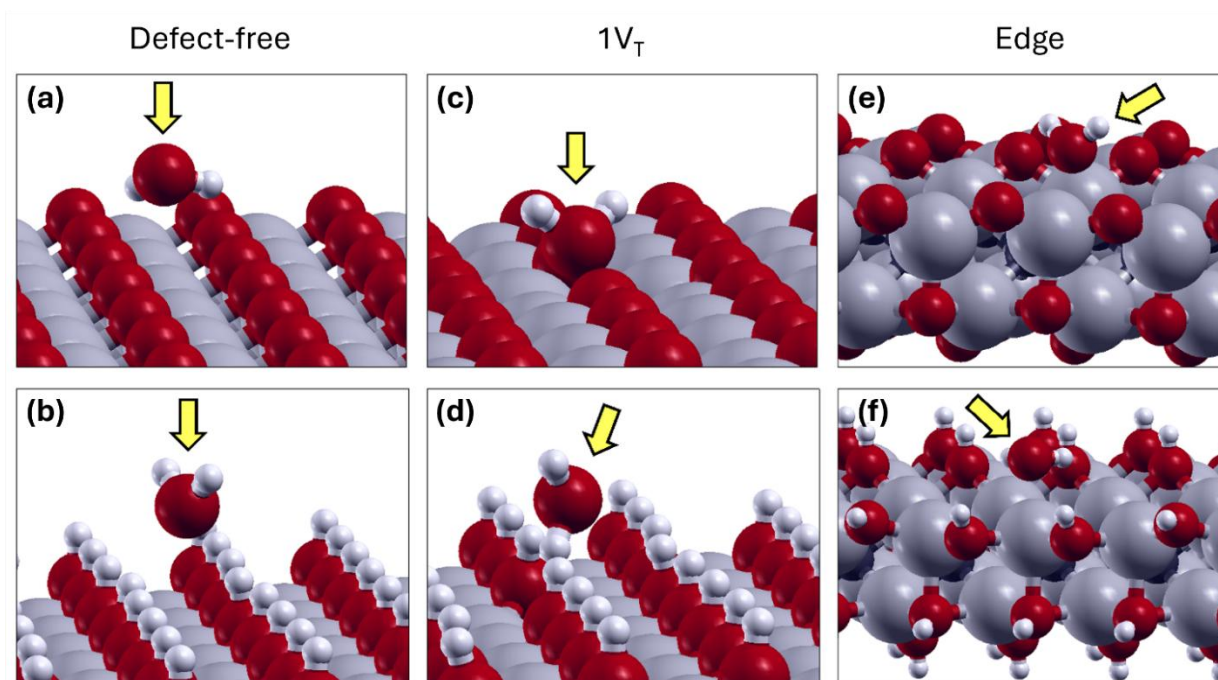


Figure 2.10: Perspective view of the optimized configuration of H_2O interacting with (a)-(b) defect-free MXenes, (c)-(d) surfaces with a vacancy of termination (V_T), and (e)-(f) edge of ribbons. Ti_2CO_2 (above) and $\text{Ti}_2\text{C}(\text{OH})_2$ (below) are taken as examples. The yellow arrow highlights the presence of the water molecule. Ti atoms are shown in gray, O in red, C in black and H in white.

Water on single-vacancy.

Single vacancy sites were modeled by removing the atoms closest to the surface, in three types, V_T , V_{Ti} and $V_{\text{C/N}}$ representing a surface with a vacancy of termination, titanium, and carbon/nitrogen, respectively. In **Figure 2.10c-d**, we show the optimized configurations of the water molecule on Ti_2CO_2 and $\text{Ti}_2\text{C}(\text{OH})_2$ surfaces with a missing termination (V_T). Neither $V_{\text{C/N}}$ nor V_{Ti} notably affects the interaction energy with water compared to defect-free surfaces. However, the optimal H-bond distance was found to vary on defective surfaces and followed a specific trend. Taking Ti_2NF_2 as an example, the average H-bond distance is 2.37 Å, 2.33 Å and 2.20 Å for a defect-free surface, $V_{\text{C/N}}$ and V_{Ti} , respectively. Generally, the same optimized orientation of H_2O was found when interacting with F- and O-terminated nitrides and carbides. This characteristic probably relates to the similar physical-chemical properties (e.g., high electronegativity, H-bonds acceptor capability) of both terminations. Moreover, OH-terminated carbides and nitrides retain a similar behavior to each other as well.

The reactivity towards water can be notably increased in the presence of surface termination vacancies (V_T), favoring the transition from physisorption to chemisorption (green triangles in **Figure 2.9b**). The absence of one surface termination causes undercoordination of the three surrounding Ti atoms. Some of these dangling bonds can be saturated by the lone pairs of the oxygen atom of water. However, only for surfaces terminated with –F and –O, water can approach the Ti-atoms (**Figure 2.10c**). In contrast, for surfaces with a single OH-vacancy

in $\text{Ti}_2\text{N}(\text{OH})_2$ and $\text{Ti}_2\text{C}(\text{OH})_2$, hydroxyl groups close to the V_T defect tend to trap H_2O into a H-bond network, before reaching the chemisorption site (**Figure 2.10d**). The chemisorption values vary between 0.61 eV 1.18 eV for F- and O-terminated surfaces, while the absolute values depend on various factors. We identified three main contributions to this variation: i) the residual positive atomic charge of the undercoordinated Ti atoms, ii) the equilibrium distance between the oxygen atom of water and titanium, iii) the number of Ti atoms stabilized by the water chemisorption. For instance, the energy gains obtained on V_T substrates for Ti_2NF_2 (0.61 eV), Ti_2CF_2 (0.91 eV) and Ti_2NO_2 (1.17 eV) show a correlation with the partial atomic charges of the Ti atoms surrounding the vacancy ($q_{\text{Ti}} = +1.45e, +1.53e, +1.65e$, respectively). Although the high value of q_{Ti} found on $\text{Ti}_4\text{C}_3\text{F}_2$ (+1.60e) and Ti_2CO_2 (+1.79e), for these two MXenes the oxygen atom of H_2O was found to stabilize only one titanium, instead of two. This compensation leads to the energy fluctuation trend shown in **Figure 2.9b**.

Water on edges.

To study the effect of MXene flake edges, we focused on MXene ribbons (1D MXenes). Different reactive sites appear on the edges, depending on the specific cut and reconstruction. However, based on a previous study on MXene nanoribbons,¹⁴⁵ we decided to restrict our study to those nanoribbons that have the lowest formation energy, thus showing the highest stability. Therefore, the adsorption values collected in **Figure 2.9c**, ranging between 0.73 eV and 0.85 eV, can be considered as the lower limit that can easily increase in presence of more unstable edges. The main geometrical feature of the MXene edge (nanoribbons) is a distortion of the chemical bonds between Ti atoms and surface terminations. At the edge, the classical octahedral geometry is lost for the outermost Ti atoms, leading to an unconventional distorted tetrahedral coordination (**Figure 2.1f**).

The configurations of water interacting with MXene edges (1D-MXenes $\text{Ti}_8\text{C}_3\text{O}_8$ and $\text{Ti}_8\text{C}_3(\text{OH})_8$) are provided in **Figure 2.10e-f**. The defective undercoordinated Ti atom along the edges constitutes the most reactive site to interact with water. Regardless of the termination type and C/N content, the oxygen of water interacts with one or two undercoordinated Ti atom(s), similarly to the MXene flake with a termination vacancy (V_T). We found that the energy gain mainly depends on the H_2O – Ti distance, the number of Ti atoms involved, and the H_2O -assisted reconstruction of the edge. In most cases (including **Figure 2.10f**), water interacts with a single titanium atom, with a narrow H_2O –Ti distances distribution (2.25 Å - 2.31 Å). In other cases (**Figure 2.10e**), H_2O prefers to interact with two Ti atoms, leading to an increase in the average distance.

Water on vacancy clusters.

Various combinations of titanium (V_{Ti}) and termination (V_T) vacancies were considered as defect clusters ($pV_{\text{Ti}}+qV_T$), exploring $p = 1, 2$ and $q = 1, 2, 3$. In **Figure 2.11**, we only focus on single Ti vacancy cases ($p=1$) with vacancy clusters on surface terminations ($q = 1,2,3$), providing the optimized configurations for two representative materials, i.e., Ti_2CF_2 and

$\text{Ti}_2\text{C}(\text{OH})_2$. For vacancy clusters ($1V_{\text{Ti}}+qV_{\text{T}}$) on O- and F-terminated MXenes (upper series in **Figure 2.11**), the H_2O molecule provides two strong stabilizing effects. First, the oxygen atom of water saturates a V_{T} , interacting with the remaining two surrounding Ti atoms. Moreover, one H of the water can point towards the hole left by V_{Ti} . With the lack of a titanium atom, many T and C/N atoms become undercoordinated, leading to a densification of the negative charge centered on the V_{Ti} defect. This excess of charge density is mitigated when one of the two positively charged hydrogens of H_2O is pointed towards the hole. It is worth noting that the excess of charge density is reduced with an increasing number of V_{T} . In other words, when a V_{Ti} is formed, the more neighboring terminations are missing, the less reactive the surface will be.

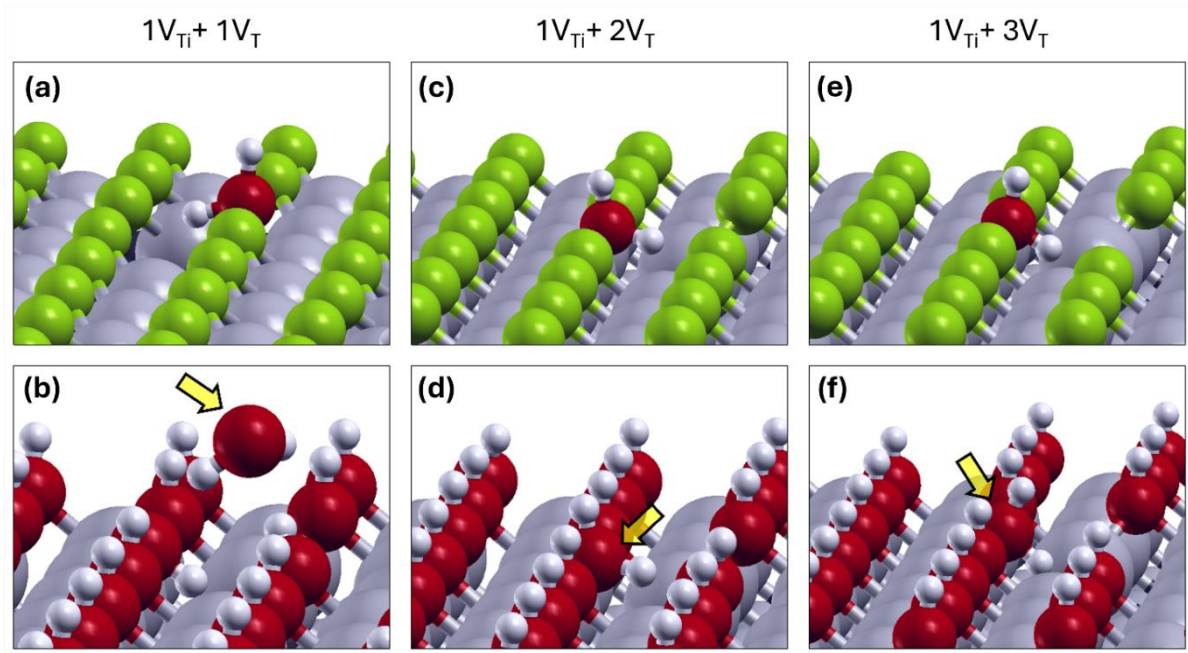


Figure 2.11: Optimized configurations of H_2O adsorbed on different clusters of vacancies for Ti_2CF_2 (above) and $\text{Ti}_2\text{C}(\text{OH})_2$ (below). The clusters of defects consist of one titanium vacancy and up to three termination vacancies, as $1V_{\text{Ti}}+1V_{\text{T}}$ (a)-(b), $1V_{\text{Ti}}+2V_{\text{T}}$ (c)-(d) and $1V_{\text{Ti}}+3V_{\text{T}}$ (e)-(f). The yellow arrow highlights the presence of the water molecule interacting with the defected $\text{Ti}_2\text{C}(\text{OH})_2$ surface.

For OH-terminated MXenes (lower series in **Figure 2.11**), similar configurations are found, except for $1V_{\text{Ti}}+1V_{\text{T}}$ cluster. This peculiar defect (**Figure 2.11b**) is already stabilized without the necessity of interacting with the water molecule. Due to the lack of a titanium atom, the surrounding hydroxyl terminations can rotate and point the hydrogens towards the hole. When the number of terminations surrounding the V_{Ti} is further reduced (**Figure 2.11d** and **f**), the configuration becomes closer to the one observed for F- and O-terminated materials.

These considerations also explain the energy value trends in **Figure 2.9d**. All energy gains are greater than 1.00 eV, except for the $1V_{\text{Ti}}+1V_{\text{T}}$ clusters on OH-terminated surfaces, where the re-orientation of hydroxyls reduces their reactivity. Furthermore, for O- and F-terminated

surfaces, the energy gains related to the water chemisorption on $1V_{Ti}+qV_T$ clusters decrease with increasing q due to the loss of reactivity explained before. However, energy fluctuations may also result from the complex interplay between other factors. The average distance between the oxygen atom of water and Ti atoms, as well as the positive atomic charge on Ti atoms, are also found to affect the extent of the water chemisorption.

The chemisorption of water on $2V_{Ti}+qV_T$ clusters ($q = 1, 2, 3$) is regulated by almost the same mechanisms discussed above for the $1V_{Ti}+qV_T$ clusters. The main difference lies in the number of undercoordinated Ti atoms stabilized by the oxygen atom of H_2O . In the case of $2V_{Ti}+qV_T$, indeed, the presence of a double V_{Ti} leaves only one titanium atom with dangling bonds and leads to smaller energy gains compared to $1V_{Ti}+qV_T$ (**Figure 2.9e**). The energy gains related to the chemisorption of water for $2V_{Ti}+qV_T$ are still greater than 1 eV. This can be explained by the fact that even if H_2O interacts with only one Ti atom, the H_2O -Ti bond distance is reduced, becoming comparable to the typical bond distance between Ti and T in a defect-free layer.

Water on mixed-terminated surface.

It is known that as synthesized MXene surfaces are generally covered by a mixture of randomly distributed surface terminations.^{128–130,184} To gain a better understanding of MXenes oxidation, we investigated the interaction of water with a Ti_2CT_x layer simultaneously passivated with $-F$, $-O$ and $-OH$ (in a stoichiometric ratio of about one-third each). The hydrophilicity map of Ti_2CT_2 (**Figure 2.12**), was built after performing 96 separate relaxations, trying to sample all the supercell areas in a uniform way. For each optimized configuration, we collected the final position of H_2O (i.e., average x and y coordinates, tiny black dots in **Figure 2.12**), as well as the associated energy gain (blue-white scale). As a result, we created the hydrophilicity map after making the interpolation on our obtained data points. The solid curved lines in black identify level curves that connect points with the same hydrophilicity (i.e., energy gain).

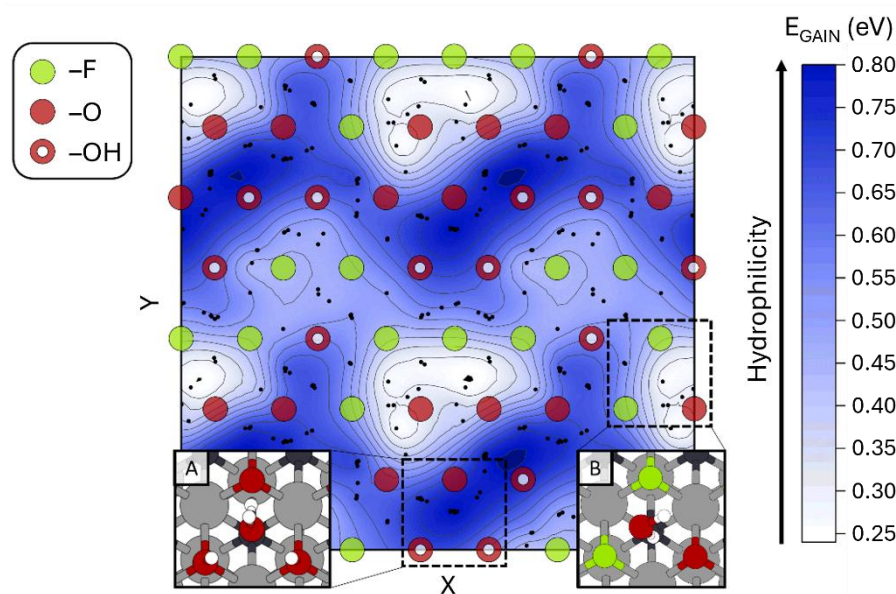


Figure 2.12: Hydrophilicity map of a 2×2 Ti_2CT_2 with mixed terminated surface. The two axes identify the lateral displacement on the surface, referring to the termination positions. Terminations are shown in relief on the map. Hydrophilic regions (blue) are those rich in hydroxyl groups, where hydrogen bond networks are easily formed (inset A). White regions correspond to less hydrophilic areas, where H_2O interacts only moderately with the surface (inset B). Black tiny dots identify the average x and y coordinates of H_2O , for each of the 96 optimized water molecules.

In the hydrophilicity map presented in **Figure 2.12**, dark blue areas highlight strongly hydrophilic areas, while white areas identify those regions that only mildly interact with water. Terminations are superimposed on the map to better appreciate their different contributions to making a surface hydrophilic. In insets A and B, we provide two exemplary configurations, corresponding to an energy gain of 0.80 eV and 0.25 eV, respectively. The unique ability of hydroxyl groups to act as H-bond donors leads to adsorption energy gains, which are always greater than 0.50 eV. Indeed, a higher density of $-\text{OH}$ terminations leads to more interaction with water and greater hydrophilicity. In contrast, $-\text{O}$ and $-\text{F}$ terminations always behave as H-bond acceptors, while oxygen is always preferred whenever possible.

These results can be compared to the case of homogeneously terminated surfaces, for which the maximum adsorption energy gain was found to be ≈ 0.50 eV for $\text{Ti}_2\text{C}(\text{OH})_2$ and $\text{Ti}_2\text{N}(\text{OH})_2$. Consequently, the consideration of a realistic surface having a mixture of surface terminations makes the system even more hydrophilic. Interestingly, the tendency to strongly interact with water is not maximized for a full coverage of hydroxyl groups. A balanced ratio between hydrogen bond donors and acceptors is the key factor in inducing cooperative hydrophilic effects. Although we limited this section to defect-free mixed terminated surfaces, we suppose that a further increase in the interaction with water could arise for defective surfaces.

2.4 Conclusions

In this chapter, we have presented a DFT study providing an in-depth understanding of the interfacial properties and hydrophylicity of Ti-based MXenes, as summarized in **Figure 2.13**. We have performed a huge series of systematic calculations also considering more realistic models for MXenes' surface terminations. Compared to the effects of MXenes' monolayer thicknesses ($n = 1$ to 3) and their C/N ratio, we have demonstrated that surface terminations play the dominant role in determining the interfacial/interlayer properties.

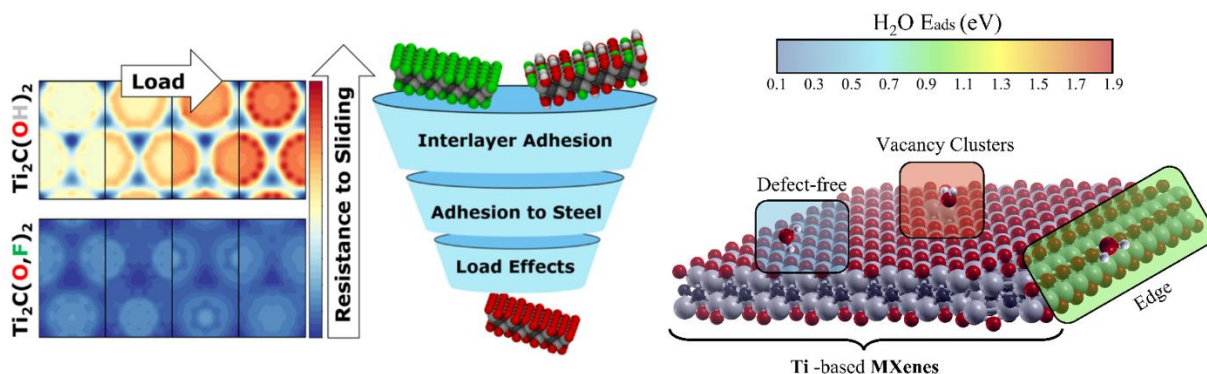


Figure 2.13: Schematic of the most relevant results obtained in this study. The best lubricating performance are achieved by increasing $-O$ terminations while reducing $-OH$. Defects on the MXene surfaces are essential to promote the chemisorption of water, which is the first step towards degradative oxidation, with defect clusters promoting chemisorption more than edges.

In For fully $-F$ and/or $-O$ terminated MXenes, the interlayer interaction is governed by the sum of attractive dispersion forces and electrostatic repulsion between negatively charged surface groups. We anticipate an excellent tribological behavior, close to or even better than the best-performing, state-of-the-art 2D materials (e.g., graphene and MoS_2). In contrast, $-OH$ terminations induce further dipole-dipole interactions between adjacent layers, increasing the interlayer adhesion and the energy demand to induce interlayer sliding. For MXene bilayers with two or three different terminations covering the surface, the W_{SEP} values are not a simple average of the homogeneous cases. Indeed, we found stronger interlayer interactions due to the formation of hydrogen bonds between $-OH$ terminations (H-bond donor) of one layer and $-O$ or $-F$ (H-bond acceptor) of the other layer.

The evaluation of the potential energy corrugation ΔW_{SEP} under an applied external normal load verified that the load-dependence of the resistance to sliding is governed by MXenes' surface terminations. Ti_2XT_2 interfaces (with $X = C/N$, $T_2 = O$ and/or F) behave like graphene and MoS_2 without a notable load dependence of ΔW_{SEP} ranging between 0.06 to 0.12 J m^{-2} . The mixed presence of both $-OH$ and $-F/-O$ terminations leads to high potential corrugation that notably increases with load. The highest ΔW_{SEP} value is observed for the heterogeneous bilayer $Ti_2CO_2@Ti_2C(OH)_2$ (0.48 and 0.56 J/m^2 at 0 and 10 GPa , respectively).

The surface terminations of MXenes also play a crucial role regarding the interaction with underlying substrates (iron and iron oxide, as models for steel). We calculated the layer-substrate adhesion and mated the coated substrate with a countersurface to evaluate the MXenes capability to reduce nano-asperity adhesion. We observe that an increase of $-F$ terminations weakens the adhesion to ferrous substrates, facilitating the lubricant removal under sliding conditions. In contrast, $-OH$ terminations anchor the monolayer to the substrate through H-bonds and electrostatic interactions, although providing less efficient interlayer lubrication. MXenes with $-O$ termination adhere well to ferrous surfaces with a lubricant performance similar to graphene and MoS_2 .

Surface terminations are essential for tuning the MXenes nano-tribological properties. By reducing/limiting $-OH$ groups, we demonstrated reduced interlayer binding, which impacts delamination processes as well as the tribological performances. We also observed that by increasing $-O$ terminations, MXenes can better reduce adhesive friction between ferrous micro-asperities, still adhering to the ferrous substrates and thus reducing the lubricant removal during rubbing. Therefore, we hypothesize that MXenes' properties can be further optimized by controlling the surface terminations either by the etching process, e.g., by minimizing the F-content in MXene etchant or by post-synthesis treatments, for example, by reducing the content of $-OH$ terminations by thermal annealing.

The interaction of Ti-based MXenes with water has been explored as a function of the type of termination, carbon/nitrogen in X, and MXene layer thickness (n). Subsequently, we have unraveled the role of single atomic vacancies, cluster vacancies and stable edges in promoting the chemisorption of water. Our results suggest that H_2O chemisorption on MXene surfaces only occurs in the presence of undercoordinated Ti atoms. The absence of at least one termination group (V_T) resulted in a destabilization of the adjacent Ti atoms, which strongly interacted with the oxygen atom of water to saturate their dangling bonds. On defect-free surfaces and on substrates with a single vacancy of C/N ($V_{C/N}$) or Ti atom (V_{Ti}), H_2O simply physisorbs via the formation of hydrogen bonds with the terminations, i.e., $-OH$, $-O$ and $-F$, with hydroxyl groups providing the strongest interaction (0.40-0.65 eV). For MXenes with $-O$ and $-F$ terminations, the resulting in-plane interaction with H_2O (0.10-0.30 eV) is comparable to the one observed for graphene and MoS_2 (0.12 eV and 0.15 eV, respectively).

Water chemisorption has been observed on surfaces with a single termination vacancy (V_T), on edges, and especially on almost all defect clusters ($pV_{Ti}+qV_T$, with $p=1,2$ and $q=1,2,3$). Whenever an unsaturated titanium atom appeared on the surface, the oxygen atom of water approached the defect and chemisorbed onto it. The energy gains are higher for the chemisorption on vacancy clusters (1.00-1.80 eV) compared to edges (0.75-0.85 eV) and termination vacancies (0.60-1.20 eV).

Chapter 3

3. Synergistic effect of MXene-MoS composite coating

MXenes, being a novel family of two-dimensional (2D) materials, have gained notable attention in tribology due to the formation of beneficial tribofilms, as discussed in the previous chapters. However, studies using MXenes as solid lubricants have mainly focused on multi-layer $\text{Ti}_3\text{C}_2\text{T}_x$ coatings,⁷⁸ while little is known about the tribological performance of MXene composites. Therefore, in this chapter we present a study about the tribological behavior of MXene-MoS₂ composites employed as solid lubricants under reciprocating sliding conditions. The results presented here are part of a manuscript which has been published in collaboration with the University of Chile and University of Vienna.⁶⁴

3.1 Introduction

In the last two decades, 2D materials showcased their outstanding mechanical, electrical, and thermal properties compared to their 3D precursor materials.^{192,193} Layered 2D materials can form easy-to-shear tribolayers, which separate both rubbing surfaces, thus reducing friction and wear.^{31,194,195} In this regard, graphene and transition metal dichalcogenides (TMDs) are the most studied 2D materials until now.^{196,197} However, since their discovery in 2011, the more recently established material class of MXenes has rapidly gained notable attention owing to their tunable structure and chemistry, offering tremendous potential for tribological applications.^{35,66}

Even though there is a vast variety of possible MXenes, multi-layer $\text{Ti}_3\text{C}_2\text{T}_x$ is by far the most studied in tribology.^{79,82} MXenes can be either used as lubricant additives,¹⁹⁸ solid lubricants,^{82,89} or fillers in composites.^{199,200} MXenes and, particularly multi-layer $\text{Ti}_3\text{C}_2\text{T}_x$, have shown an excellent wear resistance²⁰¹ and friction reduction (coefficient of friction $\approx 0.1 - 0.3$ under dry sliding conditions and low relative humidities),⁸⁶ in particular when used as solid lubricants deposited on various substrates by spray-coating, drop casting or electro-spraying.^{83,86,201} The observed experimental tendencies were traced back to the formation of a stable tribofilm.²⁰² Generally, it has been found that homogenous, high-quality coatings are mandatory for an excellent tribological performance. Additionally, irrespective of the deposition technique, the establishment of a proper substrate-coating interface is crucial for achieving superior tribological performance under solid lubrication.⁸² In this regard, we have already demonstrated that MXenes' surface terminations significantly influence their interlayer and substrate adhesion, thus greatly affecting the resulting tribological performance (see Chapter 2 of this thesis).

Based on the presented panorama, it becomes evident that 2D materials and, particularly, MXenes can notably improve the performance of tribological components. Little knowledge

is available about MXenes' true tribological potential, since a systematic study evaluating the effect of different tribological loading conditions is still missing. Moreover, only few studies have combined $\text{Ti}_3\text{C}_2\text{T}_x$ with other 2D materials (e.g., graphene or MoS_2) to induce synergistic tribological effects.^{63,84,203}

In this context, we present here the tribological performance of $\text{Ti}_3\text{C}_2\text{T}_x$ and $\text{Ti}_3\text{C}_2\text{T}_x/\text{MoS}_2$ hybrid coatings used as solid lubricants under reciprocating sliding conditions. In chapter 3.3.1 we present DFT predictions concerning the resulting interlayer adhesion and coating-substrate adhesion, which helped to design the hybrid coatings. Multi-layer $\text{Ti}_3\text{C}_2\text{T}_x$, MoS_2 and two hybrid coatings using $\text{Ti}_3\text{C}_2\text{T}_x$ and MoS_2 (random mixture and sandwich-like) were spray-coated onto steel substrates, leading to a coating thickness of about 800 nm. In chapter 3.3.2 we discuss the solid lubrication performance of our composites, explored by carrying out dry sliding tests using a steel ball at room temperature. The morphology of the initial coatings and of the formed tribofilms have been widely characterized, employing both scanning and transmission electron microscopy (SEM, TEM) as well as X-ray photoelectron spectroscopy (XPS), as discussed in chapter 3.3.3. Our results demonstrate that both hybrid coatings notably reduced friction and wear, which was traced back to synergic effects between $\text{Ti}_3\text{C}_2\text{T}_x$ and MoS_2 thus enhancing the formation of a stable tribofilm.

3.2 Methods

Materials. Ball bearing steel (AISI 52100) was used for both tribological counter-bodies of the reciprocating ball-on-disc test, namely, disc $\varnothing 24 \times 7.9$ mm ($R_a = 35$ nm) and ball $\varnothing 10$ mm ($R_a = 20$ nm - grade G10). The solid lubricant coatings were applied on the plane surface of the discs by spray-coating. Uncoated discs and balls were tested as reference material.






As coating materials, multi-layer $\text{Ti}_3\text{C}_2\text{T}_x$ and molybdenum disulphide (MoS_2) nano-sheets were utilized. Multi-layer $\text{Ti}_3\text{C}_2\text{T}_x$ will be just named "MXene" throughout the entire chapter. Regarding MXenes' synthesis, commercial Ti_3AlC_2 MAX-powder (FORSMAN SCIENTIFIC Co. Ltd., Beijing, China) was immersed in a 40 % hydrofluoric acid (HF) solution. Under continuous stirring at room temperature for two hours, the reaction product was neutralized by several washing cycles with deionized water. Using centrifugation, the powder was separated prior to filtering under vacuum conditions and freeze-drying. The described synthesis resulted in multi-layer MXenes with a negligible amount of aluminum having x-y dimensions of about 2-3 μm . In z-direction, the as-fabricated multi-layers consisted of about 100-120 layers, thus being around 100 nm thick (0.9 nm average layer distance). More details about the synthesis process and the physicochemical characteristics of the as-synthesized MXenes can be found in previously published research work.^{85,198,201} Commercial MoS_2 powder was purchased from Graphene supermarket (United States). In this regard, the MoS_2 powder demonstrated a multi-layer structure with an interlamellar spacing of about 0.58 nm as measured by high-resolution transmission electron microscopy.

Coating deposition. A total of four different coating systems were fabricated: a MXene coating, a MoS₂ coating, and two hybrid coatings consisting of a mixture of MXenes and MoS₂ (**Table 3.1**). Irrespective of their composition, the 2D materials were mixed with ethanol using a concentration of 2 mg/mL.

Composite I was prepared by dispersing MXenes and MoS₂ in ethanol in the same weight fraction. The dispersions were homogenized for 5 minutes at 10,000 rpm using a shear-mixer. The dispersion and distribution of the nano-sheets were improved using tip sonication for 1 hour (sonication time 5s on, 5s off, 50 W power), followed by 2 hours of bath sonication. Afterwards, the solution was spray-coated on the steel disc samples: The samples were arranged on a heating plate maintained at 75°C during spray-coating to speed up the solvent evaporation. A nozzle-substrate distance of 100 mm was kept fixed for all samples. A pressure of 20 psi (1.38 bar) in the compressor was used during spray-coating.

Composite II was produced by creating a sandwich-like structure with MXene being the bottom and MoS₂ being the top layer as illustrated in **Table 3.1**. The sprayed volume was adjusted to obtain a coating thickness of 800 nm for all coatings (Composite I had two layers with an individual thickness of about 400 nm) except for MXene, which had a coating thickness of about 300 nm. After initial tribological pre-tests, it was observed that an increased MXene thickness brought drawbacks when compared to thinner coatings. Similar results had also been previously published.^{204,205} The resulting coating thicknesses were measured using white light interferometry (WLI, MFT-500, Rtec Instruments).

Table 3.1: Summary of deposited coatings including coating design, thickness, deposited volume, and schematic representation of all samples considered.

Name	Material / Coating	Volume sprayed (mL)	Coating thickness (nm)	Schematic
REF	Ball bearing steel AISI 52100	/	/	
MXene	MXene multi-layer Ti ₃ C ₂ T _x	2	275 ± 25	
MoS ₂	Molybdenum disulphide	4	775 ± 35	
Composite I	“Mix”: MXene (50%) + MoS ₂ (50%)	6	825 ± 55	
Composite II	“Bilayer”: MXene bottom + MoS ₂ top	8 (4+4)	850 ± 50	

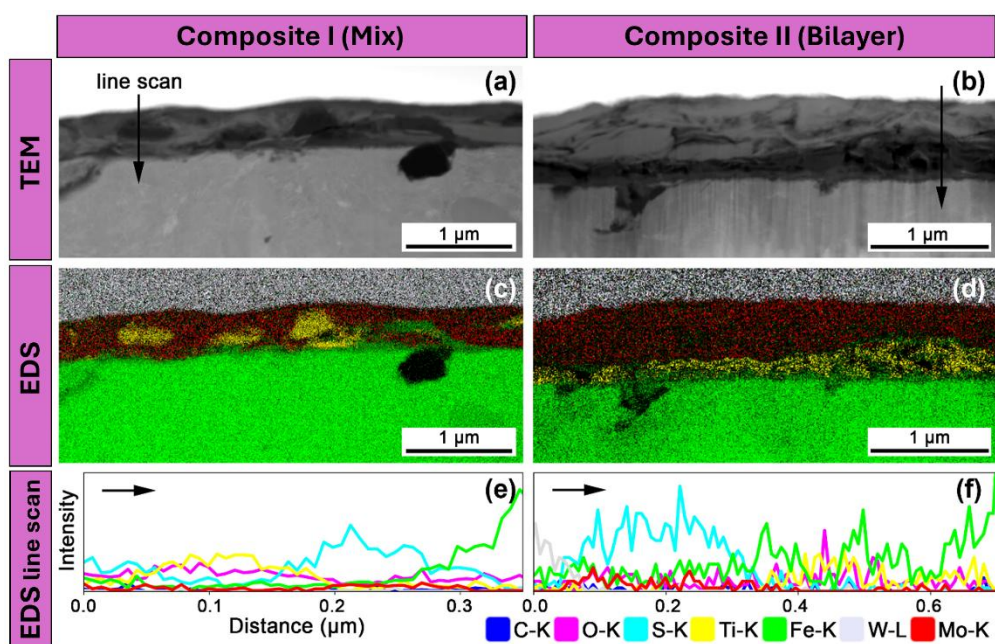


Figure 3.1: Cross-sectional morphology of the as-sprayed (a) composite I and (b) composite II coatings as analyzed by transmission electron microscopy. (c) and (d) are elemental maps of the same areas with (e and f) the corresponding energy dispersive X-ray spectroscopy line scans along the lines indicated in (a) and (b) by black arrows.

The structure and morphology of the as-deposited hybrid coatings have been investigated using transmission electron microscopy (TEM, FEI TECNAI F20) with energy-dispersive X-ray spectroscopy (EDS), as shown in **Figure 3.1**. Within the coatings, contrast differences become noticeable in **Figure 3.1a-b**, for which MXene-rich areas tend to be darker, while zones enriched in MoS₂ appear brighter. The corresponding elemental mappings (**Figure 3.1c-d**) and EDS line-scans (**Figure 3.1e-f**) verify the success of the adopted approach. For Composite I, MXene (Ti signal in yellow) and MoS₂ (Mo signal in red) are randomly intermixed, while larger MXene flakes are surrounded by smaller MoS₂ particles. In the case of Composite II, MXene can be identified as the bottom-layer, while MoS₂ is the top-layer. This is also well reflected by the EDS line-scans, showing alternating S (from MoS₂) and Ti (from MXene) signals for Composite I and a clear separation between S and Ti signals for Composite II. The fact that the bottom MXene layer in Composite II is not perfectly continuous can be traced back to spray-coating, in which the nanomaterials are stochastically deposited on the substrate.

Tribological testing. The tribological experiments were carried out under reciprocating sliding using an SRV®5 tribometer from Optimol Instruments. The disc samples were fixed at the bottom part of the tribometer, whereas the balls are mounted on the upper oscillating sample holder. An electrical linear motor controls the frequency and stroke of the ball, while the normal load was applied to the disc through a load cell. Two piezo electric force sensors mounted on the disc sample holder measured the vertical (load) and lateral (frictional) forces.

The samples were tested at a Hertzian contact pressure of 0.8 GPa, an oscillating frequency of 1 Hz, a stroke length of 2.5 mm, and a testing time of 15 minutes. The tribological conditions were chosen upon previous research conducted by the authors, in which MXene solid lubricant coatings showed a beneficial friction evaluation up to contact pressures of 0.5 GPa.²⁰⁵ A higher load has been selected in this study (contact pressure of 0.8 GPa) to verify MXenes' operational limits and evaluate the potential of hybrid coatings for severe operations. The tests were performed at room temperature (20°C). Each testing condition was repeated three times for statistical reasons to calculate mean values and standard deviations.

Tribofilm characterization. The wear tracks were analyzed post-mortem by scanning electron microscopy (SEM, multi beam system JIB-4700F – JEOL) with energy-dispersive X-ray spectroscopy (EDS), focused ion beam microscopy (FIB), X-ray photoelectron spectroscopy (XPS) and transmission electron microscopy (TEM, FEI TECNAI F20). XPS maps were acquired using a Thermo Fisher Scientific Thetaprobe with a monochromatic Al K_α X-ray source (1486.6 eV). The pass energy of 200 eV and spectrum energy step size of approximately 0.7 eV were used. The X-ray spot on the sample surface had a diameter of 50 μm and the map grid step size was likewise set to 50 μm. Prior to analysis, the whole map area was briefly sputter-cleaned with 3 keV Ar ions. Peak fitting was carried out with the Thermo Fisher Scientific Advantage Data System software using Gaussian/Lorentzian functions for peak fitting. The C_{1s} peak of adventitious carbon located at 284.6 eV was utilized as a binding energy reference.

For TEM investigation, the lamellae were prepared by FIB. The TEM lamellae had a size of about 30 x 10 μm², with a thickness of <100 nm. TEM-EDS mappings and line-scans provided information on the chemical composition. High Angle Annular Dark Field (HAADF) images showed elemental Z-contrast, while TEM imaging revealed the structure of the formed tribofilms. Additionally, Selected Area Electron Diffraction (SAED) patterns were used for phase analysis. Additional high-resolution TEM (HR-TEM) imaging was performed for phase analysis using Fourier Transformation (FT) and the measurements of lattice spacings in the HR-TEM images.

Numerical simulations. Spin-polarized DFT calculations were carried out as implemented in the version 7.2 of the Quantum ESPRESSO package.^{139–141} The Perdew-Burke-Ernzerhof (PBE) parametrization within the general gradient approximation (GGA) approach was adopted for the description of the exchange and correlation functional.¹⁰³ A dispersion term (PBE-D2_{NG}) was incorporated for the inclusion of van der Waals interactions. The D2_{NG} scheme is a modification of the Grimme-D2 parametrization, in which the C₆ and R₀ coefficients of the metal atoms (Ti, Mo, and Fe) are replaced with those of the preceding noble gas (i.e., Ar). We have already revealed the ability of such method to accurately improve the description of the interlayer interaction between MXenes (see chapter 2.2.1). The electronic wave-functions were expanded on a plane-waves basis truncated with a cut-off of 50 Ry, while a cut-off of 400 Ry was employed for the charge density, accordingly to our previous studies on MXenes.^{91,92}

Default thresholds on the total energy (10^{-4} Ry) and forces (10^{-3} Ry/Bohr) were used for structural optimizations, while adopting a Gaussian smearing of 0.02 Ry for the electronic state occupation around the Fermi level.

To avoid spurious vertical interactions between replicated images, 15 Å of vacuum were included along the axis perpendicular to the surfaces. $\text{Ti}_2\text{CT}_x\text{@MoS}_2$ and $\text{Ti}_2\text{CT}_x\text{@Fe}_2\text{O}_3$ bilayers were modelled using hexagonal cells of size 9.32 Å and 9.97 Å, respectively. The mismatch between the equilibrium lattice parameter of the hetero-interfaces and that of their constituents never exceeded 5%. The Brillouin zone of the hexagonal cells was sampled with a 6 x 6 x 1 Monkhorst–Pack grid for $\text{Ti}_2\text{CT}_x\text{@MoS}_2$, and a 3 x 3 x 1 grid for $\text{Ti}_2\text{CT}_x\text{@Fe}_2\text{O}_3$, respectively, ensuring the convergence of the total energy. The hematite surface (Fe_2O_3) was modelled with the Fe-terminated (001) plane, being one of the dominating planes in most of natural conditions.¹⁵² The PBE functional with the inclusion of the Hubbard correction (PBE-D2_{NG}+U) was used for both the Fe_2O_3 surface and the $\text{Ti}_2\text{CT}_x\text{@Fe}_2\text{O}_3$ interface to compensate the onsite repulsion between d electrons of iron. In fact, Fe_2O_3 is a strongly correlated system with the wave function showing an antiferromagnetic character. The value of the U parameter was set to 4.2 eV, as described and explained in our previous work.⁹¹

The work of separation, which is the opposite of the adhesion energy, was calculated as a difference between the total energy of the single surfaces ($E_1 + E_2$) and the total energy of the corresponding interface (E_{12}), divided by the in-plane area of the cell:

$$W_{\text{SEP}} = \frac{(E_1 + E_2) - E_{12}}{A_{\text{cell}}} \quad (3.1)$$

From equation 3.1, the higher the W_{SEP} values, the greater the interlayer and layer-substrate interactions. The work of separation changes as a function of the relative lateral position of the interface constituents. Therefore, we evaluated the interlayer and layer-substrate adhesion sampling different inequivalent lateral positions. The W_{SEP} values presented in this manuscript refer to the thermodynamically most favorable lateral position between adjacent layers.

3.3 Results and Discussion

3.3.1 DFT predicted adhesion behavior

The adhesion of pure MoS_2 and MXene layers onto steel substrates and the interlayer adhesion between MoS_2 and MXene layers have been numerically evaluated using DFT calculations to support coating design and improve the interpretation of the underlying mechanisms responsible for the experimental results. Previous numerical results proved that the MXene monolayer thickness plays a marginal role when evaluating adhesion and molecular adsorption properties.⁹¹ Indeed, the work of separation of Ti_2CT_x and $\text{Ti}_4\text{C}_3\text{T}_x$ MXene bilayers has been shown to be mainly influenced by their surface terminations rather than the monolayer thickness or overall stoichiometry. Furthermore, almost identical adsorption

energies were found for the H₂O molecule on defect-free Ti₂C and Ti₄C₃ layers, confirming that only the atoms closest to the MXene surface (i.e., terminations) are relevant to describe the energetics of adsorption/adhesion processes.⁹² Therefore, Ti₂CT_x layers were simulated instead of Ti₃C₂T_x to reduce computational costs.

It has been reported that when Ti-based MXene layers are synthesized through hydrofluoric acid (HF) etching, a random mixture of -O, -F and -OH groups passivates their surfaces.^{128,129} However, the exact distribution and stoichiometric ratios between such passivating groups is not easy-to-grasp, since many synthesis and storage parameters can influence the final composition. In this delicate context, we decided to adopt a model for mixed-terminated Ti₂CT_x that shows one third of each termination, randomly distributed on the surface. Such model, whose stoichiometric formula is Ti₂C(F_{1/3}O_{1/3}OH_{1/3})₂, was able to reproduce the experimental adhesion energy values obtained via atomic force microscopy.¹⁷⁰ For the sake of simplicity we will refer to Ti₂C(F_{1/3}O_{1/3}OH_{1/3})₂ as Ti₂CT_x.

It is well accepted that the tribological performance of 2D materials is greatly influenced by their interlayer adhesion (between adjacent layers) and the resulting coating-substrate adhesion. To shed light on both aspects from a theoretical point of view, we calculated the work of separation W_{SEP} between the 2D materials and with the ferrous substrate, i.e., iron (011) and iron oxide (001), which can give useful indications regarding the resulting coating design.

Concerning the W_{SEP} of the coating-substrate interface, pure MoS₂ adheres better to pure iron (1.30 J/m²) than Ti₂CT_x (0.40 J/m²) as shown in **Figure 3.2a**. When considering iron oxide Fe₂O₃, the opposite trend can be recognized since Ti₂CT_x shows an increased W_{SEP} (0.87 J/m²) compared to MoS₂ (0.35 J/m²). This can be related to both charge- and hydrogen-transfer from the MXene layer to the hematite surface. The formation of chemical bonds between MXene' terminations and the exposed Fe atoms of Fe₂O₃, as well as the H-transfer from the hydroxyl groups of Ti₂CT_x to the oxygen atoms of the hematite can be seen in the inset of **Figure 3.2a**. Since the used substrate is covered by a thin native oxide layer, these numerical insights motivate the usage of a MXene bottom layer in a sandwich-layer structure with MoS₂ being the top-most layer.

With respect to the interlayer adhesion (**Figure 3.2b**), it is important to point out that a lower W_{SEP} between the 2D layers indicates an improved lubricity. The interlayer adhesion between pure MoS₂ layers is 0.27 J/m², which explains the generally excellent lubricating capability of this material. Interestingly, the interlayer adhesion between MoS₂ and Ti₂CT_x with 0.25 J/m² has been estimated to be very similar, which indicates a similarly excellent lubricity for these hetero-interfaces. In contrast, the inherent adhesion between adjacent Ti₂CT_x layers is significantly higher (0.52 J/m²). Since the resistance to sliding typically decreases with the interfacial adhesion,¹¹² coatings composed of a mixture of MoS₂ and MXenes are highly promising to improve the frictional performance. Therefore, the theoretical calculations are

indicative that MXene/MoS₂ composites can offer low interlayer friction and high adhesion to ferrous substrates, which may lead to an excellent frictional performance, thus outperforming pure MXene and MoS₂ coatings.

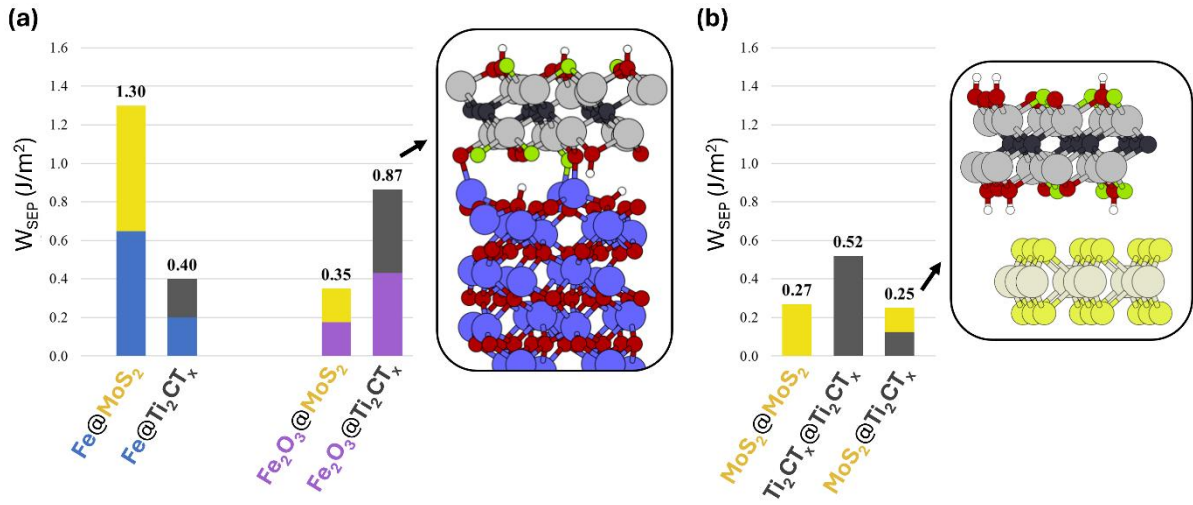


Figure 3.2: (a) Adhesion of MoS₂ and Ti₂CT_x layers onto pure iron (left-hand side) and hematite surfaces (right-hand side). (b) Work of separation (W_{SEP}) for MoS₂@MoS₂, MoS₂@Ti₂CT_x and Ti₂CT_x@Ti₂CT_x interfaces. Optimized configuration for the Ti₂CT_x layer interacting with Fe₂O₃, as well as for the MoS₂@Ti₂CT_x bilayer are reported within the insets.

3.3.2 Solid lubrication performance

The frictional performance of all samples was evaluated using reciprocating sliding experiments at room temperature (**Figure 3.3a**). For the bearing steel reference (indicated as “REF”), the coefficient of friction (COF) started at around 0.4 and quickly increased to 0.7 until levelling off at about 0.9. This can be considered a typical frictional behavior for steel-on-steel contact. In contrast, the coated samples featured entirely different behaviors.

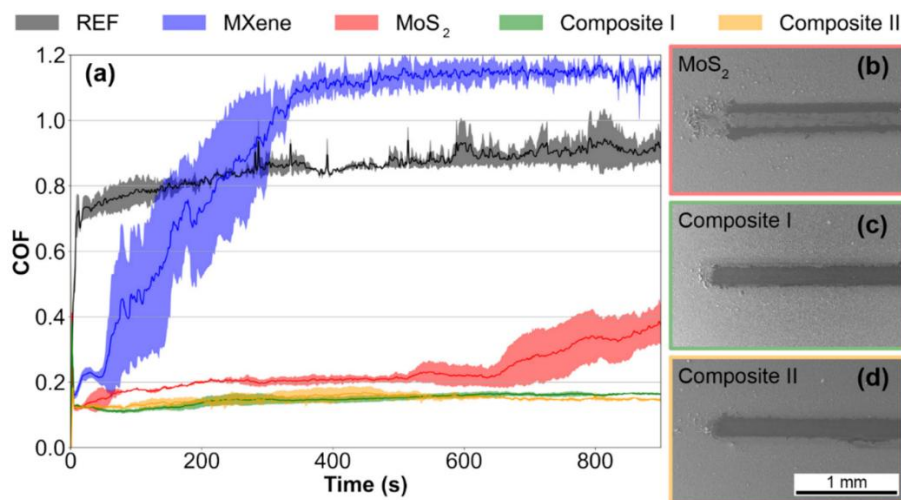


Figure 3.3: (a) Evolution of the COF of all samples. SEM micrographs of the wear tracks for (b) MoS₂, (c) Composite I and (d) Composite II. Mean values and the respective standard deviations of the three test-replica are shown as solid line and shaded area, respectively.

The pure MXene coating (blue line in **Figure 3.3a**) did not show a beneficial effect for long under the chosen severe testing conditions since it only decreased friction for the first 200 s, after which it reached a high COF of 1.1. Under an elevated contact pressure of 0.8 GPa, the MXene coating is simply removed from the tribological contact zone, thus being deposited at the turning points of the wear track (see Figure S3 of ref.⁶⁴).

In contrast, an excellent friction reduction was observed for the MoS₂ coating in the first 600 s, showing a COF of about 0.2 (red line in **Figure 3.3a**), which aligns well with their calculated low interlayer adhesion. However, afterwards, the COF started to increase till the end of the experiment, thus reaching values of 0.4 and losing its beneficial lubrication effect.

The best frictional performance was observed for the hybrid coatings, which did not lose their lubrication effect during the entire test duration. Both hybrid coatings (green line for composite I and yellow line for composite II in **Figure 3.3a**) demonstrated a very stable and low COF until the end of the experiment, corresponding to an almost six-fold COF reduction. Interestingly no significant frictional differences were detectable between both hybrid coatings.

For what concerns the wear behavior, the overall coarse-scale appearance of the wear tracks was similar for both hybrids (**Figure 3.3c-d**). In contrast, non-uniform, patchy films were observed in the wear tracks of the MXene and MoS₂ coatings. Additionally, the wear track of the pure MXene and MoS₂ coatings were wider (width of about 600 and 300 μm , respectively) than those of the composites ($\sim 200\ \mu\text{m}$), which is also in accordance with the high COF of MXenes and the partial failure of MoS₂.

3.3.3 Experimental characterization of hybrid interface

Wear track analysis by XPS

To better understand the underlying mechanisms that govern the excellent frictional performance of the composites, the wear tracks were analyzed by XPS. The elemental maps are reported in **Figure 3.4**, which shed light on the chemical changes in the wear tracks induced by the tribological load.

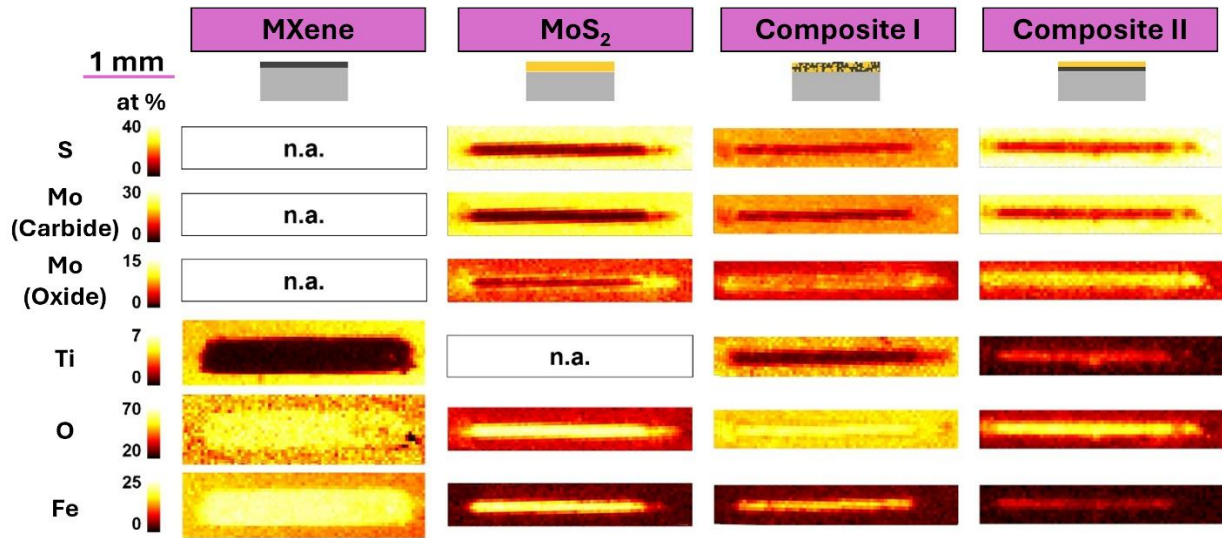


Figure 3.4: XPS maps of the wear track for MXene, MoS₂, Composite I, and Composite II. The abbreviation *n.a.* stands for *not applicable*. Please note that brighter colors imply higher element concentrations, while different scales were adopted for every distinct element to improve data visibility and readability.

In the case of the pure MXene coating, no Ti signal is detected in the wear track, while strong signals of Fe and O are observed (**Figure 3.4**). This implies the full removal of the initial MXene coating and the tribo-induced oxidation of the underlying substrate. This observation goes hand in hand with the measured evolution of the COF for this coating, which did not show any beneficial performance after a few minutes of testing. Concerning the wear track of the pure MoS₂ coating, some signals of S and Mo (carbide, attributable to as-deposited MoS₂) are detected in the outer perimeter of the wear track, while a more pronounced Mo signal (oxide) became evident in the center of the wear track. Additionally, strong Fe and O contributions are visible in the center of the wear track, which is again attributed to the partial removal of the MoS₂ coating, thus exposing the underlying substrate oxidized during tribological testing. This observation aligns well with the observed increase of the COF after a sliding time towards the end of the test (**Figure 3.3a**).

When comparing the elemental maps of the pure coatings with both hybrid coatings, notable differences can be observed. Regarding composite I (mix of MXenes and MoS₂), contributions of S, Mo (carbide) and Ti are observed in the wear track, which points toward the presence of a tribofilm containing MoS₂ and MXenes. These results corroborate the excellent frictional performance of Composite I (**Figure 3.3a**), showing the presence of MXenes and MoS₂ on the surface enduring the whole test. Moreover, signals of Mo (oxide), O, and Fe indicated the contribution of oxidation in the wear track and the formation of a tribofilm. The excellent tribological performance of composite I can be attributed to the lower W_{SEP} between MXene and MoS₂ layers as well as MoS₂ interfaces compared to pure MXene interfaces (**Figure 3.2a**). Since a lower W_{SEP} implies more lubricity, the mixture of MXene and

MoS₂ helps to reduce friction compared to the pure coatings. Additionally, the high adhesion of MoS₂ to iron and MXenes to iron oxide (**Figure 3.2b**) ensures that the lubricious film is not easily removed, thus extending the wear life.

Regarding composite II (bilayer coating having MoS₂ as top layer), the wear track still contains some S and Mo (carbide), which originate from the as-deposited MoS₂ top-layer. Besides that, a clear signal from Mo (oxide) can be seen inside the wear track, which points towards the oxidation of the outermost layers. Interestingly, the Ti signal is even stronger compared to the surrounding zones, which is due to the partial removal of the top MoS₂ layer and the exposure of the bottom MXene layer. The Fe signal is weaker for composite II compared to the pure coatings, still indicating the presence of a thin coating after the tribological tests. These findings based on the XPS analysis imply that the top MoS₂ is only partially removed and oxidized. In this regard, sufficient lubricious MoS₂ and MXene are still available in the wear track, which induces a low COF as presented in **Figure 3.3a**. The excellent tribological performance of composite II can be explained again considering the calculated W_{SEP} in **Figure 3.2b**. Due to the high interlayer adhesion between MXenes and the ferrous substrate, we assume that MXenes act as an intermediate anchoring layer between the substrate and MoS₂. This can help to avoid the complete exfoliation and removal of MoS₂ in composite II. Therefore, we anticipate that the bottom MXene layer contributes towards the durability and longevity of the top MoS₂ layer by acting as an adhesion layer, thus improving additional coating-substrate interface adhesion.

Comparing the elemental maps in the wear tracks of both composites, higher concentrations of S, Mo, and Ti were encountered in composite II, whereas a stronger Fe signal was detected in composite I. This points towards a thicker and more homogenous tribofilm formed for composite II, which might be due to the higher adhesion between MXene layers compared to MoS₂-MoS₂ or MoS₂-Ti₂CT_x, as well as their high adhesion to the ferrous oxides. Therefore, the bottom MXene layer in composite II is more effective in increasing the adhesion of the coating to the substrate than the randomly distributed MXenes in composite I.

To shed light on the distribution of the elements across the tribofilms, we also measured the elemental depth profiles in the middle of the wear tracks for all coated samples by XPS (**Figure 3.5**). Related to the S distribution (**Figure 3.5a**), it becomes evident that higher concentrations can be detected in surface regions. With increasing depth, the S signal decreases in an exponential way until it almost disappears at depths of about 200-300 nm. For the MoS₂ coatings, the S concentration is significantly lower compared to both hybrid coatings (roughly three-fold reduction). This result proves that the MoS₂ top layer of composite II was still mainly intact after tribological testing, which agrees with the presented XPS surface mapping. Concerning the Mo distribution, the trend seen for the detected profiles of S stays unchanged (**Figure 3.5b**). The results of the S and Mo profiles are in accordance with the COF trend, being that MoS₂ samples presented higher friction than both hybrid

coatings (**Figure 3.3a**). In fact, the higher S and Mo concentrations in the composites compared to MoS₂ indicate that the hybrid coatings were more prone to induce long-term stability to the tribofilm. MoS₂ samples lost their lubricious properties at the end of the tribological tests, whereas the composites performed low and stable friction for the entire test duration (**Figure 3.3a**).

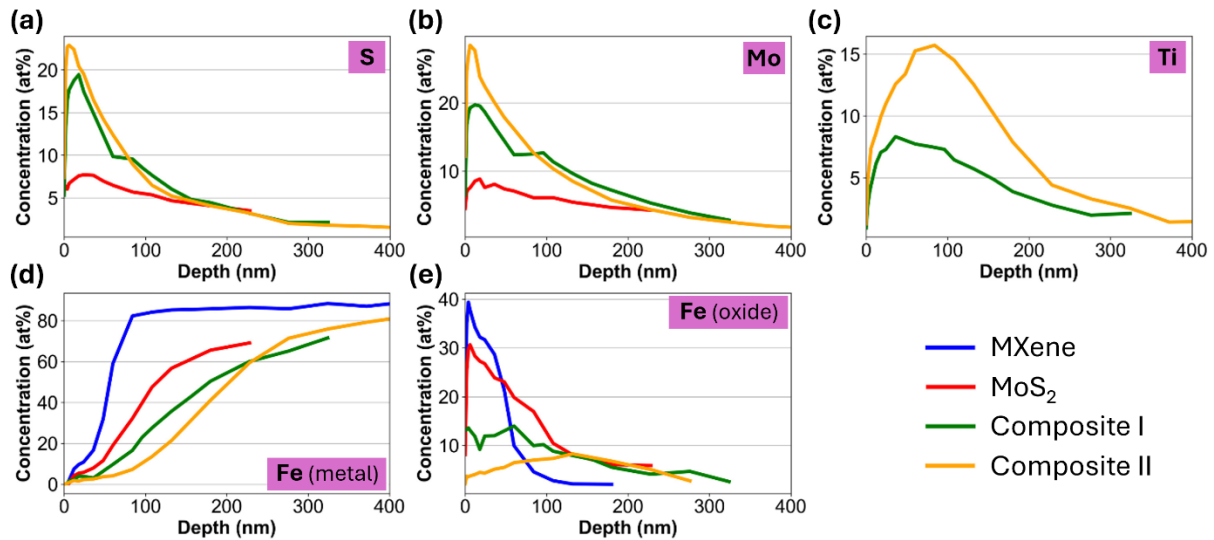


Figure 3.5: XPS elemental depth profile taken in the middle of the wear track for MXene, MoS₂, Composite I, and Composite II: (a) S, (b) Mo, (c) Ti, (d) Fe (metal) and (e) Fe (oxide).

Titanium is only detected for the hybrid samples while no traces are founded for the pure MXene coatings (no blue line in **Figure 3.5c**). This confirmed that the entire MXene layer was removed from the tribological contact zone without the possibility to form any beneficial tribolayer. This goes hand in hand with the discussed temporal evolution of the COF for the pure MXene coating, which shows an instantaneous increase reaching COF values above 1.1 (**Figure 3.3a**). For both hybrid coatings, the Ti signal is increased in surface-near regions, as observed for Mo and S, before decreasing at greater depths. In the case of composite II, the maximum Ti concentration is shifted to a region further away from the surface (i.e., maximum is at a depth of roughly 100 nm) compared to composite I, which aligns well with the as-deposited sandwich-like structure.

We divided the Fe signal into metallic and oxidic contributions to distinguish between substrate contributions (metallic signal) and tribo-oxidation (oxide signal) as well as to better estimate the tribofilm thickness after tribo-testing. In case of pure MXene coatings, the concentration of metallic Fe quickly increased with increasing depth, confirming the exposure of the metallic substrate and the removal of the as-deposited MXenes (**Figure 3.5d-e**). For MoS₂ and both hybrid coatings, the metallic Fe signal monotonously increased with increasing depth reaching concentrations above 70 % for depths of about 200, 300, and 400 nm. This outcome corroborates well with the COF trend and element maps, showing again a superior tribological potential of the composites. Finally, the oxidic Fe signal was

notably increased in superficial regions for the pure MXene and MoS₂ coatings, whereas significantly reduced contributions for Fe oxide were observed for both composite coatings. On the one hand, this clearly proves the ability of the hybrid coatings to form a beneficial tribofilm, thus protecting the substrate and preventing its oxidation and, on the other hand, the inefficiency of the pure coatings to form protecting tribofilms.

Wear track analysis by TEM

To further characterize the structure of the tribofilms, several TEM specimens were prepared by FIB from the center and turning points of the wear tracks of composite I and composite II. Additional TEM specimens were prepared by imaging the transition zone between initial coating and wear track (**Figure 3.6**).

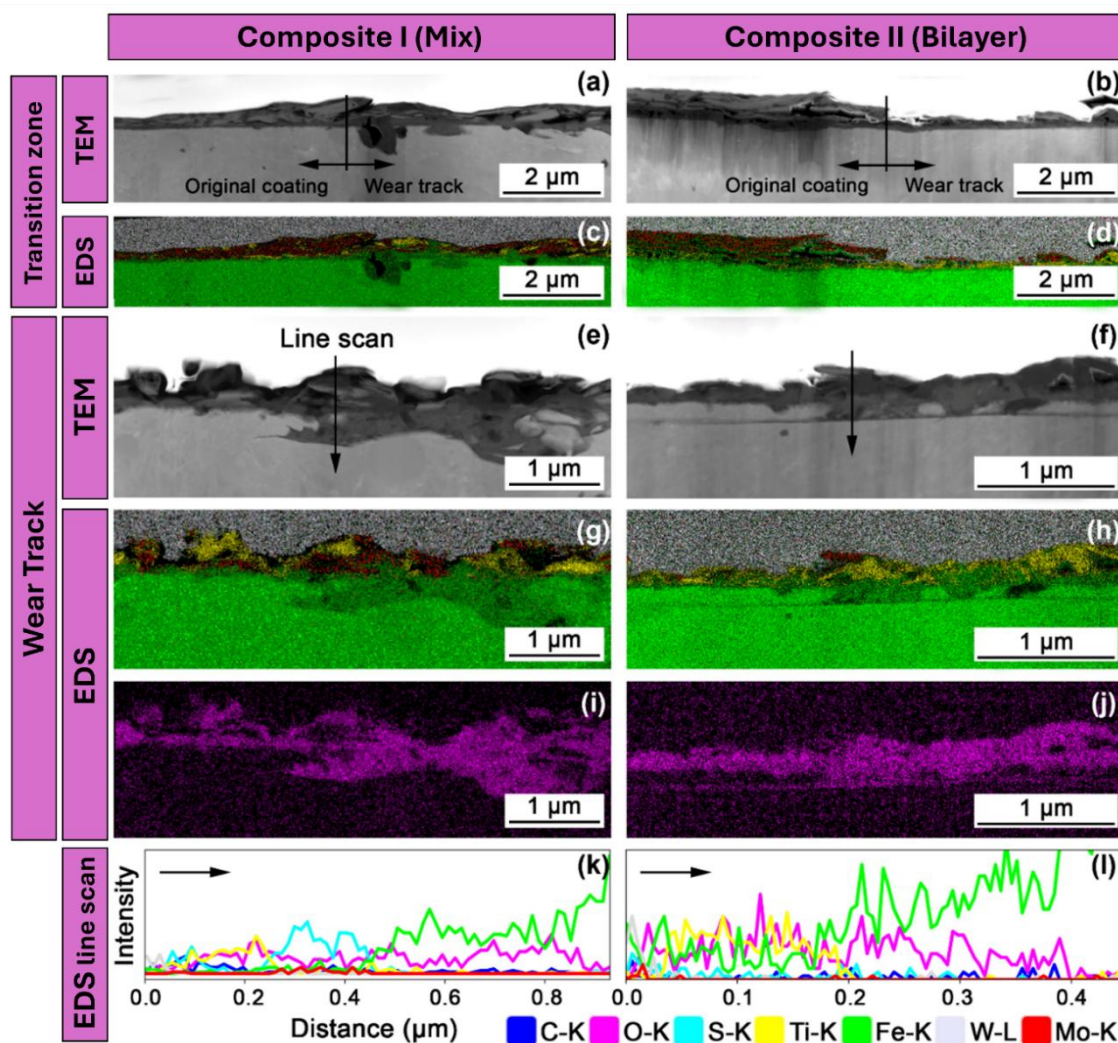


Figure 3.6: TEM analysis of the transition zone between original coating (left side of the images) and the wear track (images' right side) for (a) Composite I and (b) Composite II. Panels from (a)-(d) show the transition zone and corresponding elemental mappings. Panels (e)-(l) show the wear track, elemental mapping and EDS line scans along the lines indicated with black arrows in (e) and (f).

The TEM analysis of the transition zones of both coatings demonstrates a reduction of the coating thickness as a result of tribological loading (**Figure 3.6a-d**). Nevertheless, the original coating morphology is retained, with intermixed MXene and MoS₂ for composite I and a sandwich-structure for composite II (**Figure 3.6e-h**). In some positions, however, the coating becomes very thin or, for composite II, the top MoS₂ layer is completely removed. This is in accordance with the elemental mapping and depth profiles obtained by XPS demonstrating a much higher Ti concentration close to the surface for composite II compared to composite I. For composite II, this implies that shear is mainly localized in the top MoS₂ layer, while the bottom MXene layer helps to increase the adhesion of the tribofilms to the substrate, thus contributing to the beneficial frictional performance and increased wear life. Additionally, oxygen diffusion into the substrate and the incorporation of iron and iron oxide particles into the tribofilm can be clearly observed (**Figure 3.6i-l**). These findings correlate well with the observed Fe signals in the XPS analyses.

Figure 3.7 shows in detail the TEM analysis of the wear track's center position for Composite I. HR-TEM provides information on the structure of the tribofilm, while selected area electron diffraction (SAED) and elemental mappings by TEM-EDS of specific areas allow for an analysis of the tribofilm's crystallinity and chemical composition. After tribological testing, the thickness of the tribofilm on composite I is inhomogeneous ranging from roughly 220 nm to > 820 nm (**Figure 3.7a**). Closer investigation of the tribofilm by HR-TEM clearly demonstrates a tribofilm consisting of amorphous and layered structures (**Figure 3.7b-d**). SAED confirms the presence of crystalline (well defined larger diffraction spots), nanocrystalline (smaller spots, partially forming well defined diffraction rings according to their crystal phases), and amorphous phases (diffuse diffraction rings) inside the tribofilm (**Figure 3.7e**). The amorphous phases are mainly found close to the tribological interface as these are the positions with the highest pressure and temperature leading to thermo-mechanical amorphization. Close to the substrate surface, SAED verifies nanocrystalline Fe₂O₃, while inside the tribofilm a mixture of MoS₂ and Ti₃C₂ prevails (P63/mmc space group). The chemical composition of the tribofilm is further analyzed by elemental mapping (**Figure 3.7f**). The structure of the tribofilm after tribo-testing still resembles the initial coating structure, for which Ti-rich phases are randomly intermixed with Mo- and S-rich phases. Additionally, a significant amount of oxygen can be found inside the tribofilm.

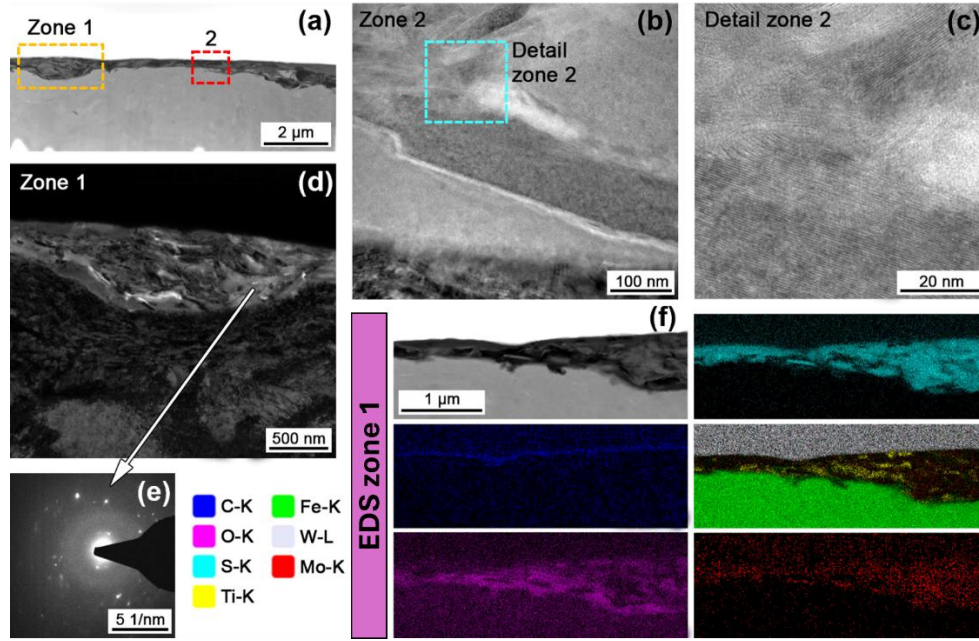


Figure 3.7: TEM analysis of the wear track on Composite I. (a)-(d) TEM images with different magnifications provide information on the structure of the tribofilm, and (e) selected area electron diffraction patterns and (f) elemental mappings demonstrate the phase and the chemical composition of the tribofilm.

Taking these points into consideration, we anticipate that the MXene/MoS₂ hybrid coating is partially amorphized or converted into nanocrystals as a result of mechanical shearing under the high acting contact pressures (globally 0.8 GPa, higher peak loads are expected). Additionally, the MXene and MoS₂ nano-sheets are partially oxidized due to tribochemical reactions. Nevertheless, there are still many intact 2D nano-sheets as well as MXene/MoS₂ interfaces in the tribofilm (**Figure 3.7c**), which can provide low shear strength (**Figure 3.2a**), resulting in the low friction observed in **Figure 3.3a**.

Finally, **Figure 3.8** shows the corresponding TEM analysis of the wear track's center position for composite II. Similar to composite I, HR-TEM clearly indicates a mixture of amorphous, crystalline, and nanocrystalline phases inside the tribofilm, where layered nano-sheets can be easily distinguished (**Figure 3.8a-c**). The presence of amorphous phases and crystalline MoS₂ and Ti₃C₂T_x is confirmed by SAED (**Figure 3.8d-f**). As verified by the elemental mapping, the structure of the tribofilm strongly resembles the initial coating with a Mo-rich top-layer and a Ti-rich layer below, thus maintaining the original sandwich-like structure (**Figure 3.8g**). Nevertheless, there are still sufficient crystalline 2D structures in the tribofilm to provide low shear and to efficiently reduce friction.

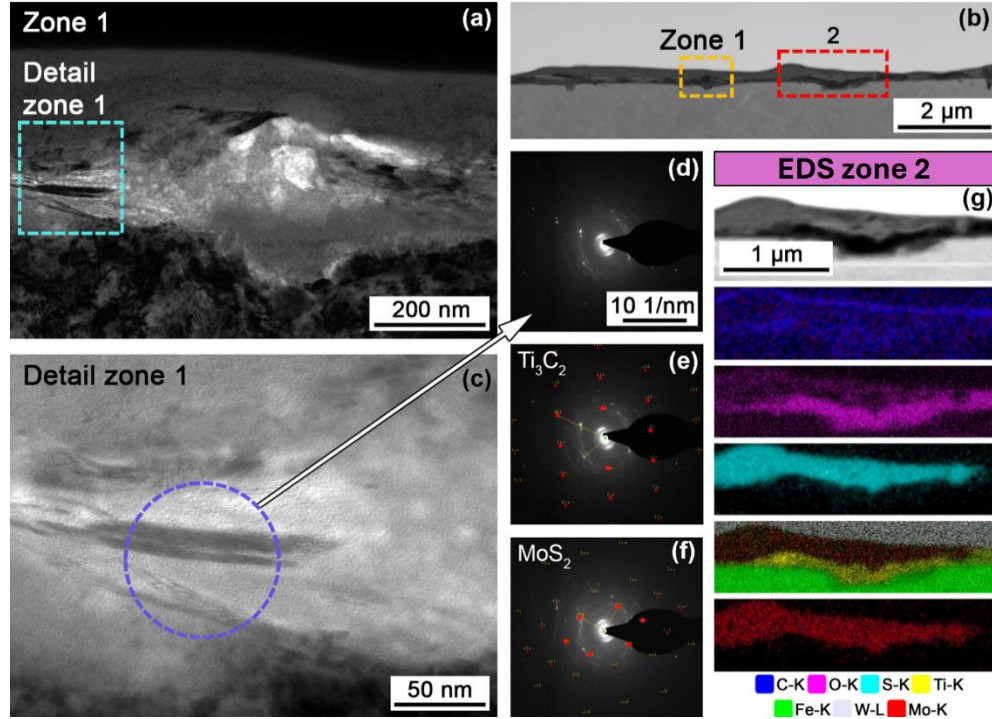


Figure 3.8: TEM analysis of the wear track on Composite II. (a)-(c) TEM images with different magnifications provide information on the structure of the tribofilm, and (d)-(f) selected area electron diffraction patterns and (g) elemental mappings demonstrate the phase and the chemical composition of the tribofilm on Composite II.

Considering the numerical calculations as well as XPS and TEM results for both composites, it becomes evident that the coatings' structure remained mainly intact after tribological testing with little intermixing of the constituents. For composite I, the low W_{SEP} for mixed MXene/MoS₂ interfaces, which is similar to MoS₂-MoS₂ interfaces, is the major factor responsible for the improved lubricious properties. Since MoS₂ tends to adhere to pure iron and MXenes demonstrated an improved adhesion to iron oxide, the formed tribofilm can stick to the substrate independent of the respective chemical state of the substrate. This helps to extend the useful lifetime of low friction tribofilms. In the case of composite II, the stronger adhesion of MXenes to iron oxide acts as an adhesion layer, while the resulting frictional performance is mainly governed by the low interlayer adhesion of adjacent MoS₂ layers.

3.4 Conclusions

In this chapter, we presented an example of how DFT simulations can support experimental results, offering predictive insights and mechanistic understanding of the tribological performance of MXene/MoS₂ hybrid coatings. Multi-layer Ti₃C₂T_x, MoS₂, and two different Ti₃C₂T_x/MoS₂ hybrid coatings (random mixture and sandwich-like) have been experimentally scrutinized under dry reciprocating sliding tests (contact pressure = 0.8 GPa). Results were corroborated via numerical simulations of the adhesion forces between the 2D layers and different ferrous substrates. The friction and wear performance as well as tribolayer formation

have been holistically analyzed with a complementary characterization approach including SEM-EDS, FIB, XPS and TEM. Based on our, the following conclusions can be drawn:

- Pure MXene coatings did not bring any tribological beneficial effect under the respective testing conditions compared to the steel reference (REF), whereas pure MoS₂ coatings presented approximately a four-fold friction reduction. Both MXene/MoS₂ hybrid coatings significantly reduced friction (roughly six-fold reduction), showing low and steady COF values of around 0.15 that were maintained for the entire duration of the test, due to the formation of a stable tribofilm.
- No significant wear protection was observed for the pure Ti₃C₂T_x coating (coating removal), whereas the pure MoS₂ considerably reduced wear, although partially losing its lubricity towards the end of the test duration. The hybrid MXene/MoS₂ coatings presented a superior wear behavior, displaying the highest wear resistance.
- Numerical calculations validated the experimental results, being that MXene/MoS₂ hybrids demonstrate an excellent frictional performance with low interlayer friction and high adhesion to ferrous substrates, outperforming the pure MXene and MoS₂ coatings.
- The coating structure of both composites remained intact even after the tribological tests, confirming the synergic effect between Ti₃C₂T_x and MoS₂. In particular, the composite with bilayer structure still preserved a MoS₂ top-layer after tribo-testing. The adhesion force between Ti₃C₂T_x and MoS₂ seemed to be the governing mechanisms to enhance the formation of a stable tribofilm.

Chapter 4

4. In Operando formation of Transition Metal Dichalcogenides (TMDs)

We have already anticipated in chapter 1.2.2.2 how transition metal dichalcogenides (TMDs) have attracted enormous scientific and industrial interest due to their outstanding tribological behavior. The paradigmatic example of TMD is MoS₂, even though selenides and tellurides have also demonstrated superior tribological properties. In this fourth chapter we describe an innovative *in operando* conversion of Se nano-powders into lubricious 2D selenides by sprinkling them onto sliding metallic surfaces coated with Mo and W thin films. Advanced material characterization confirms the formation of a thin tribofilm containing selenides, reducing the coefficient of friction down to below 0.1 in ambient air. *Ab initio* molecular dynamics simulations carried out under tribological conditions reveal the atomistic mechanisms that result in shear-induced synthesis of selenide monolayers from nano-powders. The use of Se nano-powder provides thermal stability and prevents outgassing in vacuum environments. Additionally, the high reactivity between the Se nano-powder and the transition metal coating yields highly reproducible results, making this process suitable for the replenishment of solid lubricants, avoiding the long-lasting problem of TMD-lubricity degradation caused by environmental molecules. The suggested straightforward approach demonstrates an unconventional and smart way to synthesize TMDs *in operando* and exploit their friction- and wear reducing impact. The results shown in this chapter are part of a publication on *Advanced Materials*.⁶⁵

4.1 Introduction

The *in operando* formation of a lubricating layer protecting the surfaces from wear has many advantages, such as their selective formation at locations where they are needed the most, as well as basically infinite wear life as long as the precursors for their formation are still available. In engineering applications, it is quite common to form surface-protecting tribofilms *in operando* by decomposition of precursor molecules, such as is happening with the well-known friction modifier molybdenum dithiocarbamate (MoDTC)²⁰⁶ and the anti-wear agent zinc dialkyldithiophosphate (ZDDP),²⁰⁷ which has been used as lubricant additives for many decades. A major concern of such additives is that they often rely on organometallic compounds that are noxious for the environment.

Alternatively, it has been shown in the past that it is possible to form solid lubricants based on nanocarbons *in operando* from hydrocarbon gases or liquids.^{208,209} Therefore, mechanochemical processes such as high-energy ball milling²¹⁰ can be used or the solid lubricants can be directly formed during tribological loading as a result of high contact pressure, shear, and flash heating.^{114,211–213} In this case, the metallic elements required for the

in operando formation of the solid lubricants are environmentally compatible as they can be used in metallic form or as inorganic compounds.

Transition metal dichalcogenides (TMDs) (e.g., MoS₂, WS₂ or MoSe₂) have been used by industry for many years, mainly because of their unique tribological properties. Most of them are synthetically produced, but MoS₂ exists naturally in a crystalline form, known as molybdenite mineral. Under dry sliding conditions in high vacuum or in inert gas environments they can provide some of the lowest coefficients of friction (COF). Mainly because of such excellent lubrication properties, they are the choice of lubricants for many types of space applications, such as the recently launched James Webb Space Telescope.²¹⁴

Their excellent lubricating properties stem from a layered structure, in which individual monolayers are composed of transition metal atoms (e.g., Mo and W) sandwiched between the chalcogen atoms (e.g., S and Se). Under shear conditions layers slide over one another to provide low friction while the very strong and resilient layers protect surfaces against wear. In perfect conditions (i.e., perfectly flat, rigid surfaces), or at the nanoscale, TMDs can show superlubricity with COFs below 0.01, while at the macro-scale puckering and defect formation usually leads to COFs around 0.1.^{61,215} The most used TMD-based solid lubricant is MoS₂ even though selenides and tellurides have been recently reported to exhibit superior tribological properties.²¹⁶ When operated in high vacuum or space environments, inert gases like Ar, He, or N₂, friction coefficients approaching 0.001 are reported for TMDs (especially when used in the form of 2D sheets).²¹⁷ However, the lubricity of most TMDs is strongly affected by humidity, temperature, and other environmental species such as oxygen. In general, higher humidity causes high friction and wear.^{185,218,219}

In the past, the *in operando* formation of crystalline TMD from amorphous coatings or molecules, such as H₂S and MoDTC, was demonstrated by experiments^{114,213,220–223} and simulations.^{120,224,225} However, in this chapter we describe an innovative approach that results in the formation of TMDs even with the use of the chalcogen element (Se) in the form of a nano-powder, sprinkled onto the metallic surfaces involved (Mo and W). The tribochemical reactions in the contact zone resulted in the formation of MoSe₂ and WSe₂, which guarantee very low friction and wear. Transmission electron microscopy (TEM) in combination with Raman and X-ray photoelectron spectroscopy (XPS) confirmed the solid-state formation of these films. Ab initio molecular dynamics (AIMD) simulations provided insight into the mechanisms governing their *in-operando* formation.

This approach opens the door to new technological applications due to its distinct advantages. Using a chalcogen powder, instead of sputtered coatings, prevents the degradation of lubricant properties caused by interaction with air humidity. Additionally, the tribological contact can be easily replenished by feeding nano-powders into the interface. This method can also be applied in high-temperature environments or on the nanoscale, where liquid media or sputtered coatings are unsuitable. We believe that this work represents

a significant advancement in the field of tribology and may inspire the in-situ synthesis of new compounds beyond traditional TMDs.

4.2 Methods

Materials and coating deposition. Polished AISI 52100 steel platelets ($20 \times 10 \times 1 \text{ mm}^3$) were used as substrate materials. Before the coating process, all samples were ultrasonically pre-cleaned in acetone and then isopropanol. Metallic W and Mo coatings with a thickness of around $2\text{--}3 \text{ }\mu\text{m}$ were synthesized from respective metallic targets (3-inch geometry, Plansee Composite Materials GmbH, 99.3% purity) in pure Ar atmosphere (99.999 % purity) using an in-house developed direct current magnetron sputtering system (base pressure below $2.0 \times 10^{-4} \text{ Pa}$). The rotating substrate holder (0.25 Hz) was positioned at a target-to-substrate distance of 110 mm. Following a heating sequence to a substrate temperature of $400 \text{ }^\circ\text{C}$, an Ar-ion etching step was performed to finally clean the substrates before deposition – pure Ar atmosphere at 5 Pa and an applied bias potential of 800 V. The thin films were then grown at a total Ar pressure of 0.4 Pa, a target current of 0.4 A, and floating potential. The resulting surface roughness (S_q) of the Mo and W coatings was 50 and 46.5 nm, respectively. The hardness of the coatings was 12.6 GPa (W) and 7.1 GPa (Mo) as determined by nanoindentation at 4 mN load from 40 indents.

Tribological Experiments. Tribological testing was performed on a ball-on-disk setup (Nanovea T50 Tribometer) in unidirectional sliding mode with a sliding radius of 2 mm. The counterbody was an Al_2O_3 sphere with a diameter of 6 mm (surface roughness S_q : 40 nm), to avoid substantial wear of the counterbody as well as contamination with other transition metals and catalytic effects of metallic particles. The load was set to 1 N, leading to a peak Hertzian contact pressure of 0.73 GPa, 0.88 GPa, and 0.92 GPa for the steel, Mo, and W substrates, respectively. The sliding speed was set to 1000 mm/min. The tests were run under ambient air with a temperature of $25 \text{ }^\circ\text{C}$ and a relative humidity of $\sim 45\%$. After the sample was fixed in the tribometer, 10 mg of high-purity (99.9 %) Se nano-powder with a particle size distribution between 40 to 80 nm (NANOSHELL UK Ltd.) was manually sprinkled onto the substrate surface with a spatula directly underneath the Al_2O_3 counterbody. Subsequently, the counterbody was brought into contact with the Se nano-powder so that there was a visible transfer of the loose Se nano-powder from the substrate to the counterbody. Afterwards, we started the sliding experiment. Additional reference measurements are performed without the addition of Se powder. All tests were run three times, so that the mean values and standard deviations could be plotted. Additional tests with Se nano-powder were performed to study the ability to re-establish lubricious TMD layers after their degradation. Therefore, the tribometer was stopped once the COF reached the high friction value observed at the beginning of the test, Se nano-powder was applied again to the contact zone analogously to the test before, and the test was restarted again without changing the relative position of substrate and counterbody.

Characterization of the tribofilm. The substrate surfaces and wear tracks were imaged by confocal laser scanning microscopy (CLSM, Keyence VK-X1100) and scanning electron microscopy (SEM). The average cross-sectional area of the wear tracks A as measured by CLSM was used to calculate the wear rate using the expression:

$$K \left[\frac{\text{mm}^3}{\text{N}\cdot\text{m}} \right] = \frac{A \cdot L}{F_n \cdot N \cdot L}, \quad (4.1)$$

Where L is the length of the wear track, F_n is the normal force, and N is the number of sliding cycles. The chemical state of the surfaces before and after wear was investigated by Raman spectroscopy (HR800, Jobin Yvon Horiba) with a laser wavelength of 532 nm and a yielded laser power of 13.5 mW was used. The spot size was 20 μm and the measuring time 3s. Additionally, X-ray photoelectron spectroscopy (XPS, Thermo Fisher Scientific Theta Probe) was used to determine the chemical bonding states in the top-most surface layers. The XPS device was equipped with a monochromatic Al K α X-ray source ($h\nu = 1486.6$ eV) and an Ar $^+$ ion gun. The analyzed spot size diameter was 100 μm , with pass energies of 200 eV for the survey spectra and 50 eV for the high-resolution spectra. The XPS spectra were acquired before and after 10 seconds of fine sputtering which was conducted in order to remove any possible surface contamination. The measurements were performed at a base pressure of 2×10^{-9} mbar. All the high-resolution spectra were referenced to the adventitious carbon (C 1s binding energy of 284.8 eV). Afterwards, the spectra were processed with the Thermo Fisher Scientific Advantage Data System using Gaussian-Lorentzian peak fitting. Transmission electron microscopy (TEM, FEI TECNAI F20) was used to image the structure of the formed tribofilms. Energy dispersive X-ray spectroscopy (EDS) inside the TEM was performed using an EDAX detector.

Ab initio Calculations. Spin-polarized DFT calculations were performed employing version 6.7 of the Quantum ESPRESSO package.^{139–141} The generalized gradient approximation (GGA) within the Perdew-Burke-Ernzerhof (PBE) parametrization was used to describe the electronic exchange and correlation.¹⁰³ Dispersion interactions were included using the D2 parametrization scheme of Grimme.¹⁴² The plane-wave expansion of the electronic wave functions (charge density) was truncated with a cutoff of 40 Ry (320 Ry). The ionic species were described by ultrasoft pseudopotentials, considering 14 explicit electrons for the d-ions (e.g., W and Mo), and 6 explicit electrons for chalcogens (e.g., O and Se). For the structural optimization, we adopted default criteria for energy and forces convergence (10^{-4} Ry and 10^{-3} Ry/Bohr, respectively) and used a Gaussian smearing of 0.02 Ry. We modelled the (110) surfaces of Mo by sampling the Brillouin zone with a $14 \times 18 \times 1$ Monkhorst-Pack grid,¹⁴³ while an equivalent sampling was used for larger cells. To avoid spurious interactions, all surfaces and interfaces were built with at least 15 Å of vacuum between vertical replicas.

For the AIMD simulations of sliding surfaces we used a version of the Born-Oppenheimer Molecular Dynamics modified by our group to impose tribological conditions. The outmost metallic atoms are dragged with a constant velocity of 2 Å/ps; a normal load of 10 GPa, and a

constant temperature of 600 K are applied. Newton's equations of motion are integrated using the Verlet algorithm. We tuned the time step, dt , according to the frequency of bond vibrations, with the Mo-O bond stretching having the shortest period of 33 fs (corresponding to a frequency $\nu = 1000 \text{ cm}^{-1}$).²²⁶ Therefore, we selected a dt value of 2.4 fs, so to sample more than 10 times each bond vibration. This choice allows for a fast production, while ensuring a correct integration of the equations of motion. To observe the full formation of TMD from Mo and Se particles, we performed long simulation runs (up to hundreds of ps). In this case, where Mo-O bonds were not present, the dt was increased to 9.4 fs.

4.3 Results and Discussion

4.3.1 An innovative lubrication method

We performed unidirectional ball-on-disk experiments using chemically inert Al_2O_3 counterbodies to study the *in operando* formation of solid lubricants based on TMDs, in particular MoSe_2 and WSe_2 . Without the application of Se nano-powders on the sliding surfaces, the evolution of the COF over the sliding cycles is characteristic for non-lubricated sliding of a metal substrate *versus* a ceramic counterbody (**Figure 4.1**). The COF starts at 0.4 for the bare Mo coating (**Figure 4.1a**) and at 0.3 for bare W (**Figure 4.1b**) and then quickly increases to a maximum value of 0.8 (Mo) and 0.6 (W) during the first 100 sliding cycles of running-in, which can be attributed to the evolution of the real contact area as well as the removal of contaminants and thin native oxide layers, resulting in higher adhesion and finally increased friction.²²⁷ Subsequently, the COF slightly decreases until it stabilizes at a steady-state-value of 0.6 or 0.4 for Mo and W, respectively. The smaller COF of W compared to Mo can be mainly traced back to its higher hardness leading to a smaller real contact area and less disruption of the native oxide film.

In contrast, the friction behavior drastically differs when Se nano-powder is added to the tribological interface before the tests. For both Mo and W substrates, the COF starts at a level like that of the reference measurements. However, independently of the used transition metal substrate, the COF continuously decreases over the course of the sliding experiment, ending up at a COF of 0.09 and 0.13 for the Mo (**Figure 4.1a**) and W (**Figure 4.1b**) substrates with Se nano-powder addition, respectively.

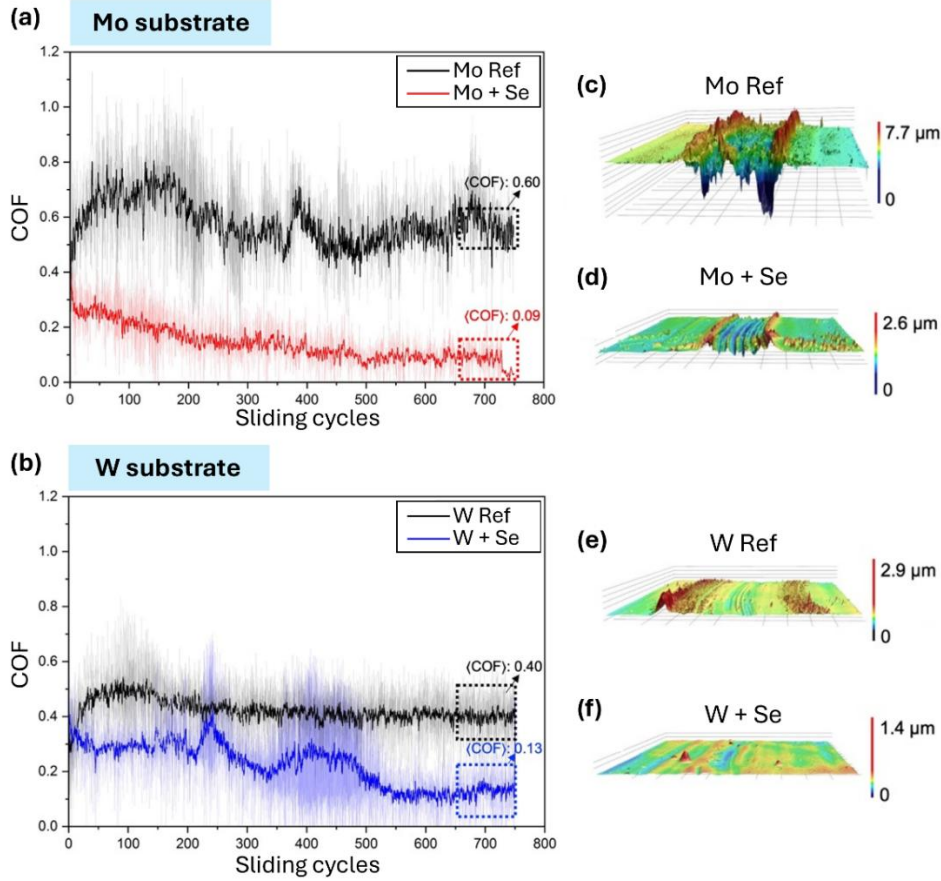


Figure 4.1: Friction (a,b) and wear (c)-(f) performance of the Mo and W substrates during ball-on-disk experiments. Compared to the bare substrates (black curves, REF), which show the typical frictional performance of a dry contact, the experiments with the addition of selenium nano-powder (red and blue curves for Mo and W substrates, respectively) demonstrate a continuous decrease in COF and a significant reduction in steady-state friction. Additionally, both (c,d) Mo and (e,f) W substrates demonstrate greatly reduced abrasive wear marks when Se nano-powder is added, as reported by 3D laser scanning microscopy. All the wear tracks have been imaged at the same magnification.

It is remarkable to achieve such a low macroscopic COF on an unlubricated metal-on-ceramic sliding contact under ambient conditions by simply sprinkling the contact zone with Se nano-powder. The improvement in the tribological performance as a result of the addition of Se nano-powder to the contact zone on the transition metal substrates is also reflected in the wear of these substrates (**Figure 4.1c-f**). When the experiments were performed with Se, the wear rate decreased by an order of magnitude, from $1.1 \cdot 10^{-4}$ to $2.7 \cdot 10^{-5} \text{ mm}^3 \text{ N}^{-1} \text{ m}^{-1}$ and $5.3 \cdot 10^{-6}$ to $3.9 \cdot 10^{-6} \text{ mm}^3 \text{ N}^{-1} \text{ m}^{-1}$ for Mo and W, respectively. We observed a clear reduction in wear in terms of wear groove shape and size, wear particle formation, and abrasive wear marks for the experiments performed with Se nano-powder (**Figure 4.1d and f**). Again, due to its higher mechanical hardness, W shows much lower wear in general compared to the Mo substrates when rubbing against the Al_2O_3 ball. This confirms less conformal contact with a smaller contact area, thus leading to lower friction.

We also explored the possible re-establishment of a low coefficient of friction through addition of further Se nano-powder into the tribological contact zone after the COF had reached the high value observed at the beginning of the tests (**Figure 4.2**). Indeed, the COF of the Mo-coated substrate drops after the first addition of Se powder and keeps constant up to around 700 sliding cycles (**Figure 4.2a**). Thereafter, frictional instabilities appear and the COF increases to 0.35 at approximately 1700 sliding cycles. This is exactly the point when the tribometer was stopped and the Se nano-powder was added again to the contact interface. It can be clearly observed that the COF rapidly decreases and reaches a rather constant level of about 0.1 up to 6500 sliding cycles, which also denotes the end of the test. In **Figure 4.2b**, the same trend is visible for the W-coated substrate. After the initial application of Se powder, the COF is around 0.17 up to 700 sliding cycles but then starts to increase to even 0.5 at around 850 cycles. After adding the Se nano-powder for the second time, the COF sharply drops down to approximately 0.17 again, where it remains constant up to 1200 cycles before slowly rising again. This straightforward experiment clearly shows the consistency of the approach, demonstrating that a further addition of Se nano-powder results in a repeatable and reproducible friction reduction. It can be envisioned that this cycle could be repeated again various times.

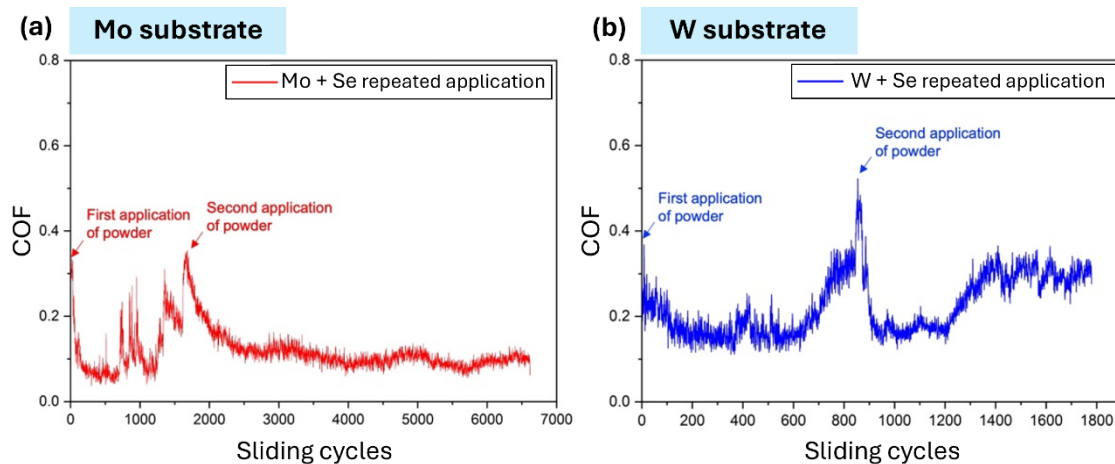


Figure 4.2: Reapplication of Se nano-powder leads to reoccurring reduction in friction, for both (a) Mo- and (b) W-coated substrate.

4.3.2 Tribofilm characterization - MoSe_2 and WSe_2 formation

To understand the tribochemical reactions taking place in the contact zone during relative sliding, we analyzed the substrate surfaces by Raman spectroscopy, XPS, and TEM.

Wear track analysis by Raman.

Raman spectra in **Figure 4.3** unambiguously shows that sliding induced tribochemical reactions occur in the contact zone. As expected, when performing experiments in ambient air atmosphere, sliding on the bare transition metal substrates is dominated by tribo-oxidation of Mo and W, leading to the formation of $\text{MoO}_3/\text{MoO}_2$ and WO_3 , which were found in the wear tracks of the Mo and W samples, respectively (**Figure 4.3b** and d). However, many of

the oxide peaks disappeared when Se nano-powder was added to the contact zone of the Mo (**Figure 4.3b**) and W (**Figure 4.3d**) samples. Instead, peaks related to the formation of MoSe₂ and WSe₂ became very clear. This statement is not entirely conclusive, as the peaks of MoO₂ at 210 cm⁻¹ and MoSe₂ at 242 cm⁻¹ as well as WO₃ at 265 cm⁻¹ and WSe₂ at 245 cm⁻¹ partly overlap. Nevertheless, these findings point towards a tribochemical reaction between the transition metal substrates and the Se nano-powder induced by the mechanical stresses and shear forces experienced during sliding, leading to the formation of lubricating TMDs, i.e. MoSe₂ and WSe₂. The formation of a tribofilm results in the reduction of friction and wear due to the easy-to-shear ability of layered TMDs which also provide protection to the underlying substrates.

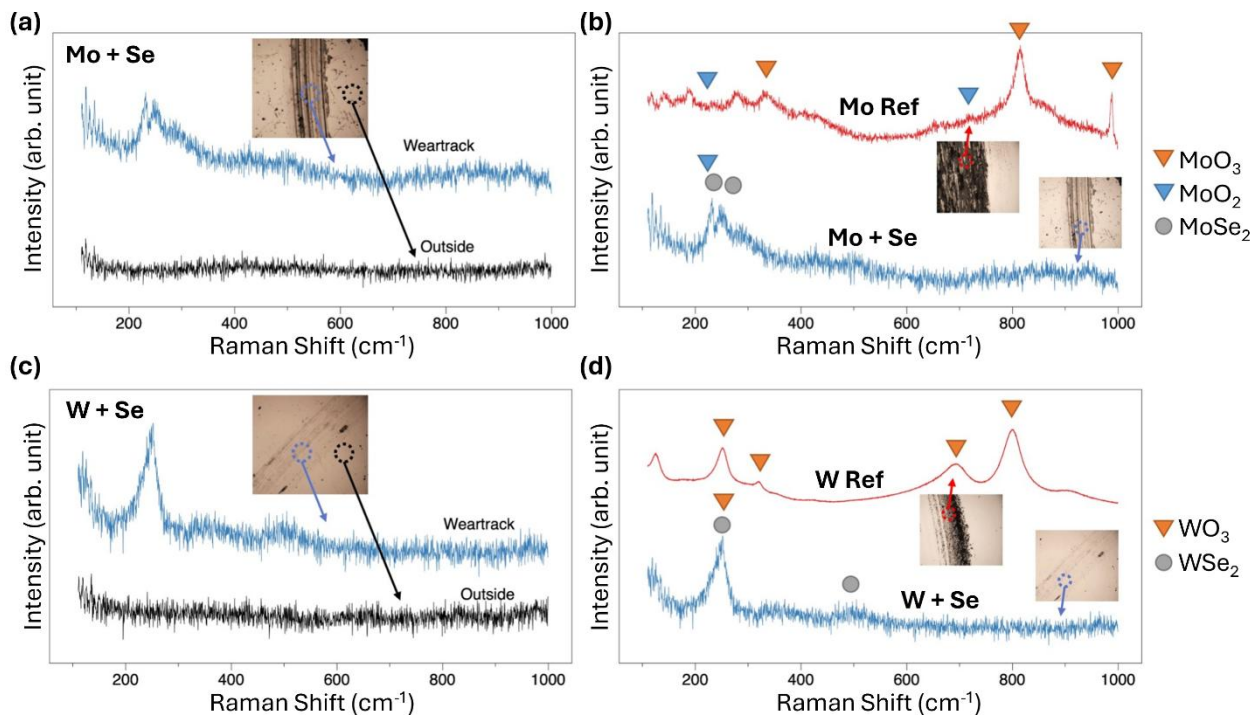


Figure 4.3: Raman spectra of the wear tracks of the (a,b) Mo and (c,d) W substrates. The addition of Se nano-powder triggers chemical reactions on both (a,b) Mo and (c,d) W substrates, so that selenides (MoSe₂, WSe₂) are formed. Without the addition of Se nano-powder, the formation of oxides dominates (MoO₃, MoO₂, WO₃).

Wear track analysis by XPS.

The high-resolution XPS scans performed inside the wear tracks are presented in **Figure 4.4**. The wear tracks from experiments performed on Mo substrates (**Figure 4.4a**) reveal the complex XPS envelope characteristic of molybdenum oxide samples containing mixed oxidation states. The main peak, located at 228.0 eV, is attributed to metallic Mo. The Mo 3d_{5/2} peaks are located at 230.8, and 232.6 eV and are assigned to the oxidation states Mo (IV) and Mo (VI).²²⁸ The addition of Se powder to the contact area before the tribological experiment results in a radical change in the chemical composition of the wear track. Aside from the major presence of metallic Mo (228.0 eV), the spectrum of the as-tested wear track reveals a

doublet of Mo 3d_{5/2} and Mo 3d_{3/2} centered at 228.8 and 231.8 eV, respectively. These peaks are characteristic of MoSe₂.²²⁹ Additionally, the presence of Mo (IV) and Mo (VI) can be identified. The *in operando* formation of MoSe₂ during the experiment is further confirmed by the presence of the characteristic selenide doublet at 54.6 eV (Se 3d_{5/2}) and 55.4 eV (Se 3d_{3/2}).²³⁰ Outside the wear scar, the surface composition was determined to be formed by metallic Mo and MoO₃, with a minor presence of MoO₂.

The XPS measurements performed on the W substrates offer analogous results (**Figure 4.4b**). Outside the wear scar, the measured spectrum contains only peaks corresponding to metallic W, W (IV) and W (VI). The XPS spectrum measured on the W substrate tested without Se shows a main doublet at 31.2 and 33.4 that corresponds to metallic W. The other peaks are ascribed to tungsten oxides (WO₂ and WO₃).²³¹ In the presence of Se nano-powder, the wear track shows a similar spectrum but with a pronounced doublet at 32.4 and 34.2 that corresponds to WSe₂. The Se narrow spectra again confirm the presence of WSe₂ with a main peak at 54.7 eV, accompanied in this case by the presence of a metallic tungsten satellite peak located at 56 eV.

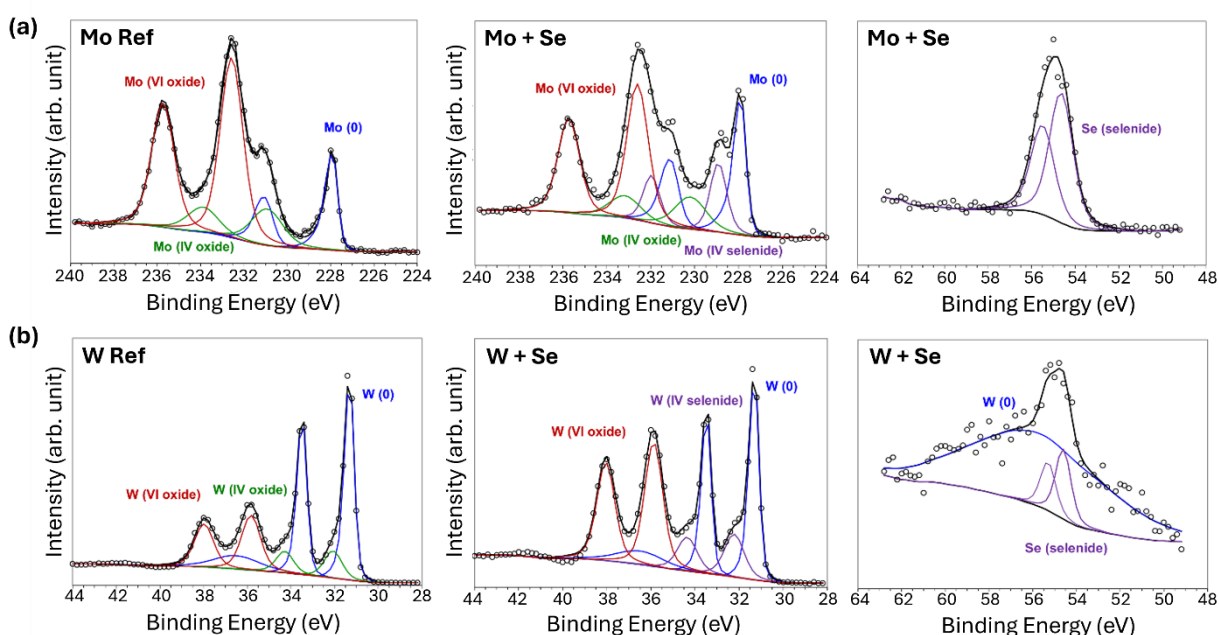


Figure 4.4: High-resolution XPS spectra of Mo 3d, W 3d and Se 2p illustrating the presence of MoSe₂ (Mo 3d_{5/2} and Mo 3d_{3/2} centered at 228.8 and 231.8 eV) and WSe₂ (doublet at 32.4 and 34.2 eV). The formation of selenides is confirmed by the presence of a doublet at 54.6 eV (Se 3d_{5/2}) and 55.4 eV (Se 3d_{3/2}). Note the lack of selenide formation in the reference samples (left side).

Wear track analysis by TEM.

Finally, the structural features of the formed tribofilms over the Mo and W substrates have been investigated by TEM. The results in **Figure 4.5** verify the formation of 2D layered TMDs on both substrates. The tribofilm found on the Mo substrate (**Figure 4.5a-c**) has a thickness of up

to 20 nm and is composed of clearly layered structures intermixed with amorphous zones. The tribofilm on the W substrate (**Figure 4.5d-f**) indicates a thickness of up to 10 nm and is, therefore, much thinner compared to the one on the Mo substrate. However, the tribofilm is more clearly delineated from the substrate and is composed of continuous layers. This can be explained by the larger resistance to plastic deformation of W, which prevents strong intermixing as found for Mo. The measured interlayer distances of about 7.1 Å are close to the ones corresponding to the (002) planes of hexagonal MoSe₂ and WSe₂.^{232,233} Additionally, the layers are perfectly aligned with respect to the substrate surface, thus enabling easy shearing and a low COF.

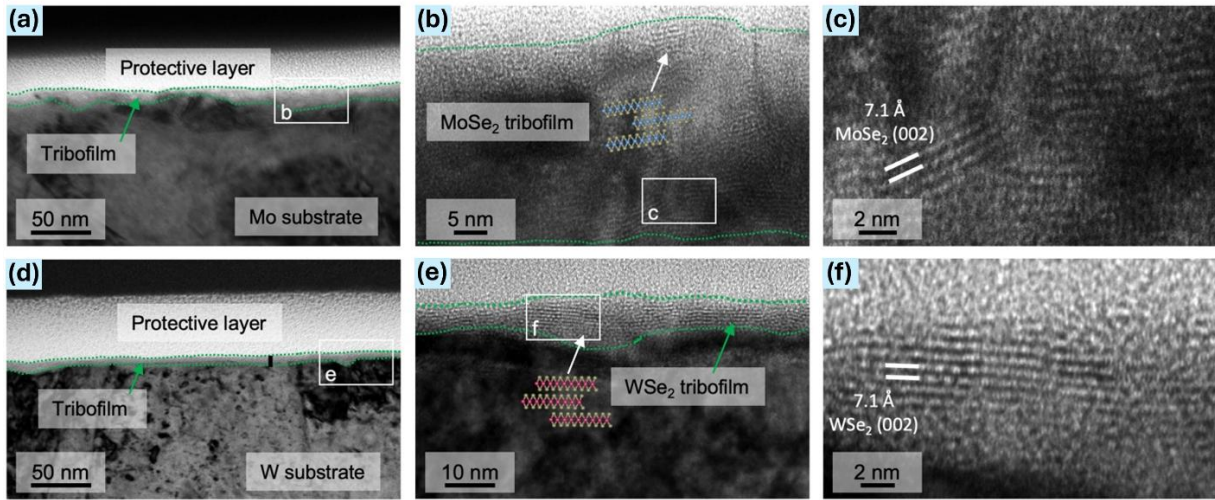


Figure 4.5: TEM micrographs of the tribofilms formed during the experiments on the (a)-(c) Mo and (d)-(f) W substrates with addition of Se nano-powder. The tribofilms are encircled with dashed green lines and the layer distances are measured and given in the high magnification images.

The finding of layered structures in the tribofilm combined with the Raman and XPS results clearly proves the *in operando* formation of low friction and low wear tribofilms based on transition metal selenides.

4.3.3 Mechanistic insights: Ab Initio Molecular Dynamics (AIMD)

As a first step to understanding the atomistic mechanism of TMD mechano-synthesis, we evaluated if the formation of TMDs from their metal and chalcogenides constituents is energetically favorable. To this aim, we compared the energy of a MoSe₂ (WSe₂) unit in the TMD layer with the sum of the energies of a Mo (W) atom and two Se atoms in their bulk structures. The results indicate that forming a TMD layer from the bulk constituents is highly favorable, the associated energy gain being 2.0 eV (1.1 eV) per MoSe₂ (WSe₂) unit. The lower energy gained by the formation of WSe₂ layers compared to MoSe₂ layers could also explain the shorter wear life of this system as it leads to less material being formed.

The energetic analysis described above points at the thermodynamic driving force for the transformation of the metal and chalcogenide elements into the TMD layers. To “observe” such a transformation in real time we performed AIMD simulations of Se nano-powder under load and shear in the presence of debris particles. We considered both pure metal and metal-oxide debris, the latter to consider the presence of MoO_2 , which was in fact revealed by the Raman analysis (**Figure 4.3**). The load and shear were applied through two TMD boundary layers to reduce the computational effort and to operate with the proper in-plane cell size to host a TMD layer that may be formed. Additionally, we considered a third case with the Se nano-powder confined within two perfectly flat Mo surfaces, representing the experimental conditions. **Figure 4.6a-c** shows different snapshots acquired during the AIMD simulations.

The initial configuration ($t = 0$ ps) for each dynamic simulation corresponds to the optimized system structure under load. The high applied load induces the weak Se-Se bonds to rearrange and adhere to the metallic nano-particles and the boundary TMD surfaces (**Figure 4.6a-b**) or to the metallic surfaces (**Figure 4.6c**). The system evolution is different in the three considered cases. When the pure metal nanoparticle is embedded in the chalcogenide powder (**Figure 4.6a**), we observe sliding-induced atom intermixing. Mo-Se bonds are established with trigonal prismatic coordination typical of TMDs. Already after 3.5 ps, one Mo atom (highlighted with a black circle) is fully surrounded by six selenium atoms, indicating a complete detachment from the metallic nanoparticle. After 35 ps of simulation, the metallic nanoparticle is almost completely disaggregated. At 136 ps the formation of the TMD is almost complete. The situation is different for the molybdenum-oxide nanoparticle (**Figure 4.6b**), where the intermixing of the metal and chalcogen atom is hindered by the presence of oxygen. The only relevant event observed in 36 ps consists in the partial extraction of one metal atom from the nanoparticle, which is still interacting with oxygen (see black circles in **Figure 4.6b**). The evolution of the third considered system, i.e. Se nanoparticle confined between ideal (110) Mo surfaces, is reported in **Figure 4.6c**. The cohesive energy of the atoms in the metallic surfaces is too high for their detachment, thus in the simulated time interval we do not observe the formation of any TMD unit. The Se nanoparticle disaggregates, but Se atoms chemisorb on the metal surfaces without affecting their surrounding environment.

The formation of TMD can be monitored quantitatively by computing the structure factor $S(G)$ of the Mo atoms:

$$S(G) = \sqrt{\frac{|\sum_{j=1}^N e^{iG \cdot r_j}|^2}{N^2}} \quad (4.2)$$

where G is the summation of the two reciprocal lattice basis vectors of a crystalline MoSe_2 layer and r_j is the real space position of the j -th Mo atom belonging to the debris particle or the Mo (110) surface. $S(G)$ has a limit value of 0 in case of full incommensurability, and of 1 for full commensurability of the lattices.²³⁴ In **Figure 4.6d**, we report the $S(G)$ evolution with time for the three AIMDs performed in this work. In line with the qualitative analysis in **Figure**

4.6a, the atoms belonging to the Mo₂₀ nanoparticle reorganize into an almost perfect MoSe₂ crystal structure within 80 ps (see the blue line). The S(G) values for the metal-oxide particle fall within the 0.2-0.4 range (black line in **Figure 4.6d**) indeed, Mo dioxide has the same stoichiometry and similar bonding as Mo selenide. Finally, The S(G) values close to 0 (see yellow line in **Figure 4.6d**), demonstrate that the atoms of the Mo surface retain the bulk geometry, which is in accordance to the results demonstrated in **Figure 4.6c**.

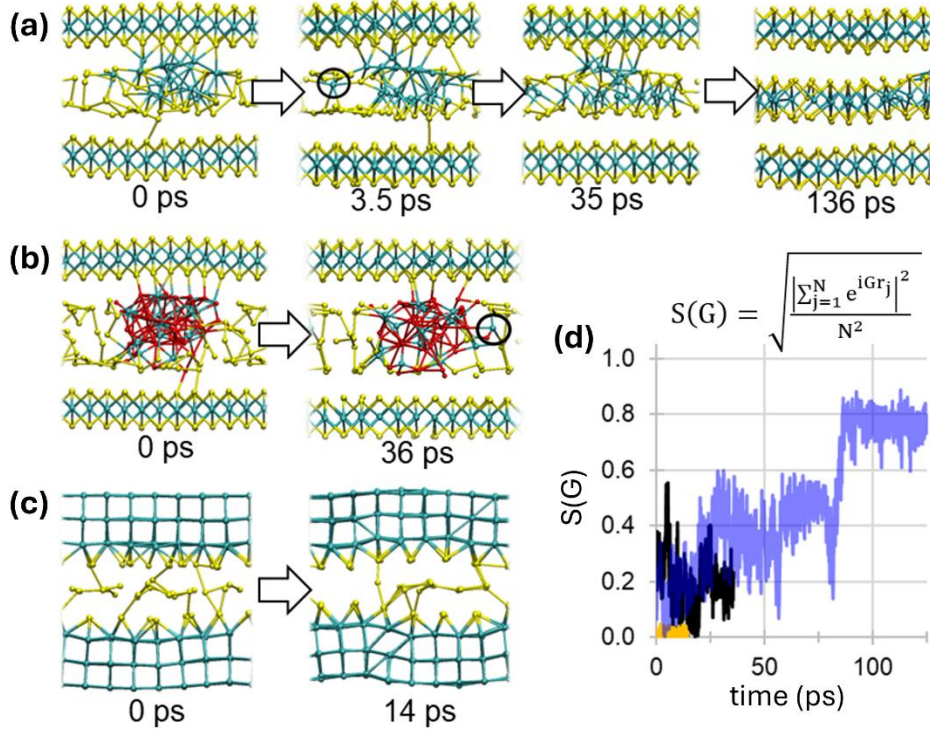


Figure 4.6: Dynamical evolution of three tribological systems: (a) Mo₂₀ debris particle and Se₄₀ nanoparticle; (b) Mo₂₀O₄₀ debris particle and Se₄₀ nanoparticle between two TMD boundary layers; (c) Se₆₄ nanoparticle confined within two Mo(110) surfaces. The black circles in panels (a) and (b) highlight the detachment of Mo atoms from the debris particles. Please refer to the color code: Mo in cyan, Se in yellow, O in red. (d) Time evolution of the structure factor, i.e. S(G), during the AIMDs for the Mo₂₀ debris particle (in blue), the Mo₂₀O₄₀ debris particle (in black) and the Mo(110) surface (in yellow).

The different degrees of Mo-Se intermixing observed in our simulations can be explained by the different binding energies of the metal atoms within the three different precursors considered. As shown in **Figure 4.7**, the calculated energies to extract a metal atom from a pure-metal nanoparticle, oxidized nanoparticle, or a metallic surface are 6.5 eV, 10.1 eV, and 8.7 eV, respectively.

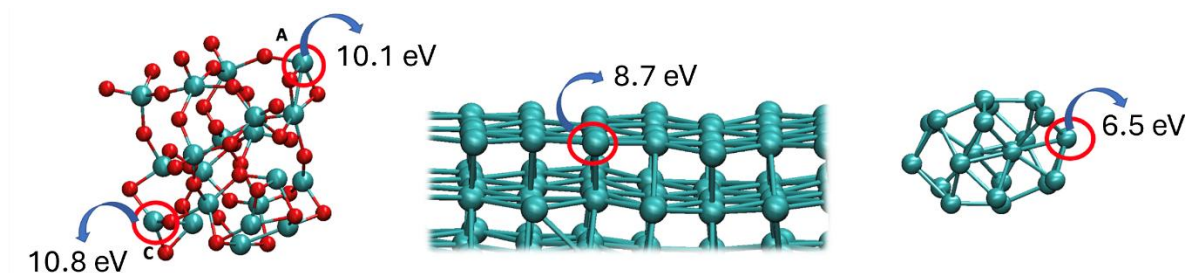


Figure 4.7: Energy cost to isolate a Mo atom from an the $\text{Mo}_{20}\text{O}_{40}$ debris particle, Mo(110) surface, and pure Mo particle.

The above-described simulations suggest that mechanical shear and load can promote the formation of crystalline MoSe_2 layers from a Se nano-powder as a precursor providing that metal atoms are extracted from the substrate, e.g., thanks to defects. While oxidized surfaces might be more easily damaged by rubbing, the extract of metal atoms from metal-oxide nanoparticles is more difficult. Therefore, the oxidic wear debris formed during rubbing cannot directly facilitate the formation of TMD layers. However, they can act as third body and, hence, accelerate abrasive wear and the extraction of metallic wear particles, which are then converted rapidly into TMD layers under shear and load once brought into contact with the Se nanoparticles.

4.4 Conclusions

In this chapter, we presented an innovative lubrication method for the *in operando* synthesis of slippery TMD layers by simply sprinkling a nano-powder of chalcogen elements, in this case selenium, at the tribological interface in ambient air. The formation of these TMD layers within the tribological contact significantly reduces friction and wear, lowering the coefficient of friction to 0.1 or even below, levels typically achieved only with fully formulated oils. Without the application of the nano-powder, both friction and wear are high, as expected for a dry contact between metal and ceramic, due to abrasive and adhesive interactions between the sliding surfaces caused by the hard oxides of Mo and W.

High-resolution characterization techniques, such as Raman spectroscopy and X-ray photoelectron spectroscopy (XPS), confirmed the formation of MoSe_2 and WSe_2 -based tribofilms on the interacting surfaces. Transmission electron microscopy further revealed the nanoscopic layered structure of MoSe_2 and WSe_2 , with a preferential crystalline alignment relative to the sliding surfaces.

We performed *ab initio* molecular dynamics simulations to investigate the shear-driven reaction pathways involved in the formation of layered TMDs during sliding. The simulations clearly highlight that metallic debris are a prerequisite to facilitate the tribochemical reaction between metallic particles and the Se nano-powder, leading to the formation of crystalline TMD layers. These metallic debris particles are likely generated during sliding, as the surfaces are weakened by oxidation.

Overall, our study demonstrates a straightforward and cost-effective approach, yielding highly reproducible results that underscore the strong affinity of Se nano-powder for the tribochemical formation of 2D selenides in the presence of a transition metal coating when brought together at the contact interface. Our approach may be considered for applications where the use of toxic gaseous reactants like H_2S is neither feasible nor desirable, in vacuum environments where outgassing of conventional oils and greases may hinder their use, or in maintenance-critical applications, where commonly used TMD coatings lead to component failure once they are fully worn. The results presented here may inspire further research into solid-state tribochemistry and the design of new composite materials that can provide long-lasting, self-sustaining, and self-healing capabilities in future applications through the replenishment of sliding contacts with solid lubricants.

The proposed lubrication mechanism based on the *in operando* formation of TMD layers is schematically shown in **Figure 4.8**.

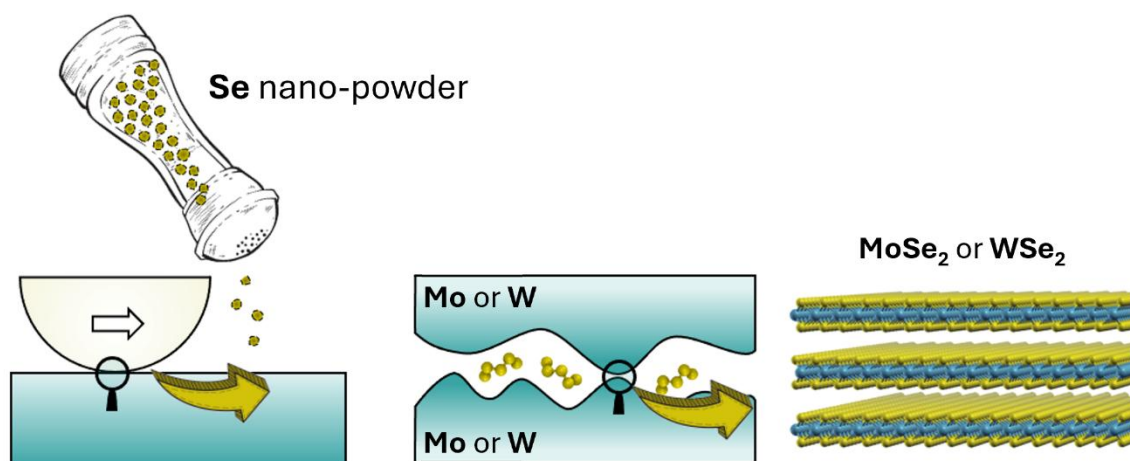


Figure 4.8: Schematic representation of the proposed lubrication method based on the friction-induced formation of slippery TMD layers *in operando*.

5. Transition Metal Carbo-Chalcogenides (TMCCs) as solid lubricants

Two-dimensional (2D) transition metal carbo-chalcogenides (TMCCs), consisting of an MXene core and a TMD-like surface, represent an inherent combination of TMDs and MXenes without the need to construct hybrids out of the individual layers. Due to their layered structure and surface chemistry, favorable tribological properties can be expected from these novel materials. In this chapter, we discuss the tribological performance of multilayer Ta₂S₂C and Nb₂S₂C TMCCs, deposited solely as a powder onto a steel substrate, tested under linear sliding against different counterbodies (Al₂O₃, SiC, AISI 304, and polytetrafluoroethylene).

5.1 Introduction

Many technological advances are only possible through the discovery of new and advanced materials. An example is the transition to clean energy, which is fueled by applied material science, making it possible to further reduce the cost of electricity from solar and wind or improve the efficiency of electric vehicles. One possibility to save huge amounts of energy is to reduce friction and wear, as discussed in chapter 1.1. This inspires the search for new lubricating materials, which demonstrate lower friction, protect the surfaces more from wear, and are stable over a wide range of conditions.

Two-dimensional (2D) materials with layered structures have been the focus of research as solid lubricant materials due to their exceptional mechanical, physical, and chemical properties.^{202,235–237} These properties stem from their unique structure, where the atoms within a layer (in-plane atoms) are held together by a mixture of ionic and/or covalent bonds, providing high strength. Meanwhile, adjacent out-of-plane layers are weakly bonded, interacting mainly through van der Waals (vdW) forces. This configuration results in atomic planes with a high strength yet can easily shear over each other. Due to their advantages in terms of vacuum and temperature stability, contamination resistance, and low friction, solid lubricants such as MoS₂ or WS₂ are the lubricating materials of choice for many space applications (e.g., Mars Rover, James Webb Space Telescope).²³⁸ However, challenges remain, such as their short wear life and the dependence of their tribological performance on the environmental conditions.²⁰² For instance, MoS₂ produces very low friction in vacuum or inert gas but reacts with humidity and oxygen in air to form MoO₃, thereby losing its exceptional tribological performance.⁵⁴

MXenes represent an extensive family of 2D materials, which have already generated interest for tribological applications,^{82,239} as extensively discussed in this thesis. Their properties can be tuned by leveraging their significant structural and chemical versatility.³⁹ Experimental testing has demonstrated very interesting performance for MXenes, specifically

in terms of outstanding wear life compared to MoS₂ or even WS₂.^{18,79,201} Additionally, under the right conditions even superlubric regimes can be achieved.^{203,240} A possibility to further improve the properties of 2D materials and to unlock synergistic effects is to stack different 2D materials into vdW heterostructures or nanocomposites,⁶¹ as exemplary presented within chapter 3 of this thesis. Numerous examples demonstrated that the friction and wear performance of 2D heterostructures and nanocomposites is greatly improved compared to their individual components. These include graphene/transition metal dichalcogenide (TMD) heterostructures,⁶¹ TMD/TMD heterostructures, e.g., MoS₂/MoSe₂,⁶² or Ti₃C₂T_x/MoS₂ nanocomposites.^{63,64} Utilizing the aforementioned heterostructures or nanocomposites might be a viable option to expand the parameter space for sustaining effective lubrication. Indeed, combinations of MXenes i.e., Ti₃C₂T_x with MoS₂⁶³ or MoSe₂²⁴¹ have proven to provide very low friction (even in the superlubric range between 0.007-0.01).

On the other hand, the tribological community completely overlooked a family of new 2D materials, which can be considered an inherent and exciting combination of MXenes and TMDs, so called transition metal carbo-chalcogenides (TMCCs).⁴⁰ Although the synthesis of many TMCCs in bulk 3D-form such as Ta₂S₂C and Nb₂S₂C had already been achieved in the past century,^{93,94} it is only thanks to the successful exfoliation of TMCCs into single layers achieved by Majed et al.,⁴⁰ that this family of 2D materials has definitely gained the attention of the scientific community, especially in the fields of electrochemical energy conversion and storage.⁴¹ To date there is only one study by Wally and Ueki that explores the tribological properties of Ta₂S₂C and (Ta, Nb)₂S₂C transition metal carbo-chalcogenides.⁹⁵ However, the research did not continue, and the family of 2D materials remained unexplored until today. Compared to heterostructures, TMCCs have the advantage that the solid/solid interface can be engineered in a very controlled fashion, they can be considered as an interface-free hybrid of TMD and MXene. The intriguing combination of a MXene core and a TMD surface might give important insights into the role of mechanical stability provided by the layer core, and the chemical composition of the surface determining environmental stability, reactivity, and interlayer binding, all of which affect tribological behavior.

In this chapter, we describe for the first time the tribological properties of multilayer Ta₂S₂C and Nb₂S₂C TMCCs deposited solely as powders onto AISI 304 steel substrate, in linear reciprocating sliding against different counterbody materials (i.e., Al₂O₃, SiC, AISI 304, and polytetrafluoroethylene). Despite the simplicity of this first exploring approach, the presence of TMCC powders in the contact area is sufficient in most cases to maintain a coefficient of friction (COF) lower than 0.2, which is considered a threshold for effective solid lubrication.^{242,243} The lubrication ability of TMCC is traced back to the tribo-induced formation of a compacted patchy tribofilm, which reduces the COF and prevents the substrate from wear. X-ray photoelectron spectroscopy (XPS) and Auger-Meitner electron spectroscopy (AMES) highlighted the presence of TMCCs inside the wear tracks. The 2D structure of TMCCs was detected inside the tribofilm by transmission electron microscopy (TEM). Finally, density

functional theory (DFT) simulations were carried out to confirm the easy-to-shear ability of TMCCs, suggesting that their 2D structure can accommodate shear between layers.

5.2 Methods

Synthesis and Characterization of TMCCs. Niobium carbo-sulfide ($\text{Nb}_2\text{S}_2\text{C}$) and tantalum carbo-sulfide ($\text{Ta}_2\text{S}_2\text{C}$) were obtained by solid-state synthesis followed by chemical purification. $\text{Fe}_x\text{Nb}_2\text{S}_2\text{C}$ was synthesized using commercial precursors of niobium (Nb, 99.8%, < 45 μm , Alfa Aesar), niobium carbide (NbC, 99%, < 10 μm , Alfa Aesar), iron (II) sulfide (FeS, 99%, 60 – 200 μm , STREM). Powders with an atomic ratio of Nb: NbC: FeS = 1.0: 1.0: 1.5 were weighed inside an Argon (Ar)-filled glovebox. Yttrium stabilized zirconia balls (10 balls, 5 mm each) were added to high density polyethylene container as mixing media along with the powders. The container was sealed with parafilm in the glovebox, then transferred outside the glovebox to a Turbula T2F mixer, where it was mixed at ~56 rpm for 3 h. The mixed powders were returned to the glovebox and cold-pressed under 300 bars into 1-inch pellets. These pelletized samples were then placed in an alumina crucible inside a tube furnace and heated under a constant Ar flow at a rate of 10 $^{\circ}\text{C}/\text{min}$ to 1550 $^{\circ}\text{C}$, where they were held for 30 min. The pellets were then allowed to cool to room temperature. After cooling, the pellets were pulverized and sieved through a 325 mesh (< 44 μm). $\text{Nb}_2\text{S}_2\text{C}$ was obtained by etching $\text{Fe}_x\text{Nb}_2\text{S}_2\text{C}$ using aqueous hydrochloric acid (12 M HCl) with a ratio of 20 ml HCl for each 1 g of starting powder. The solution was heated to 30 $^{\circ}\text{C}$ using a hot plate for 48 h and mixed with the aid of a Teflon-coated magnetic stir bar. The sample was washed with deionized (DI) water until near neutral pH was reached. Similarly, $\text{Fe}_x\text{Ta}_2\text{S}_2\text{C}$ was synthesized by mixing tantalum (Ta, 99.9%, < 150 μm , Alfa Aesar), tantalum carbide (TaC, 99.5%, < 44 μm , Alfa Aesar), and iron (II) sulfide in a molar ratio of Ta: TaC: FeS = 1.0: 1.0: 1.75. $\text{Ta}_2\text{S}_2\text{C}$ was obtained from $\text{Fe}_x\text{Ta}_2\text{S}_2\text{C}$ by mixing the ground sample (< 44 μm) with 12 M HCl at 30 $^{\circ}\text{C}$ for 48 h followed by washing. After washing the sample with DI water to a pH ~ 7, the dried sample was obtained by vacuum-assisted filtration.

The crystal structures of the investigated samples were analyzed using a Rigaku D/Max-2200 X-ray diffractometer with a Cu K α source. Scans were performed with a 2 θ step size of 0.02 $^{\circ}$ and a sweep rate of 1 $^{\circ}/\text{min}$. Scanning electron microscope (SEM) images were obtained using a Hitachi S-4800 microscope at an acceleration voltage of 3 kV, while images were processed with an image processing software (ImageJ). Chemical compositions were confirmed through energy dispersive x-ray spectroscopy (EDS) analysis with an Oxford-Hitachi S-3400 microscope at an accelerating voltage of 30 kV.

Tribological Experiments. Frictional testing of the TMCCs was conducted using a ball-on-disk tribometer (*Rtec Instruments, MFT-2000A*) in linear reciprocating sliding with a stroke length of 1 mm. As substrate material we used AISI 304 (100Cr6) steel platelets with a size of 20 x 20 x 1 mm³, Young's modulus of 200 GPa, Poisson ratio of 0.29, and an initial roughness S_q of 0.18 μm . Various counterbody materials were employed (Al_2O_3 , SiC, 100Cr6, and PTFE).

All had a diameter of 6 mm, except for PTFE, which was 6.35 mm. The linear sliding velocity was set at 1 mm/s and the normal force was 0.25 N. This load corresponds to Hertzian contact pressure of 0.45, 0.48, 0.40 and 0.012 GPa for Al_2O_3 , SiC, 100Cr6 and PTFE, respectively. The temperature during the measurements ranged between 19.5 and 24.8 °C, and the relative humidity between 23% and 46%. After mounting the sample in the tribometer, we deposited the synthesized TMCCs powder onto the substrate using a spatula. Although this method does not ensure strong adhesion to the substrate, it served as a useful test to evaluate the performance of the TMCCs powder without employing more advanced deposition techniques. About 10 ± 2 mg of powder was spread over the steel substrate. Then, the counterbody was brought into contact with the TMCC powder, ensuring visible transfer of the loose powder from the substrate to the counterbody. Afterwards, the sliding tests started. Additionally, tests without powder addition were run. The tribological experiments were repeated three times for statistical representation, and the curves were used to calculate the corresponding mean values and standard deviations.

Linear reciprocating sliding tests were repeated using WS_2 and $\text{Ti}_3\text{C}_2\text{T}_x$ MXene powders as benchmark materials. We used the same tribological parameters as previously described (i.e., stroke length = 1 mm, sliding velocity = 1 mm/s, normal force = 0.25 N) with an Al_2O_3 counterbody, resulting in a Hertzian contact pressure of 0.45 GPa. All the samples were imaged by confocal laser scanning microscopy (CLSM, Keyence VK-X1100) before and after the friction tests.

Tribofilm characterization.

The XPS measurements were carried out on a PHI Versa Probe III-spectrometer equipped with a monochromatic Al-K α X-ray source and a hemispherical analyser (acceptance angle: $\pm 20^\circ$). Pass energies of 55 eV and step widths of 0.1 eV were used for XPS detail spectra (Excitation energy: 1486.6 eV; Beam energy and spot size: 12.5 W onto 50 μm ; Mean electron take-off angle: 45° to sample surface normal; Base pressure: $< 8 \times 10^{-10}$ mbar; Pressure during measurements: $< 1 \times 10^{-8}$ mbar). Samples were mounted on double-sided polymer tape. Electronic and ionic charge compensation was used for all measurements (automatized as provided by PHI). Surface cleaning was carried out using a gas cluster ion source (2.5kV, 10nA, 15min). Data analysis was performed using CASA XPS and Multipak software packages, employing transmission corrections, Shirley/Tougaard backgrounds,^{244,245} and customised Wagner sensitivity factors.²⁴⁶ Deconvolution of spectra was carried out by using a Voigtian line shape (LA(50)). Two characteristic peaks were used to characterize $\text{Nb}_2\text{S}_2\text{C}$ (in Nb 3d $_{5/2}$ at 202.8 eV, assigned to S-Nb-C bonding) and $\text{Ta}_2\text{S}_2\text{C}$ (in Ta 4f $_{7/2}$ at 23.7 eV, assigned to S-Ta-C bonding), according to Majed et al.⁴⁰

All Auger-Meitner Electron Spectroscopy (AMES) and EDS measurements were carried out on a PHI 710-spectrometer equipped with a field emission gun electron source, a cylindrical mirror analyzer (AMES) and an Oxford Instruments Ultim $\text{\textcircled{M}}$ Max 100 detector (EDS). Excitation

energy: 10 kV@10nA used for AMES and EDS. AMES/EDS maps are recorded using 256x256 and 512x512 pixels (1024 channels, process time: 5ms), respectively. Image stabilization is used for AMES maps. AMES survey spectra were recorded in a range from 50 to 2200 eV in 0.5 eV steps (3 scans). The base system pressure was $<1 \times 10^{-9}$ mbar and pressure during measurements: $< 1 \times 10^{-8}$ mbar. While the samples were on the same holder also used in XPS, additional Cu/Be clamps were added for a better electrical contact of the sample surface. Data analysis was carried out using PHI Multipak (AMES) and Oxford AZTEC (EDS) software packages. The relative sensitivity factors are provided by PHI.

Transition electron microscopy (TEM, FEI TECNAI F20) was used to image the structure of the formed tribofilms. EDS inside the transmission electron microscope was performed using an EDAX-AMETEK Apollo XLTW SDD system. For TEM investigation, a thin lamella was prepared by ThermoFisher Scios II Focused Ion Beam (FIB). The TEM lamellae had a size of about $30 \times 10 \mu\text{m}^2$, with a thickness of < 100 nm at the regions of interest. Selected Area Electron Diffraction (SAED) patterns were used for phase analysis. Additionally, high resolution-TEM (HR-TEM) imaging was performed for phase analysis using Fourier Transformation (FT) and the measurements of lattice spacings in the HR-TEM images.

Numerical Simulations. We carried out Density Functional Theory (DFT) simulations by using the Quantum ESPRESSO software (version 7.2).^{139–141} The Perdew-Burke-Ernzerhof (PBE) exchange-correlation functional was employed,¹⁰³ with the inclusion of van der Waals corrections according to Grimme's D2 method.¹⁴² In particular, the standard C_6 coefficient and the van der Waals radius R_0 parameters of the metal atoms (Nb and Ta) have been replaced with those of the preceding noble gas in the periodic table (Kr and Xe, respectively). This scheme (referred to as D2_{NG}) has been presented in chapter 2.2.1, providing a better description of the dispersion forces involving transition metal atoms with positive oxidation states inside 2D-materials.⁹¹ The electronic wave-function (charge density) was expanded on a plane-waves basis truncated with a cutoff of 50 Ry (400 Ry), while ionic species were treated with “rrkj” ultrasoft pseudopotentials. Convergence thresholds of 10^{-4} Ry and 10^{-3} Ry/Bohr for the total energy were adopted for atomic relaxations. We adopted a Gaussian smearing of 0.02 Ry to describe the electronic states occupation around the Fermi level. Both Nb₂S₂C and Ta₂S₂C were modeled through trigonal unit cells (group symbol $R\bar{3}m$, group number 166), whose Brillouin zone was sampled with a $16 \times 16 \times 1$ Monkhorst-Pack grid.¹⁴³ WS₂ (group symbol $P6_3/mmc$, group number 194) was modelled with hexagonal unit cell, using a $20 \times 20 \times 1$ grid to sample the Brillouin zone. To avoid artificial interactions between replicas, 15 Å of vacuum were included along the out-of-plane direction. The work of separation (W_{SEP}) is calculated as the opposite of the adhesion energy (E_{ADH}):

$$W_{\text{SEP}} = -E_{\text{ADH}} = -\frac{2E_{\text{M}} - E_{\text{B}}}{A} \quad (5.1)$$

where E_{M} is the total energy of the relaxed monolayer, E_{B} is the total energy of the bilayer in its most favorable configuration, and A is the area of the cell. To evaluate the potential energy

surface (PES) we repeated the calculation of W_{SEP} at different relative lateral positions. The potential corrugation (ΔW_{SEP}) rises from the difference between the maximum and minimum W_{SEP} of the PES (i.e., $\Delta W_{\text{SEP}} = W^{\text{max}} - W^{\text{min}}$). Details about the lateral positions used to construct the PES can be found in **Figure 5.1**, which also shows the unit cell employed in our models.

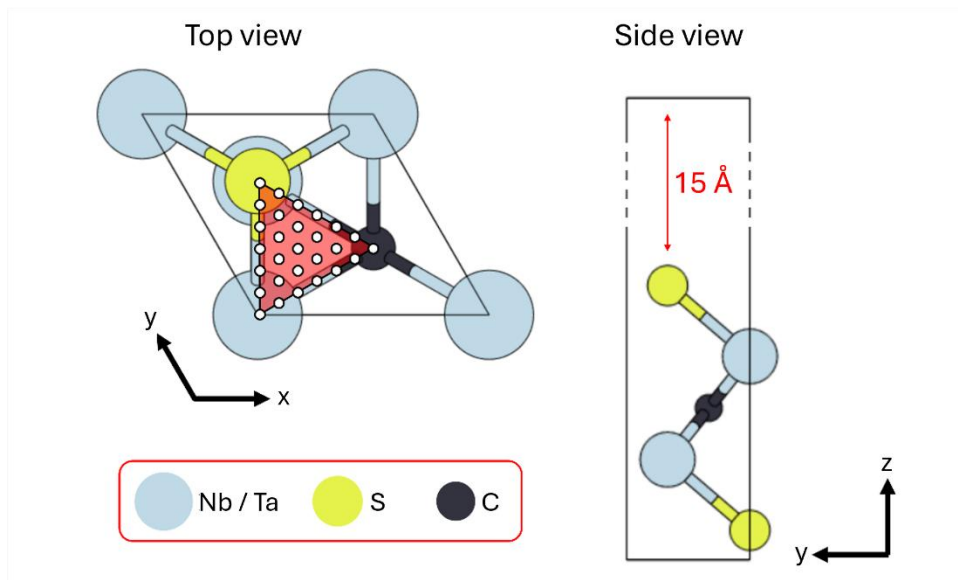


Figure 5.1: Hexagonal unit cell employed to model TMCCs. The sampling grid within the top view shows the lateral displacements employed to construct the PES. The highlighted area represents the irreducible portion that was replicated through symmetry operations to fill all the unit cell. The internal ABC stacking of TMCCs can be appreciated in the side view.

5.3 Results and Discussion

5.3.1 Characterization of the TMCCs

The TMCC powders studied here are multilayered, featuring a transition metal carbide core and chalcogen surface chemistry. $\text{Nb}_2\text{S}_2\text{C}$ and $\text{Ta}_2\text{S}_2\text{C}$ multilayer powders were synthesized using a simple and scalable powder metallurgy process, followed by a chemical treatment to remove excess Fe (FeS was used as the source of S during synthesis). **Figure 5.2a** presents SEM images of $\text{Nb}_2\text{S}_2\text{C}$ and $\text{Ta}_2\text{S}_2\text{C}$ multilayer particles and EDS elemental maps of Nb/Ta, S, and C, confirming uniform distribution. The Fe signal remains quite intense, despite the use of various etching trials to reduce the iron content.⁴⁰ Indeed, EDS quantitative analysis revealed ratios of Nb:Fe = $2.00:0.14 \pm 0.06$ and Ta:Fe = $2.00:0.31 \pm 0.01$, indicating incomplete Fe removal. However, to date, there are no reports in the literature of successfully achieving complete Fe removal from TMCC multilayers using hydrochloric acid etching. The average particle size of $\text{Nb}_2\text{S}_2\text{C}$ is $16.7 \pm 3.06 \mu\text{m}$, while for $\text{Ta}_2\text{S}_2\text{C}$ the average particle size is $11.0 \pm 4.57 \mu\text{m}$.

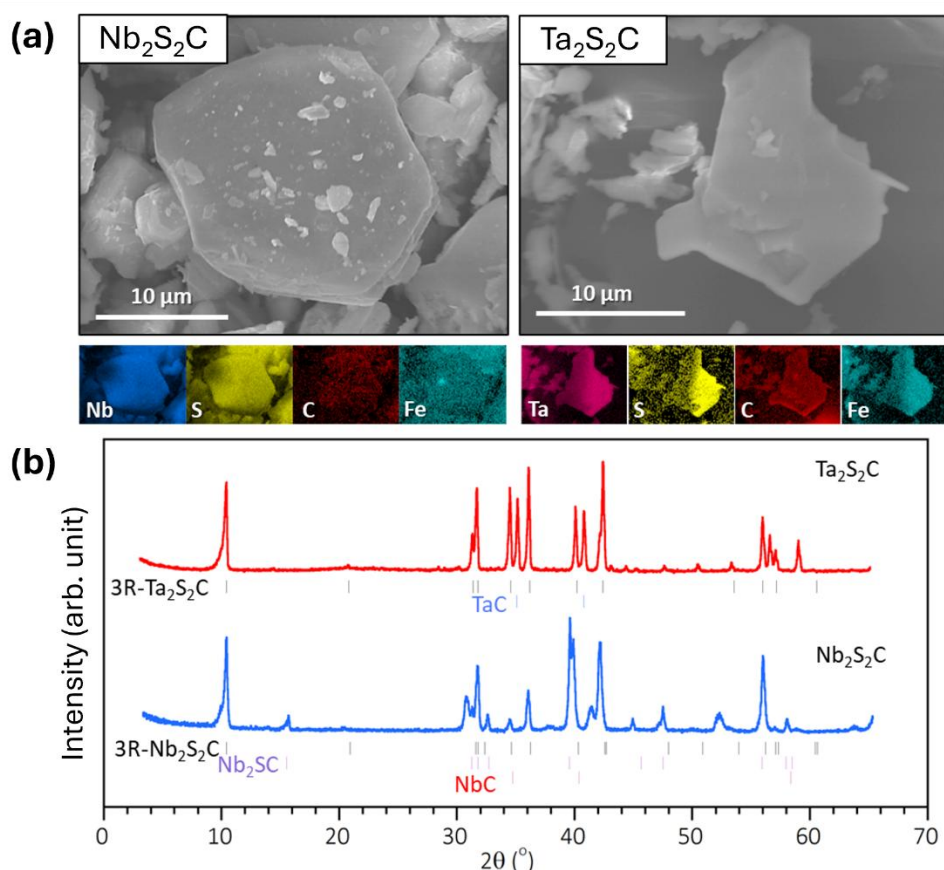


Figure 5.2: (a) SEM images of Nb₂S₂C and Ta₂S₂C particles in addition to EDS elemental map of Nb/Ta, S, C, and Fe. (b) XRD pattern of Nb₂S₂C with references of 3R-Nb₂S₂C (PDF#01-070-8925), Nb₂SC (PDF#00-021-0604), NbC (PDF#01-070-8416), 3R-Ta₂S₂C (PDF#00-024-1258, and TaC PDF#03-065-8264).

XRD patterns in **Figure 5.2b** confirm the successful phase formation of Nb₂S₂C and Ta₂S₂C after chemical treatment, although secondary phases such as Nb₂SC, NbC, and TaC were also observed. The lattice parameters of TMCCs have been determined from the recorded powder x-ray diffraction patterns. The crystal structure of TMCCs is trigonal with space group symbol $R\bar{3}m$, the lattice parameters in the x, y, and z directions are denoted as *a*, *b*, and *c*, respectively, with *a* = *b*. For Nb₂S₂C, *a* = 3.31 Å and *c* = 26.68 Å, while for Ta₂S₂C *a* = 3.29 Å and *c* = 26.59 Å. Since three TMCC layers are stacked within a single unit cell, the resulting interlayer distance is approximately 8.88 Å, calculated by dividing the *c* vector by three. The XPS analysis of the as-synthesized TMCCs nanolayers was conducted and reported in a previous work,⁴⁰ where Nb, S, and C peaks were detected, while no Cl signal from HCl etching was observed in neither TMCCs.

5.3.2 Tribological performance

We assessed the tribological performance of the as-synthesized TMCC multilayer powders on a ball-on-disk tribometer in linear sliding mode. **Figure 5.3a** demonstrates the evolution of the COF of the two different TMCC samples (viz., Nb₂S₂C and Ta₂S₂C) against a hard and

chemically inert Al_2O_3 counterbody over time. Their frictional behavior is compared to a steel reference sample without the addition of any lubricating material. Without the addition of TMCC powders, the steel sample against the Al_2O_3 counterbody demonstrated the typical behavior of a non-lubricated metal surface sliding against a ceramic counterbody, with pronounced fluctuations during the running-in period and a rapidly rising COF.²²⁷ Specifically, the COF started at around 0.4 and quickly increased during the first 500 s, after which the COF remained steady and stable between 0.7 and 0.8. On the other hand, TMCC-lubricated surfaces started at a much lower COF of ~ 0.15 . Afterwards, the COF slightly increased constantly but remains low (around 0.2) throughout the entire measuring duration of 1800 s, almost identically for both $\text{Ta}_2\text{S}_2\text{C}$ and $\text{Nb}_2\text{S}_2\text{C}$. These low COF values are astonishing especially since they were achieved by simply adding lubricious material in the form of powders to the contact area, without the need of a coating process.

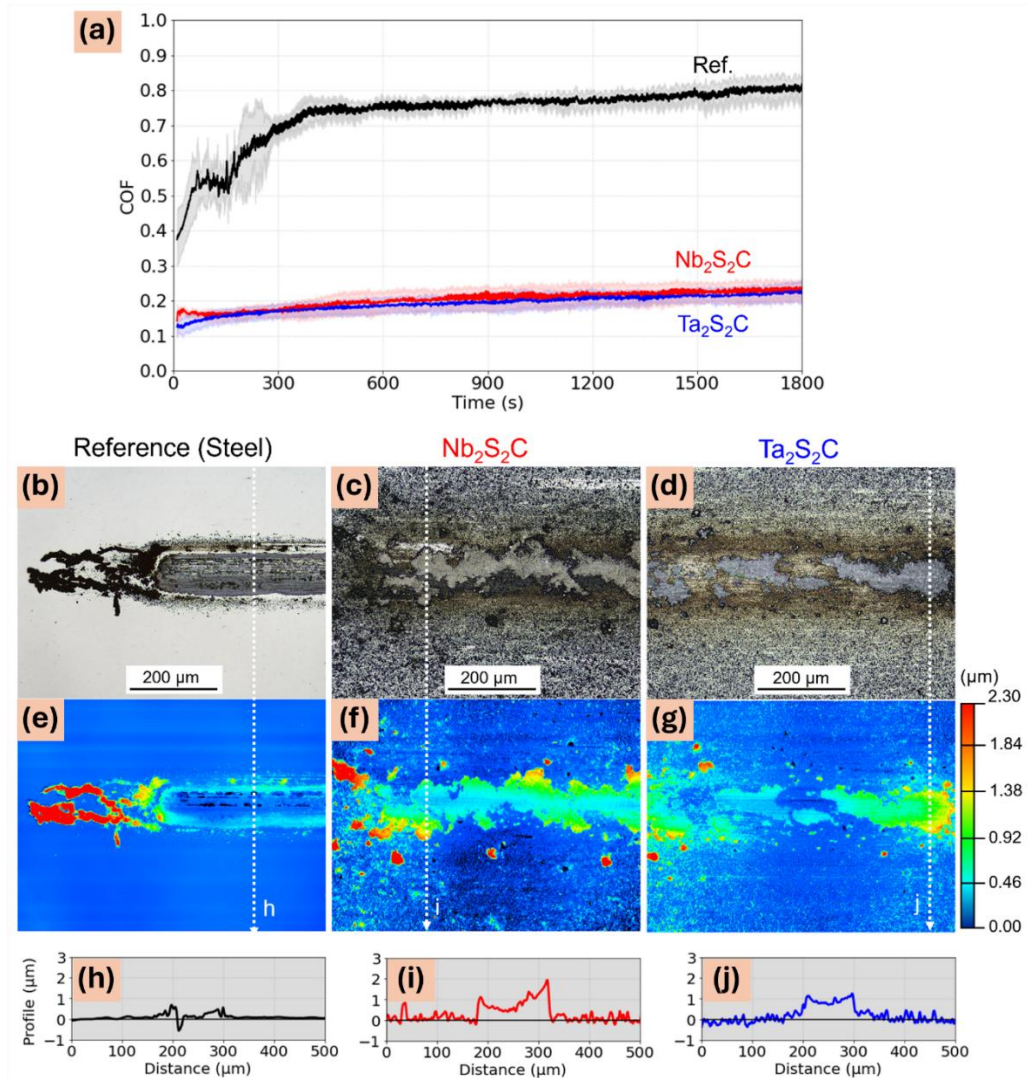


Figure 5.3: (a) Tribological performance of $\text{Nb}_2\text{S}_2\text{C}$ and $\text{Ta}_2\text{S}_2\text{C}$ powders against an Al_2O_3 counterbody. (b)-(d) laser scanning microscopies and (e)-(g) corresponding depth profiles for the reference and TMCC cases. (h)-(j) 1D cross-section height profiles acquired along the white dashed lines.

The wear track morphologies after the tribo-tests are reported in the bottom part of **Figure 5.3** for (b) the reference case, (c) Nb₂S₂C and (d) Ta₂S₂C. Height maps of the same areas are also provided beneath the optical images in addition to profiles along the dashed lines (**Figure 5.3e-j**). Significant abrasion marks were found when the Al₂O₃ ball was rubbed against the steel plate without the addition of any lubricious material. This was also clearly observed in the depth profiles (**Figure 5.3e**) and height maps (**Figure 5.3h**), which showed wear up to a maximum depth of ~ 0.5 µm in addition to the debris pile up at the reversal point as well as along the sides of the wear track. Conversely, no wear was detected in the TMCC-lubricated steel substrate (**Figure 5.3f-g**). Instead, volume build-up along the wear track length can be observed due to the formation of a protective layer, thus preventing the direct contact between the tribo-pair. This holds true for the case of Nb₂S₂C powder, where a patchy tribofilm covered the substrate all along the wear track. For Ta₂S₂C, the tribofilm appeared less thick and patchier; although showing some discontinuities and reduced compactness, such layer was sufficient to prevent abrasive wear, since no remarkable wear scar can be identified inside the wear track. Similar tribofilm morphologies have been found for other loosely bound solid lubricant films.^{64,243} Height profiles across the Nb₂S₂C- and Ta₂S₂C-based tribofilms (**Figure 5.3i-j**) highlight their similar shape with a concave form resulting from the ball's shape. The formation of the protecting tribofilm relates to the uncontrolled compacting of TMCC powder over the substrate, thanks to the mechanical force exerted by the counterbody. Therefore, the morphology and thickness of the resulting tribofilm were somehow affected by stochastic parameters (e.g., the amount of TMCC particles in the contact area and their size). That would explain the minor differences observed between Nb₂S₂C and Ta₂S₂C.

Additionally, we performed experiments with counterbodies (CBs) of different nature: SiC, PTFE, and 100Cr6 steel, to assess the dependence of TMCC's tribological performance on the material pairing. In **Figure 5.4** we report the results involving the Ta₂S₂C powder. Clearly, the tribological performance greatly depends on the used CB. With silicon carbide CB, the addition of Ta₂S₂C powders provide great lubrication (**Figure 5.4a**), almost identical to what observed in **Figure 5.3a** for Al₂O₃ CB. On the other hand, experiments with the steel CB revealed very little beneficial effects of the lubricious Ta₂S₂C powders (**Figure 5.4c**). Interestingly, friction was even higher than the reference sample in case of the PTFE CB (**Figure 5.4b**), which can be associated to the friction reducing effects of PTFE.²⁴⁷ While this might seem like a negative result at first, it is nonetheless clear proof of the formation of a tribologically active tribofilm composed of TMCC, which shields the rubbing surfaces and accommodates shear. This shielding is why PTFE cannot be effective as a lubricating material and the COF of the tests with the TMCC powder is higher, in fact almost identical to the tests with the Al₂O₃ CB. In summary, both ceramic CBs (SiC and Al₂O₃) showed a clear reduction in friction compared to the non-lubricated reference samples, with the highest reduction in friction for the Al₂O₃ CB.

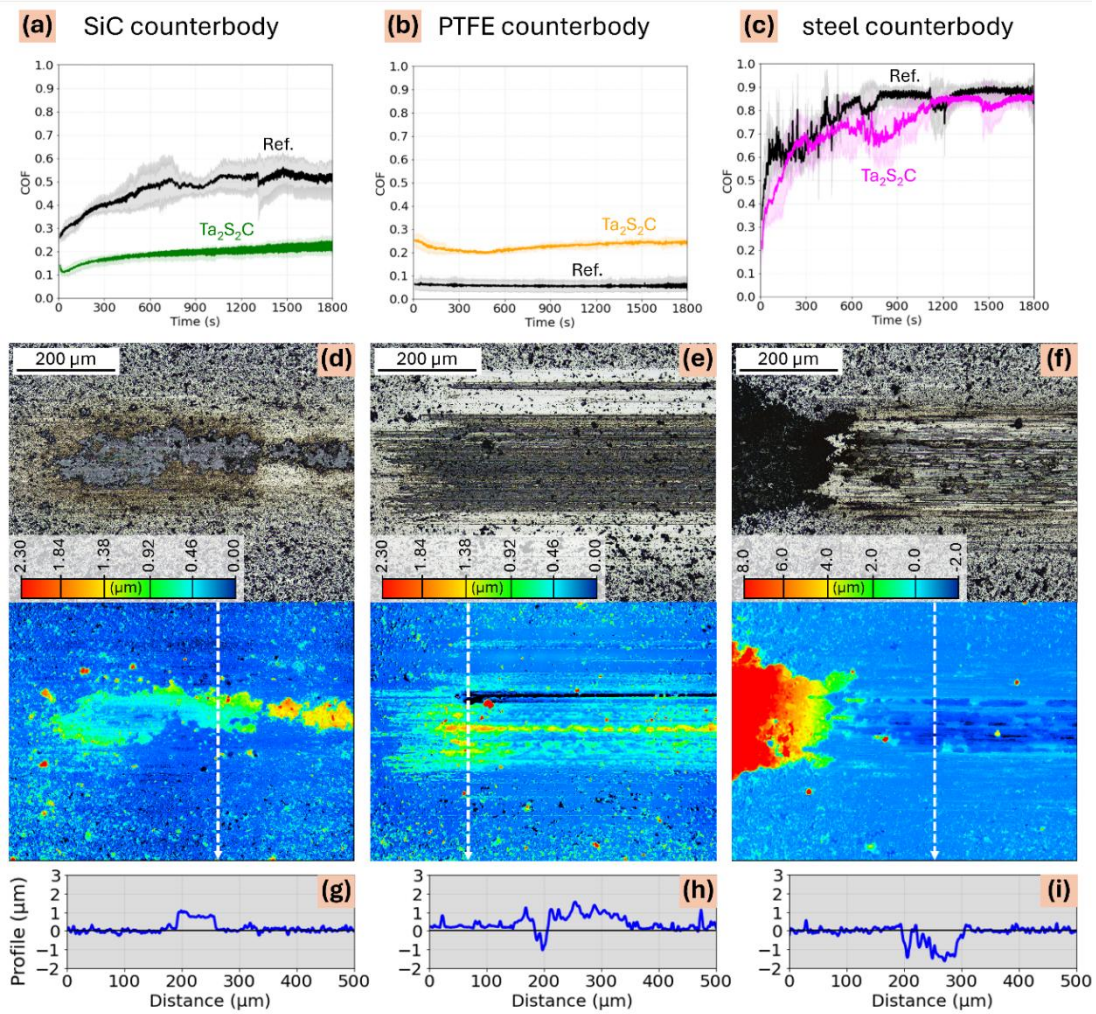


Figure 5.4: (a) Tribological performance of Ta₂S₂C powder against different counterbodies (a) SiC, (b) PTFE, and (c) steel. (d)-(f) laser scanning microscopies and depth profiles for the case with Ta₂S₂C powder in the tribological contact. (g)-(i) 1D cross-section height profiles acquired along the white dashed lines.

Images of the wear tracks were profiled by laser scanning microscopy for each of the considered materials and are shown in **Figure 5.4d-f**. We discussed that both ceramic CBs exhibited low and stable COFs, while supporting the formation of a passivating patch-like tribofilm that prevents abrasive wear. Indeed, Al₂O₃ (**Figure 5.3d**) and SiC (**Figure 5.4d**) lead to indiscernible tribofilms of similar compactness and thickness. For the PTFE counterbody, the resulting film was much less compacted (**Figure 5.4e**), although it effectively hosting the sliding interfaces (same COF trend). The less compacted film when using PTFE can be explained by the much smaller acting contact pressure due to the lower elastic modulus of PTFE. Interestingly, a tiny abrasive scar was also visible in the upper part of the wear track. Since PTFE is not hard enough to scratch the steel substrate, such abrasion may be traced back to the direct action of TMCC particles. When using a steel ball as a CB, however, the initial TMCC powders were immediately removed, and deep abrasion marks covered the entire wear track (**Figure 5.4f**). Moreover, the accumulation of debris at the reversal points

and around the entire perimeter confirms the occurrence of pronounced abrasive processes, typical of a steel-steel contact. This evidence could explain the trend observed in **Figure 5.4c**, where the COF starts very low (~ 0.2) and increased to the reference value after few initial cycles, coinciding with the removal of the TMCC powders from the tribological contact. The observations made for the wear behavior and the trend of the friction values strongly indicate that the adhesion of the $\text{Ta}_2\text{S}_2\text{C}$ powder to the steel CB is much lower compared to the ceramic CBs, resulting in a significant reduction in the wear life of the tribofilm. Moreover, the morphology of the TMCC-based tribofilm seems to be affected by the Hertzian contact pressure induced by the paired material, i.e., 0.45 GPa for Al_2O_3 , 0.48 GPa for SiC, 0.40 GPa for 100Cr6 and only 0.012 GPa for the PTFE CBs.

5.3.3 Tribofilm characterization

To further confirm the formation of TMCC tribofilms and to understand the underlying tribological mechanisms we carried out multiple analyses of the substrate surfaces after sliding. To provide a complete picture in terms of both chemical composition and structural features, in the following paragraphs we report the results from SEM-EDS, XPS, AMES, and TEM. As the most promising results were obtained during sliding against an Al_2O_3 counterbody, we focused the analysis on this tribo-pair.

Wear track analysis by SEM-EDS, XPS and AMES.

Elemental map overlays by EDS inside the AMES system provide more information about the distribution of the elements inside the tribofilms (**Figure 5.5**). The SEM images and the elemental mappings of the EDS analysis clearly show the formation of a patchy tribofilm for both $\text{Nb}_2\text{S}_2\text{C}$ and $\text{Ta}_2\text{S}_2\text{C}$. Also, the tribofilms are basically composed of compacted flake-like particles similar in size to the original powder. Indeed, the overlaid elemental mappings for $\text{Nb}_2\text{S}_2\text{C}$ (**Figure 5.5a**) and $\text{Ta}_2\text{S}_2\text{C}$ (**Figure 5.5b**) verify that the patches inside the tribofilms were mainly composed of Nb/Ta and S, with only minor contributions of oxygen. Outside the wear tracks the iron signal from the steel substrate prevails, while no iron can be detected through the tribofilm (**Figure 5.5c-d**). Interestingly, the Fe signal in the EDS mapping was quite intense for the as-synthesized TMCCs (**Figure 5.2a**), but it was not detected in the tribofilm after the sliding experiment. This suggests that the residual Fe may be loosely bonded to the TMCCs and therefore easily removed during friction.

These results conclude that the TMCCs added to the contact area as powders were compressed to form a relatively thick tribofilm, whose functionality did not rely on any specific tribochemical reactions. The fact that no significant oxygen and iron contributions appeared in the EDS measurements inside the tribofilm underscores the stability of the TMCC particles and suggests that a protecting tribofilm was formed preventing tribochemical wear of the substrate.

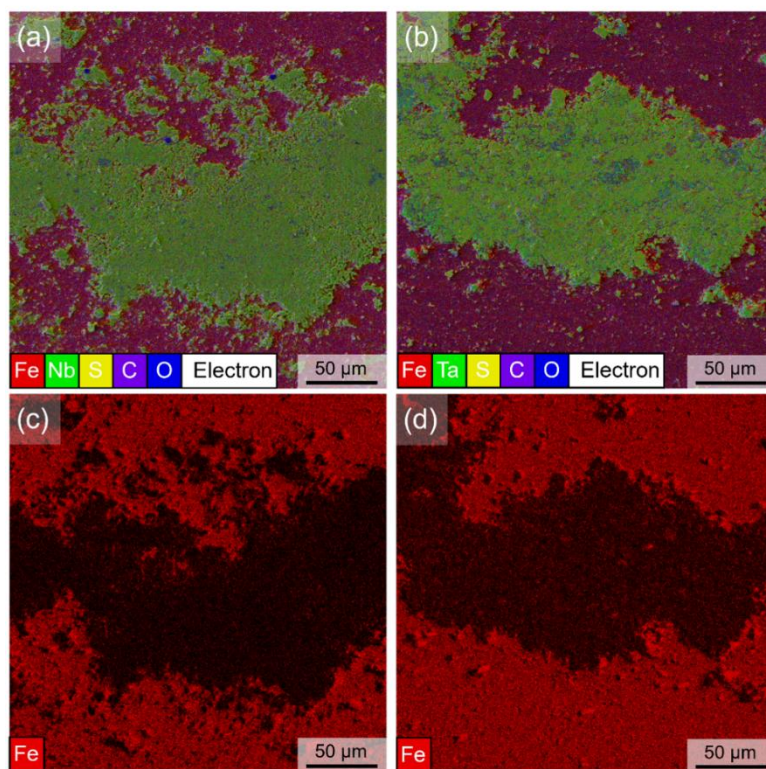


Figure 5.5: SEM-EDS elemental map overlays (Fe, Nb/Ta, S, O, C) of tribofilms for Nb₂S₂C (a) and Ta₂S₂C (b). Elemental map of Fe to show the coverage of the tribofilm on Nb₂S₂C (c) and Ta₂S₂C (d).

Further chemical analysis was performed by XPS and AMES to characterize the chemistry of the wear tracks in detail, specifically capturing the surface chemistry and the chemical bonding environments. XPS spectra with the corresponding deconvolution fits for the Nb3d (Ta4f), S2p, C1s and O1s peak areas are shown in **Figure 5.6** for (a) Nb₂S₂C and (b) Ta₂S₂C. Nb3d (Ta4f) regions confirm the presence of TMCCs inside the tribofilm, since we observed the presence of doublets centered at 202.8 eV (23.7 eV) in accordance with S-Nb-C (S-Ta-C) chemical bonds.⁴⁰ Moreover, the TMCC presence is also highlighted by peaks centered around 160.8 eV in the S2p region and at 284.3 eV inside the C1s region, all related to the S-Nb(Ta)-C bond. It is also worth noting a doublet connecting with metallic tantalum (22.2 and 24.2 eV inside the Ta4f region), that was also reported in Ref.⁴⁰ from the XPS analysis on the delaminated TMCCs. The presence of Ta(0) signal in Ta₂S₂C is not clear. It may be connected with the presence of unreacted Ta and TaC from the TMCC synthesis (as observed in **Figure 5.2**) and/or it may be related to surface defects and damage caused by ion-sputtering. Inside the sulfur region, chemical states involving oxygen are also clearly visible (peak located at 162.3 eV related to SO_x and a small contribution of sulphates around 168.3 eV). Similarly, inside the O1s region we detected the presence of metal oxides (529.7 eV) and carbon-oxygen bonds (531.3 eV). Together with the peaks of C-Nb(Ta)-S at 284.3 eV, the C1s signals reveal four additional components: adventitious carbon (285 eV), C-O (286.4 eV) and C=O (288.2 eV), as well as small amounts of carbide (282.3 eV). Interestingly, almost negligible oxygen

signal was observed in the SEM-EDS mapping, whereas from XPS analysis, whose depth typically reaches only up to 7-10 nm, oxygen bonding environments are evidenced. Therefore, we can assume that oxidation is limited exclusively to the near-surface region of the particles. The presence of oxides from XPS analysis may suggest that oxidative reactions happened during rubbing, although traces of native oxides can be observed even without tribological testing.⁴⁰ Since the experiments were conducted in air environment, rich in O₂, it is reasonable to believe that oxide layers are repeatedly removed and re-formed.

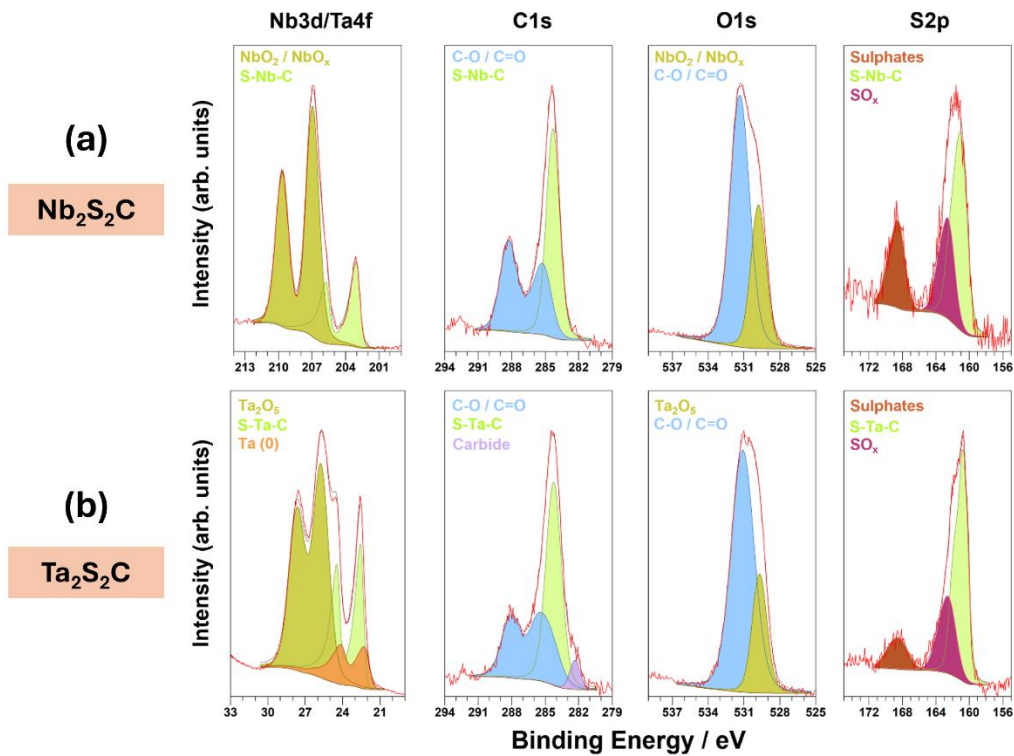


Figure 5.6: XPS of the Nb3d/Ta4f, C1, O1s and S2p regions of tribofilms Nb₂S₂C (a) and Ta₂S₂C (b) after surface cleaning. Intensity scales are normalized to the maximum signal for each of the elements. Color code: light green S-Nb-Ta-C, olive (metal oxide), blue (C, O-contamination), magenta (SO_x), dark orange (sulphates), violet (carbide).

AMES results are included in **Figure 5.7** for (a) Nb₂S₂C and (b) Ta₂S₂C. All the expected elements (Nb, Ta, S, C) were detected, confirming once again the presence of TMCC inside the tribofilm. The oxygen contribution was almost negligible, while the iron signal originated from the underlying steel substrate. Both XPS and AMES/EDS confirm the presence of the expected elements in compacted tribofilms with a thickness of at least 1 μm (deduced from the absence of the iron signal from underneath the tribo track in EDS). The bonding environments found in powder TMCC samples can also be detected in the tribofilms, which allows us to assume that most of the TMCC remains stable. However, small changes are found when compared to Ref.²² in increased amounts Nb/Ta/S oxide and the formation of small amounts of sulphates and carbides on the particle surface.

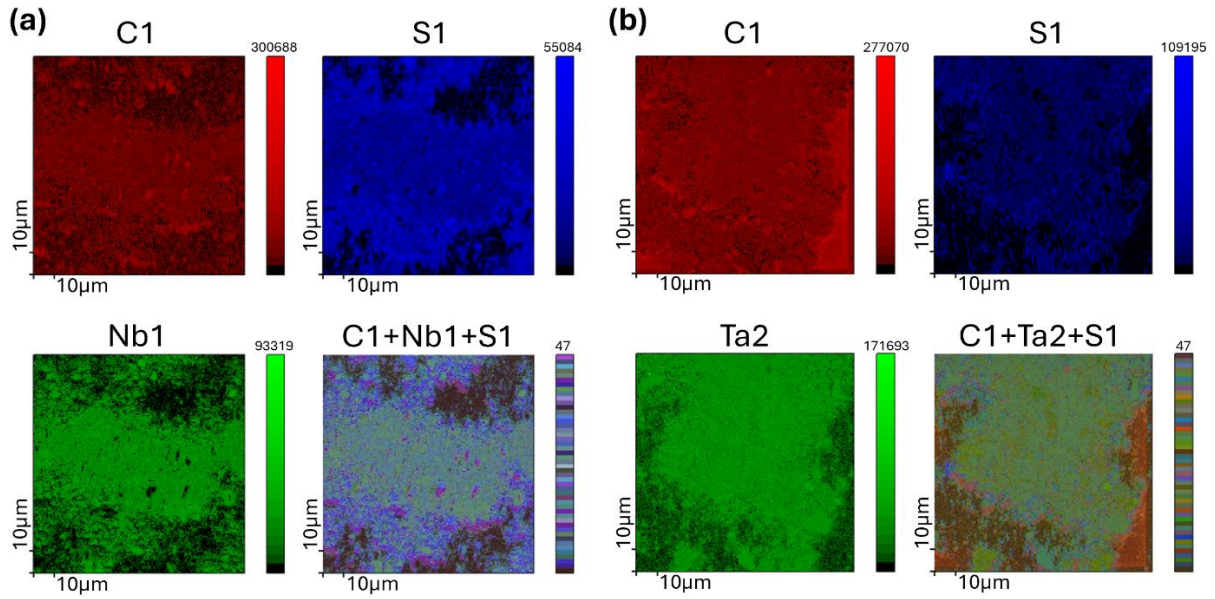


Figure 5.7: AMES maps and red-green-blue (RGB) map overlays of tribofilms (a) $\text{Nb}_2\text{S}_2\text{C}$ and (b) $\text{Ta}_2\text{S}_2\text{C}$. Intensity scales are normalized to the maximum signal for each of the elements.

Wear track analysis by TEM.

To gain structural and morphological insights into the tribofilm after the friction experiments, we first prepared a FIB cross-section in a representative wear track and performed TEM analysis on it afterwards. The FIB cut on a $\text{Nb}_2\text{S}_2\text{C}$ -based TMCC tribofilm was done on a specific area (**Figure 5.8a**), so that both loose and compacted parts of the tribofilm were included inside the same TEM-lamella (**Figure 5.8b-c**). The cross-sectional view of the compacted tribofilm area (**Figure 5.8d**) reveals a flat tribofilm with a homogeneous thickness of about 1 μm . The voids observed are mainly generated by the thinning process during FIB processing, since originally the tribofilm appeared fully dense consisting of TMCC particles of different sizes, including micron sized large TMCC particles with a low degree of wear, as well as powders that have been frictionally ground down to the nanoscale. Selected area electron diffraction (SAED) in **Figure 5.8e-g** highlights that the large micro-sized TMCC particles have a crystalline structure, while the smaller-sized particles exhibit mainly nanocrystalline and amorphous phase diffraction patterns. The $\text{Nb}_2\text{S}_2\text{C}$ presence is clearly confirmed by the subsequent EDS mapping (**Figure 5.8h**), where Nb, S, C, and O are detected. Interestingly, no significant oxidation occurred inside the larger TMCC particles, while the oxygen signal is more intense for those areas surrounding the particle surface. This is in accordance with the assumption that tribochemical reactions are more pronounced at the locations with more wear.

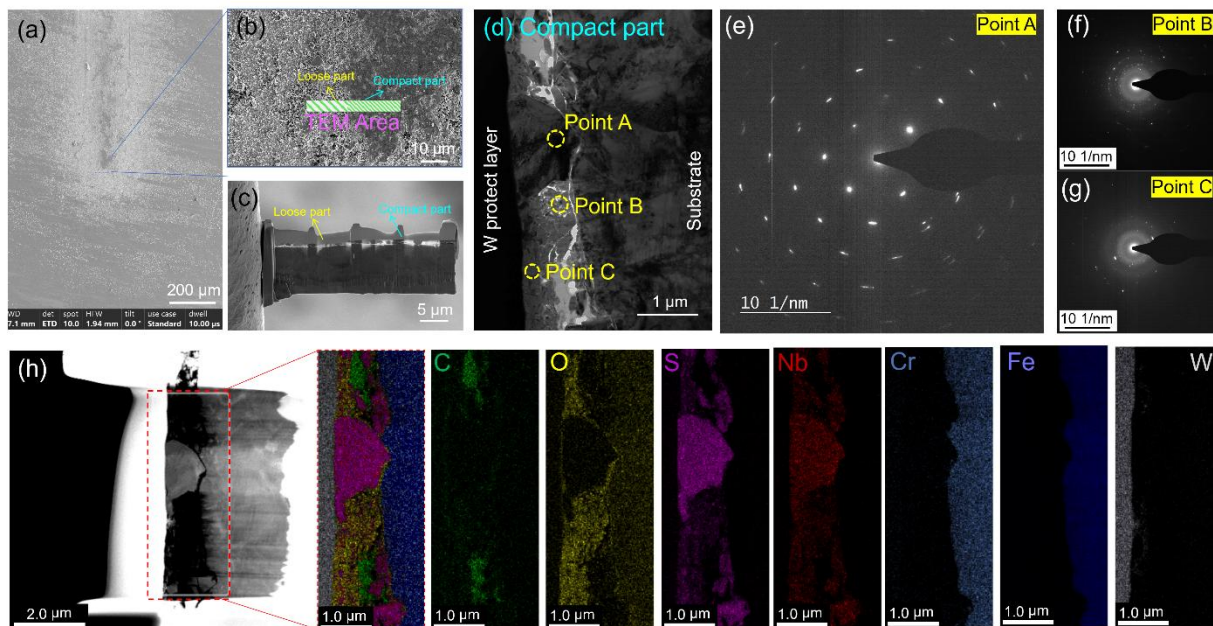


Figure 5.8: TEM results for Nb₂S₂C powder after sliding: (a)-(c) FIB lamella preparation, (d) cross-sectional morphology of the compacted part of the tribofilm inside the wear track, (e)-(g) corresponding SAED patterns at different positions, and (h) EDS mapping results.

The high-resolution TEM morphology of the tribofilm is reported in **Figure 5.9**. In the region close to the surface of the tribofilm, the TMCC layers show a distribution trend parallel to the surface (**Figure 5.9c-d**). The measured interlayer distance is about 0.88 nm, which connects well with the (001) Nb₂S₂C crystal plane. These 2D TMCC planes are the ones with weak interacting forces and, therefore, they are the ones supposed to accommodate interlayer sliding. Such evidence can explain the excellent tribological performance observed for the TMCC powder. In addition, **Figure 5.9e-h** shows high-resolution images of some small particles inside the tribofilm, highlighting the presence of an amorphous phase embedding these particles. From the TEM-EDS results of **Figure 5.8**, it seems that such amorphous phase is composed of oxides, most likely originating from the particle's surface during the tribological process and pressed together with unoxidized Nb₂S₂C layers. The high-resolution image of TMCC small particles (**Figure 5.9g**) reveals a crystalline interior where the (001) and (012) crystal planes are clearly visible (**Figure 5.9h**). The interlayer distances measured based on HR-TEM are almost identical to the simulated values for Nb₂S₂C (inset in **Figure 5.9h**).

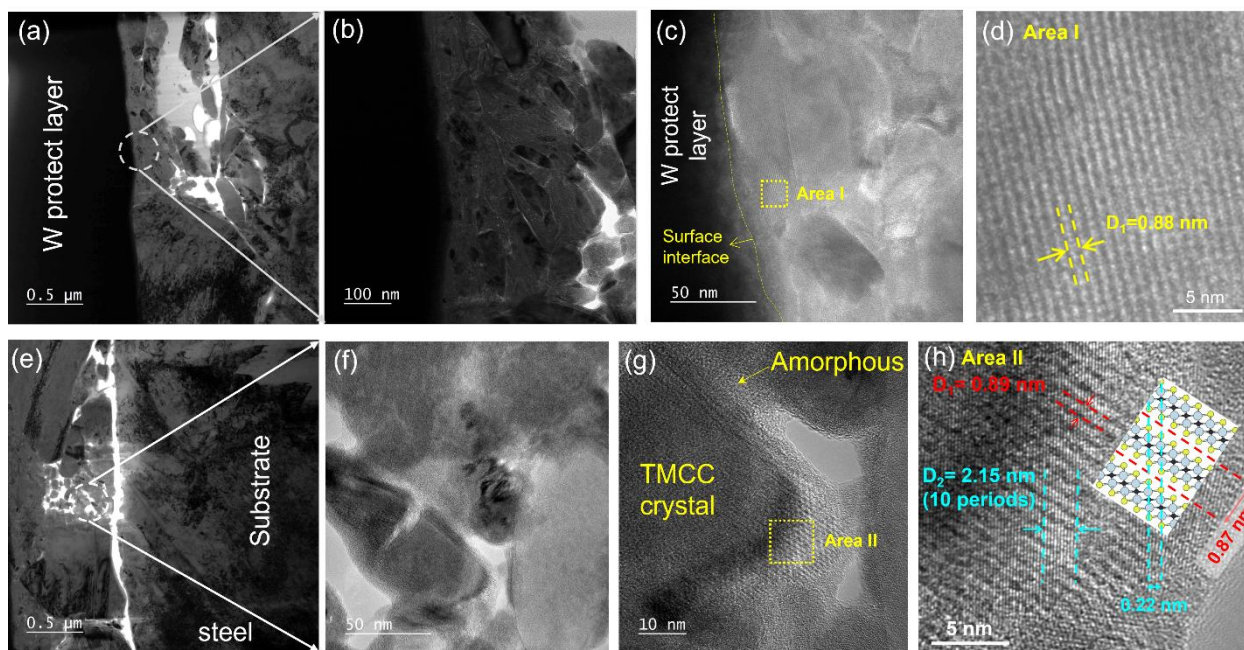


Figure 5.9: TEM results for $\text{Nb}_2\text{S}_2\text{C}$ powder after sliding: (a-b) TEM images of the near-surface region of the wear track and (c-d) corresponding high-resolution TEM images of the TMCC particle near the surface. TEM images of the region close to the substrate (e-f) and corresponding (g-h) high-resolution TEM images of the small TMCC particles. The inset inside panel (h) shows the crystal structure of $\text{Nb}_2\text{S}_2\text{C}$ simulated in this work, as well as the observed interplanar distances.

These results confirm that the tribofilm is mainly composed of unoxidized TMCC crystalline nanoparticles, embedded in an oxide-based amorphous matrix. Compared with TMD materials, TMCCs seem to have higher thermal and chemical stability, which may be traced back to the strong Nb-C bonds. Because they are more chemically inert, oxidative processes are limited to the outermost TMCC layers. However, the presence of an oxidic phase inside the tribofilm is not necessarily negative, as it may help prevent the rapid exfoliation of TMCCs flakes. More studies are needed to investigate the role of oxides, whether they are also lubricious or have a mere retention function.

5.3.4 Interlayer sliding by DFT simulations

TEM-EDS analysis confirms the presence of intact and crystalline 2D TMCC layers within the effective tribofilm. Supported by this experimental evidence, we carried out numerical DFT calculations to model the interlayer sliding for $\text{Nb}_2\text{S}_2\text{C}$ and $\text{Ta}_2\text{S}_2\text{C}$ bilayers, exploring their easy-to-shear properties from a nanoscale perspective. The amount of energy required to separate two layers, i.e., the work of separation (W_{SEP}), and the potential corrugation values (ΔW_{SEP}) are listed in **Table 5.1**. These two quantities represent a good predictor for the lubricating ability of materials,^{105,248} since they correlate with the shear strength.¹¹² In addition to $\text{Nb}_2\text{S}_2\text{C}$ and $\text{Ta}_2\text{S}_2\text{C}$, we also provide a comparison with well-established solid lubricants, i.e., MoS_2 , graphene, WS_2 and Ti_2CT_x ($T = \text{F}_{1/3}$, $\text{O}_{1/3}$, $\text{OH}_{1/3}$). The low W_{SEP} and ΔW_{SEP} values

observed for Nb₂S₂C and Ta₂S₂C connect well with the vdW nature of their interlayer interactions. Ta₂S₂C (0.33 J/m²) shows a slightly higher binding energy than Nb₂S₂C (0.24 J/m²), since electronic correlation effects are more pronounced for Ta than Nb, leading to stronger vdW interactions. However, the maximum energetic barriers experienced during mutual sliding are almost the same for the two TMCCs ($\Delta W_{\text{SEP}} = 0.08\text{-}0.10$ J/m²), being in the range observed for graphene, MoS₂ and WS₂.¹¹¹ The comparison between TMCCs and titanium-based MXenes (Ti₂CT_x) strictly depends on the termination types of MXene (T), which are known to be poorly controllable when following a top-down HF etching approach.¹³¹ As broadly documented in chapter 2, MXene layers with mixed terminations have a significant interlayer adhesion (0.52 J/m²), due to the formation of hydrogen bonds and dipole-dipole interactions between layers, making them more adhesive to each other and reducing the interlayer slipperiness. Nb₂S₂C and Ta₂S₂C layers, conversely, only expose to the interface homogeneous sulfur terminations, leading to pure vdW forces acting between the layers and hence low interlayer adhesion. Although MoS₂ and WS₂ layers are also passivated by sulfur atoms, Nb₂S₂C and Ta₂S₂C exhibit lower ΔW_{SEP} values, suggesting better performance for TMCCs, at least in principle. It is important to note that DFT calculations presented here serve as an ideal predictive tool and do not account for other potentially significant factors acting at the micro- and macro-scales (surface roughness, grain boundaries).

Table 5.1. Work of separation (W_{SEP}), and the potential energy surface corrugation (ΔW_{SEP}) for a selected list of 2D materials.

2D-bilayer	W_{SEP} (J/m ²)	ΔW_{SEP} (J/m ²)
Nb ₂ S ₂ C	0.24	0.08
Ta ₂ S ₂ C	0.33	0.10
Graphene	(0.25) ^a	(0.06) ^a
	(0.26) ^b	(0.08) ^b
MoS ₂	(0.26) ^a	(0.12) ^a
	(0.27) ^b	(0.10) ^b
WS ₂	0.29	0.12
Ti ₂ CT _x (T = F _{1/3} , O _{1/3} , OH _{1/3})	(0.52) ^a	(0.46) ^a

^aRef.⁹¹

^bRef.¹¹¹

To further confirm the lubrication ability of TMCCs, in **Figure 5.10** we report the potential energy surface (PES) for Nb₂S₂C and Ta₂S₂C bilayers as a function of the external load applied (from 0 to 5 GPa). Since a PES describes the interlayer interaction between two surfaces as a function of their relative lateral position, it provides precise information about the energetic barriers experienced during mutual sliding, or in other words, about the amount of energy that can be dissipated by frictional processes. Both Nb₂S₂C and Ta₂S₂C show hexagonal crystal structure with similar *a* lattice parameter (3.284 Å and 3.268 Å, respectively, in very good agreement with Ref.⁴⁰) and the same most favorable stackings (labeled ‘min 1’ and ‘min 2’ in

Figure 5.10). The minimum energy path (MEP, i.e., the most favorable sliding path during reciprocal sliding) is highlighted with a yellow dashed line, while the corresponding energy profile is reported on the right side of **Figure 5.10**. The energy barriers faced during interlayer sliding along the MEP are surprisingly low, with almost no difference between Nb₂S₂C and Ta₂S₂C. Indeed, for applied normal loads ranging from 0 to 5 GPa the maximum energy barrier never exceeded 0.05 J/m². Such numerical results are in perfect agreement with our experimental findings as they confirm the easy-to-shear ability of TMCCs. Moreover, they predict a similar lubricant behavior between Nb₂S₂C and Ta₂S₂C, which has also been observed in our experiments whenever the TMCC-based tribofilm was formed.

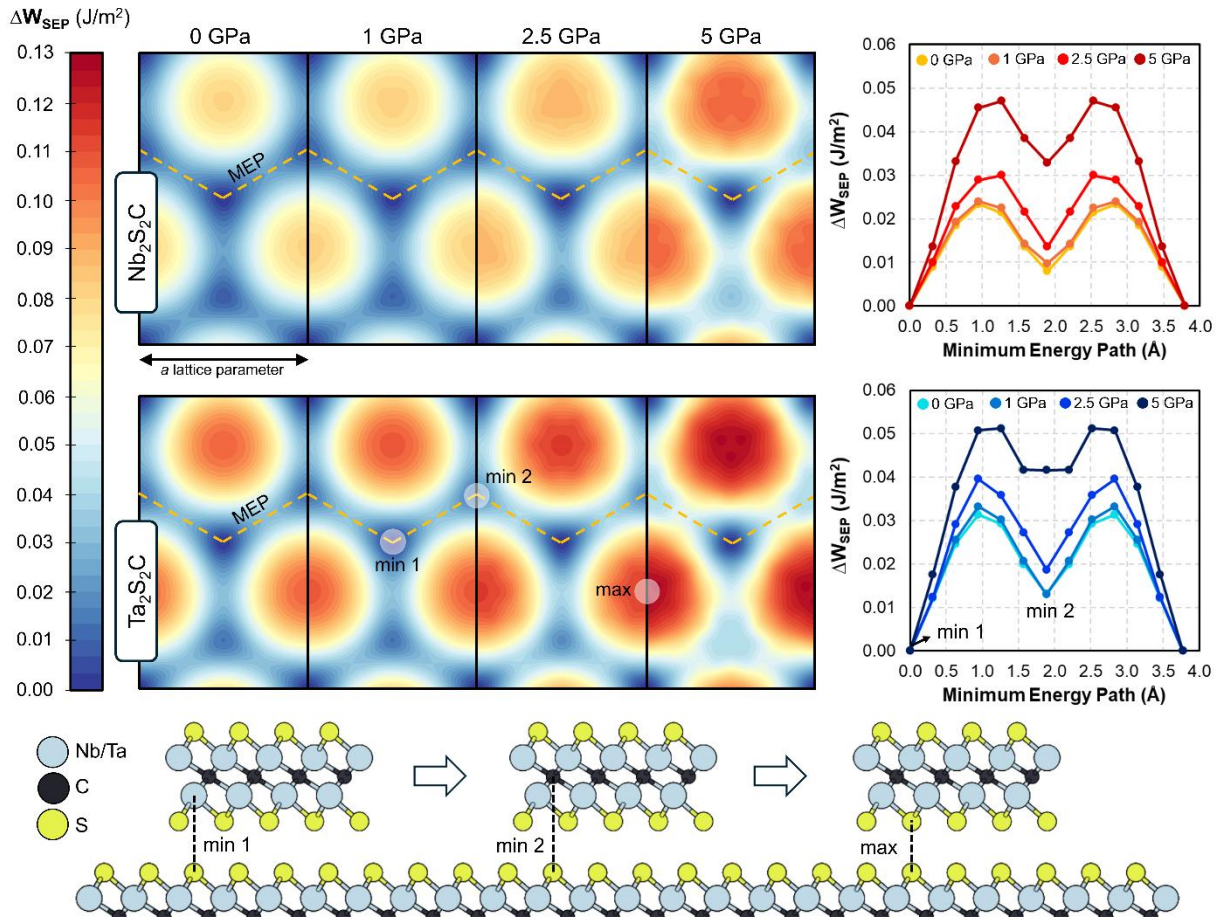


Figure 5.10: Potential energy surfaces (PES) for bilayers of Nb₂S₂C (above) and Ta₂S₂C (below) from 0 to 5 GPa load. The minimum energy path (MEP) is highlighted by a yellow dashed line, with the corresponding energy profile depicted on the right. Schematics on the relevant lateral configurations (min1, min2 and max) are shown below the PESes.

5.4 Conclusions

We have widely discussed the tribological performance of TMCC powders in both reducing the COF and preventing wear. No complicated coating process had to be applied, but rather the TMCCs were simply added to the contact area as powders, and the results were still impressive. The exceptional tribological performance can be traced back to the ability of TMCCs to form an adhesive and protective tribofilm, with the layers oriented in parallel to the

surface. Once the TMCC-based tribofilm is formed, the 2D nature of the Nb₂S₂C/Ta₂S₂C flakes ensures easy shearing, thus leading to low friction.

In **Figure 5.11** we report the results obtained for WS₂ and Ti₃C₂T_x MXene as-deposited powders under the same tribological conditions as described before for Nb₂S₂C and Ta₂S₂C TMCCs against Al₂O₃ counterbody (i.e., Hertzian contact pressure of 0.45 GPa, stroke length of 1 mm and sliding velocity of 1 mm/s).

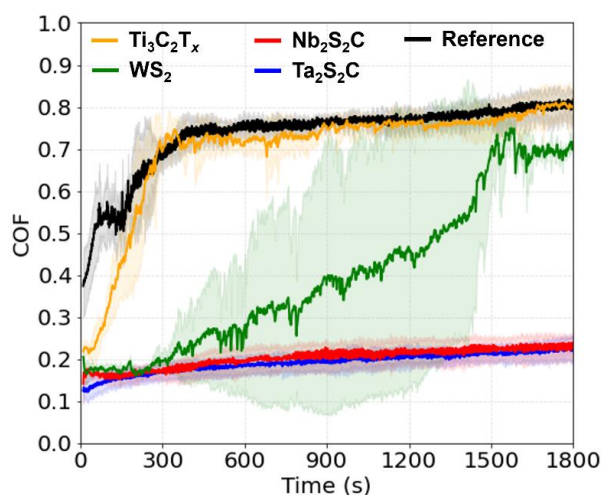


Figure 5.11: Tribological performance of Nb₂S₂C (red line) and Ta₂S₂C (blue) TMCCs compared with tungsten disulfide (WS₂, green) and MXene (Ti₃C₂T_x, yellow) powders, against Al₂O₃ counterbody.

Figure 5.11 clearly indicates that Nb₂S₂C and Ta₂S₂C outperform WS₂ and Ti₃C₂T_x powders in terms of frictional performance. It is worth mentioning that WS₂ and Ti₃C₂T_x are usually not tested as powders, instead they are commonly applied as coatings to optimize their performance. However, the resulting COFs are close to earlier observed values when WS₂ or Ti₃C₂T_x are applied as coatings and tested under similar conditions.^{85,201,249} In the first few minutes, the WS₂ powder could efficiently lubricate the tribological contact, leading to COF similar to the TMCCs. The standard deviation (e.g., highlighted by the faded area in the diagram) reaches even values well below the limit of 0.2 observed for TMCCs. However, after a while the WS₂ powders were rapidly removed from the contact, with the effect that the COF reached the reference value. Instead, Ti₃C₂T_x powder was completely dislodged from the wear track from the very beginning of the experiments, being indicative of low adhesion to the sliding surfaces. These comparative results highlight the importance for 2D materials of establishing a good adhesion to the substrate, so as to resist the peeling-off during rubbing. Further benchmarking and comparisons with other Niobium- and Tantalum-based TMDs (NbS₂ and TaS₂) or MXenes are expected to enhance the understanding of TMCCs' potential usage as lubricants.

To conclude, this chapter extensively discussed the tribological behavior of 2D layered TMCCs (Ta₂S₂C and Nb₂S₂C) when applied as powders onto steel substrates (AISI304),

investigating the effect of different counterbody materials (Al_2O_3 , SiC, PTFE, and AISI304 steel) in a ball-on-disk setup under ambient air. In most cases, the presence of $\text{Ta}_2\text{S}_2\text{C}$ and $\text{Nb}_2\text{S}_2\text{C}$ at the contact interface proved to be beneficial for lubrication, significantly outperforming traditional 2D materials such as WS_2 and MXenes. This was primarily due to the rapid formation of a patchy tribofilm composed of compacted TMCC powder, which protected the tribo-pair from excessive wear and ensured a stable and low coefficient of friction ($\text{COF} < 0.2$). For the PTFE counterbody, which has a much lower elastic modulus, a less compacted but still effective tribofilm was observed, maintaining the same COF trend. In contrast, with the steel counterbody, the TMCC powder was completely removed from the substrate after a few cycles, leaving the contact unlubricated. We concluded that strong adhesion of TMCC particles to the counterbody and sufficient contact pressure are necessary for the formation of a beneficial tribofilm, as observed with the Al_2O_3 and SiC ceramic counterbodies.

SEM-EDS measurements of the wear tracks revealed that the tribofilms were not continuous but consisted of patches of compacted TMCC particles (with Nb/Ta, S, and C signals). XPS and AMES analysis of the near-surface region confirmed the expected binding environments (S-Nb/Ta-C) and elemental composition (Nb/Ta, S, C) for TMCCs. TEM-EDS imaging, combined with SAED, showed that TMCC particles compacted within the tribofilm had a range of sizes, from large micro-sized crystalline particles to smaller nanocrystalline particles embedded in an amorphous oxide phase. While SEM-EDS mapping indicated only minimal oxygen content, XPS analysis, by probing a depth of 7-10 nm, revealed oxygen-related bonding environments (SO_x , sulfates, metal oxides, C-O, C=O).

Based on these results, we inferred that while oxidative processes occur near the surface, the functionality of the tribofilm does not rely on significant tribochemical transformations but rather on the layered structure of TMCCs, which promotes easy interlayer shearing. Indeed, high-resolution TEM images of the near-surface region revealed the presence of TMCC flakes oriented parallel to the sliding surface. This experimental evidence was further supported by comparative DFT simulations, which demonstrated low energy barriers for interlayer sliding of TMCCs, confirming their potential as efficient solid lubricants.

These findings pave the way for further studies involving more advanced deposition techniques (e.g., air-spraying, electro-spraying) and various tribological testing setups under different environmental conditions (e.g., nitrogen or vacuum). It is important to note that the samples tested contained secondary phases, such as rock-salt carbides and MAX phases, which have strong bonding in all directions and lack the weak out-of-plane forces characteristic of TMCCs. Therefore, it is reasonable to predict even better lubricity with purer samples. Future research on TMCCs should focus on enhancing the purity of the TMCC phases. The presented results serve as a foundation for introducing TMCCs to the materials science and tribology communities, offering possibilities for more durable, efficient, and sustainable solid lubricants.

Chapter 6

6. Final remarks and future perspectives

In this thesis, computational simulations have been combined with experimental techniques to investigate the tribological properties of 2D materials, with a focus on TMDs, MXenes, TMCCs, and their composites. All computational results were obtained through Density Functional Theory (DFT) atomistic simulations, which allowed for an accurate description of interlayer interactions in 2D materials, as well as their chemical reactivity under mechanical stress. The chosen methodology (PBE+D2_{NG}) was carefully optimized to handle van der Waals interactions efficiently, delivering both precision and computational economy.

In Chapter 2, we demonstrated by DFT atomistic simulations that titanium-based MXenes possess excellent potential as solid lubricants, particularly in terms of interlayer slipperiness and substrate adhesion. Our results showed that surface terminations (–F, –O, –OH) significantly affect lubrication performance, more than monolayer thickness or C/N ratio. Hydroxyl-terminated surfaces offer higher interlayer adhesion and stronger interactions with substrates like iron and iron oxide. Conversely, –F terminations reduce interlayer binding but weaken adhesion to ferrous substrates, promoting exfoliation during sliding. MXenes with –O termination exhibited the best overall performance, adhering well to ferrous surfaces and performing comparably to graphene and MoS₂. We also explored MXene hydrophilicity by mapping defect-free surfaces, mono- and poly-defected surfaces, as well as edges. Water chemisorption was observed on surfaces with single termination vacancies, edges, and defect clusters. Notably, exposed unsaturated Ti atoms allowed the oxygen in H₂O molecules to chemisorb, with higher energy gains observed on vacancy clusters (1.00-1.80 eV) compared to edges (0.75-0.85 eV) and termination vacancies (0.60-1.20 eV).

In Chapter 3, we discussed the synergistic effects observed in MXene/MoS₂ composite coatings, which outperform the pure materials in terms of adhesion and lubrication. DFT simulations provided insights into the tribological performance of the MXene/MoS₂ hybrid interface, complementing experimental results. Under harsh conditions, such as 0.8 GPa contact pressure, two Ti₃C₂T_x/MoS₂ hybrid coatings (random mixture and sandwich-like) were tested in dry sliding tests. We demonstrated the formation of a stable tribofilm that significantly reduced wear and lowered friction, with a steady COF of around 0.15 throughout the test. These findings highlight the potential of MXene-based composites for unlocking multiple synergistic effects, from enhanced resistance to specific environments to improved load-carrying capacity.

Chapter 4 introduced an innovative method for generating MoSe₂- and WSe₂-based tribofilms from selenium nano-powders during the reciprocating sliding of Mo- and W-coated

surfaces. The *in operando* formation of these TMD layers within the contact zone substantially reduced friction and wear, with the addition of Se nano-powders ensuring repeatability and reproducibility. *Ab initio* molecular dynamics (AIMD) revealed the shear-driven reaction mechanisms responsible for TMD layer formation, emphasizing the role of metallic debris in catalyzing the tribochemical reaction between metal and selenium. This approach holds promise for applications in vacuum environments where traditional lubricants are unsuitable or in maintenance-critical settings where TMD coatings fail once fully worn.

In Chapter 5, we provided an initial investigation into the lubricating capabilities of TMCCs, specifically Nb₂S₂C and Ta₂S₂C multilayer powders. Tribological testing against different counterbody materials demonstrated their potential as solid lubricants under ambient conditions. The best performance was observed in steel vs. Al₂O₃ contacts (0.45 GPa), where TMCC powders formed a protective tribofilm with parallel-oriented layers. Once the tribofilm formed, the 2D nature of the Nb₂S₂C/Ta₂S₂C flakes enabled easy shearing, as evidenced by TEM imaging and DFT simulations. The ability of TMCCs to reduce wear and friction was superior to that of WS₂ and Ti₃C₂T_x MXenes under similar conditions. These results represent a foundational step toward unlocking the tribological potential of TMCCs in the materials science and tribology fields.

In conclusion, the results presented in this thesis underline the viability of 2D materials for tribological applications. Their effectiveness is rooted in their layered structure, which makes the covered surfaces inert, facilitating the easy shearing, combined with their high compressive strength. Whether we consider transition metal dichalcogenides (TMDs), transition metal carbides/nitrides (MXenes), or transition metal carbo-chalcogenides (TMCCs), as well as their composites, such as Ti₃C₂T_x/MoS₂, all exhibit remarkable potential as solid lubricants, capable of outperforming conventional oils and greases. TMDs are already used in various applications, particularly in space lubrication.^{250,251} However, further optimization is required, especially through composite coatings, representing an exciting frontier. MXenes, though a more recent discovery, are rapidly gaining attention, with new advancements emerging every day.⁸² Addressing environmental stability issues, particularly oxidation, while exploring biodegradable or non-toxic synthesis methods, will be crucial for future developments. Although Ti₃C₂T_x has been extensively studied, the broader family of MXenes remains underexplored in tribological contexts. In fact, we can say that research on MXenes for tribology is still in its infancy. As for TMCCs, their potential is even less studied, with the results presented in this thesis representing only the first step in a much longer journey. Future work will involve testing TMCCs using advanced deposition techniques (e.g., air-spraying, electro-spraying) and exploring their performance in different environments (e.g., nitrogen or vacuum).

Each of these families of 2D materials offers unique advantages in terms of load-carrying capacity, temperature stability, and resistance to harsh environments. Defining these ranges is crucial for expanding our understanding of their properties, thus systematic studies play a

key role in advancing the knowledge of 2D materials for solid lubrication. Additionally, computational simulations represent predictive and explanatory tools that guide the design and optimization of these materials. It is essential not only to conduct systematic laboratory experiments but also to explain the underlying mechanisms, establishing clear cause-effect relationships. In this regard, the integration of machine learning techniques with atomistic simulations could accelerate the discovery of new 2D materials with optimized tribological properties.

Bibliography

- (1) Blau, P. J. *Friction Science and Technology: From Concepts to Applications*, 2nd ed.; CRC Press, 2008.
- (2) Williams, J. The Invention of Tribology: Peter Jost's Contribution. *Lubricants* **2024**, *12*, 65.
- (3) Holmberg, K.; Erdemir, A. The Impact of Tribology on Energy Use and CO₂ Emission Globally and in Combustion Engine and Electric Cars. *Tribol. Int.* **2019**, *135*, 389–396.
- (4) Holmberg, K.; Erdemir, A. Global Impact of Friction on Energy Consumption, Economy and Environment. *FME Trans.* **2015**, *43*, 181–185.
- (5) Reynolds, O. On the Theory of Lubrication and Its Application to Mr. Beauchamp Tower's Experiments, Including an Experimental Determination of the Viscosity of Olive Oil. *Philos. Trans. R. Soc. London* **1886**, *177*, 157–234.
- (6) Stribeck, R. *Kugellager Für Beliebige Belastungen*; Springer, 1901.
- (7) Stribeck, R. *Die Wesentlichen Eigenschaften Der Gleit- Und Rollenlager*; Springer, 1903.
- (8) Bowden, F. P.; Tabor, D. *The Friction and Lubrication of Solids*; Clarendon Press, 2001.
- (9) Tabor, D.; Winterton, R. H. S. The Direct Measurement of Normal and Retarded van Der Waals Forces. **1969**, *312*, 435–450.
- (10) Carpick, R. W.; Salmeron, M. Scratching the Surface : Fundamental Investigations of Tribology with Atomic Force Microscopy. **1997**, *97*, 1163–1194.
- (11) Phillips M. R.; Dewey M.; Hall D. D.; Quinn T. F. J.; Southworth H. N. The Application of Auger Electron Spectroscopy to Tribology. *Vacuum* **1976**, *26*, 451–456.
- (12) Atkinson, S. J.; Brundle, C. R.; Roberts, M. W. Ultra-Violet and X-Ray Photoelectron Spectroscopy (UPS and XPS) of CO, CO₂, O₂ and H₂O on Molybdenum and Gold Films. *Faraday Discuss. Chem. Soc.* **1974**, *58*, 62–79.
- (13) Hirano, M.; Shinjo, K. Atomistic Locking and Friction. *Phys. Rev. B* **1990**, *41*, 11837–11851.
- (14) Vakis, A. I.; Yastrebov, V. A.; Scheibert, J.; Nicola, L.; Dini, D.; Minfray, C.; Almqvist, A.; Paggi, M.; Lee, S.; Limbert, G.; Molinari, J. F.; Anciaux, G.; Aghababaei, R.; Restrepo, S. E.; Papangelo, A.; Cammarata, A.; Nicolini, P.; Putignano, C.; Carbone, G.; Stupkiewicz, S.; Lengiewicz, J.; Costagliola, G.; Bosia, F.; Guarino, R. Modeling and Simulation in Tribology across Scales : An Overview. *Tribol. Int.* **2018**, *125*, 169–199.
- (15) Nyholm, N.; Espallargas, N. Functionalized Carbon Nanostructures as Lubricant Additives – A Review. *Carbon N. Y.* **2023**, *201*, 1200–1228.
- (16) Gong, H.; Yu, C.; Zhang, L.; Xie, G.; Guo, D.; Luo, J. Intelligent Lubricating Materials: A Review. *Compos. Part B Eng.* **2020**, *202*, 108450.
- (17) Zhang, Z. Z.; Liu, W. M.; Xue, Q. J. Effects of Various Kinds of Fillers on the Tribological Behavior of Polytetrafluoroethylene Composites under Dry and Oil-Lubricated Conditions. *J. Appl. Polym. Sci.* **2001**, *80*, 1891–1897.
- (18) Rosenkranz, A.; Liu, Y.; Yang, L.; Chen, L. *2D Nano-Materials beyond Graphene: From Synthesis to Tribological Studies*; Springer International Publishing, 2020; Vol. 10.
- (19) Spikes, H. Friction Modifier Additives. *Tribol. Lett.* **2015**, *60*, 1–26.
- (20) Xia, D.; Wang, Y.; Liu, H.; Yan, J.; Lin, H.; Han, S. Research Progress of Antioxidant Additives for Lubricating Oils. *Lubricants* **2024**, *12*.
- (21) Martini, A.; Ramasamy, U. S.; Len, M. Review of Viscosity Modifier Lubricant Additives. *Tribol. Lett.* **2018**,

66, 1–14.

- (22) Spikes, H. The History and Mechanisms of ZDDP. *Tribol. Lett.* **2004**, *17*, 469–489.
- (23) Kosarieh, S.; Morina, A.; Lainé, E.; Flemming, J.; Neville, A. The Effect of MoDTC-Type Friction Modifier on the Wear Performance of a Hydrogenated DLC Coating. *Wear* **2013**, *302*, 890–898.
- (24) Grossiord, C.; Varlot, K.; Martin, J.; Mogne, T. Le; Esnouf, C. MoS₂ Single Sheet Lubrication by Molybdenum. *Tribol. Int.* **1999**, *31*, 737–743.
- (25) Fry, B. M.; Chui, M. Y.; Moody, G.; Wong, J. S. S. Interactions between Organic Friction Modifier Additives. *Tribol. Int.* **2020**, *151*, 106438.
- (26) Guegan, J.; Southby, M.; Spikes, H. Friction Modifier Additives, Synergies and Antagonisms. *Tribol. Lett.* **2019**, *67*, 1–12.
- (27) Mansot, J. L.; Hallouis, M.; Martin, J. M. Colloidal Antiwear Additives 2. Tribological Behaviour of Colloidal Additives in Mild Wear Regime. *Colloids Surfaces A Physicochem. Eng. Asp.* **1993**, *75*, 25–31.
- (28) Selezneva, I. E.; Levin, A. Y.; Monin, S. V. Detergent-Dispersant Additives for Motor Oils. Alkylphenolates. *Chem. Technol. Fuels Oils* **1999**, *35*, 389–395.
- (29) Kumar, R.; Kumar Banga, H.; Singh, H.; Kundal, S. An Outline on Modern Day Applications of Solid Lubricants. *Mater. Today Proc.* **2020**, *28*, 1962–1967.
- (30) Li, Y.; Zhou, Z.; He, Y. Solid Lubrication System and Its Plasma Surface Engineering: A Review. *Lubricants* **2023**, *11*.
- (31) Scharf, T. W.; Prasad, S. V. Solid Lubricants: A Review. *J. Mater. Sci.* **2013**, *48*, 511–531.
- (32) Zabinski, J. S.; Donley, M. S.; Prasad, S. V.; McDevitt, N. T. Synthesis and Characterization of Tungsten Disulphide Films Grown by Pulsed-Laser Deposition. *J. Mater. Sci.* **1994**, *29*, 4834–4839.
- (33) Muratore, C.; Bultman, J. E.; Aouadi, S. M.; Voevodin, A. A. In Situ Raman Spectroscopy for Examination of High Temperature Tribological Processes. *Wear* **2011**, *270*, 140–145.
- (34) Felts, J. R.; Oyer, A. J.; Hernández, S. C.; Whitener, K. E.; Robinson, J. T.; Walton, S. G.; Sheehan, P. E. Direct Mechanochemical Cleavage of Functional Groups from Graphene. *Nat. Commun.* **2015**, *6*, 6467.
- (35) Naguib, M.; Kurtoglu, M.; Presser, V.; Lu, J.; Niu, J.; Heon, M.; Hultman, L.; Gogotsi, Y.; Barsoum, M. W. Two-Dimensional Nanocrystals Produced by Exfoliation of Ti₃AlC₂. *Adv. Mater.* **2011**, *23*, 4248–4253.
- (36) Alhabeb, M.; Maleski, K.; Anasori, B.; Lelyukh, P.; Clark, L.; Sin, S.; Gogotsi, Y. Guidelines for Synthesis and Processing of Two-Dimensional Titanium Carbide (Ti₃C₂T_x MXene). *Chem. Mater.* **2017**, *29*, 7633–7644.
- (37) Gogotsi, Y.; Anasori, B. The Rise of MXenes. *ACS Nano* **2019**, *13*, 8491–8494.
- (38) Anasori, B.; Gogotsi, Y. The Global Expansion of MXenes. *Graphene 2D Mater.* **2023**, *8*, 39–41.
- (39) *2D Metal Carbides and Nitrides (MXenes) - Structure, Properties and Applications*, 1st ed.; Babak Anasori, Yury Gogotsi, Eds.; Springer Cham, 2019.
- (40) Majed, A.; Kothakonda, M.; Wang, F.; Tseng, E. N.; Prenger, K.; Zhang, X.; Persson, P. O. Å.; Wei, J.; Sun, J.; Naguib, M. Transition Metal Carbo-Chalcogenide “TMCC:” A New Family of 2D Materials. *Adv. Mater.* **2022**, *34*, 2200574.
- (41) Belay Ibrahim, K.; Ahmed Shifa, T.; Zorzi, S.; Getaye Sendeku, M.; Moretti, E.; Vomiero, A. Emerging 2D Materials beyond Mxenes and TMDs: Transition Metal Carbo-Chalcogenides. *Prog. Mater. Sci.* **2024**, *144*, 101287.
- (42) Ramadanoff, D.; Glass, S. W. High-Altitude Brush Problem. *Trans. Am. Inst. Electr. Eng.* **1944**, *63*, 825–830.

- (43) Chen, Z.; He, X.; Xiao, C.; Kim, S. H. Effect of Humidity on Friction and Wear-A Critical Review. *Lubricants* **2018**, *6*, 74.
- (44) Berman, D.; Deshmukh, S. A.; Sankaranarayanan, S. K. R. S.; Erdemir, A.; Sumant, A. V. Extraordinary Macroscale Wear Resistance of One Atom Thick Graphene Layer. *Adv. Funct. Mater.* **2014**, *24*, 6640–6646.
- (45) Restuccia, P.; Ferrario, M.; Righi, M. C. Monitoring Water and Oxygen Splitting at Graphene Edges and Folds: Insights into the Lubricity of Graphitic Materials. *Carbon N. Y.* **2020**, *156*, 93–103.
- (46) Rajak, D. K.; Kumar, A.; Behera, A.; Menezes, P. L. Diamond-Like Carbon (DLC) Coatings: Classification, Properties, and Applications. *Appl. Sci.* **2021**, *11*, 4445.
- (47) Donnet, C.; Erdemir, A. Solid Lubricant Coatings : Recent Developments and Future Trends. **2004**, *17*, 389–397.
- (48) Ren, Y.; Zhang, L.; Xie, G.; Li, Z.; Chen, H.; Gong, H.; Xu, W.; Guo, D.; Luo, J. A Review on Tribology of Polymer Composite Coatings. **2021**, *9*, 429–470.
- (49) Briscoe, B. J.; Tabor, D. The Effect of Pressure on the Frictional Polymers* Properties Of. **1975**, *34*, 29–38.
- (50) Bahadur, S.; Tabor, D. The Wear of Filled Polytetrafluoroethylene*. **1984**, *98*, 1–13.
- (51) Sawyer, W. G.; Freudenberg, K. D.; Bhimaraj, P.; Schadler, L. S. A Study on the Friction and Wear Behavior of PTFE Filled with Alumina Nanoparticles. **2003**, *254*, 573–580.
- (52) Burris, D. L.; Sawyer, W. G. A Low Friction and Ultra Low Wear Rate PEEK / PTFE Composite. **2006**, *261*, 410–418.
- (53) Brunn, H.; Arnold, G.; Körner, W.; Rippen, G.; Steinhäuser, K. G.; Valentin, I. PFAS : Forever Chemicals — Persistent , Bioaccumulative and Mobile . Reviewing the Status and the Need for Their Phase out and Remediation of Contaminated Sites. *Environ. Sci. Eur.* **2023**, *35*, 1–50.
- (54) Vazirisereshk, M. R.; Martini, A.; Strubbe, D. A.; Baykara, M. Z. Solid Lubrication with MoS₂: A Review. *Lubricants* **2019**, *7*, 57.
- (55) Li, M.; Zhou, Q.; Cao, M.; Zhou, Z.; Liu, X. Nano Materials Science High-Temperature Solid Lubrication Applications of Transition Metal Dichalcogenides (TMDCs) MX₂ : A Review. *Nano Mater. Sci.* **2024**.
- (56) Martin, J. M.; Donnet, C.; Le Mogne, T.; Epicier, T. Superlubricity of Molybdenum Disulphide. *Phys. Rev. B* **1993**, *48*, 10583–10586.
- (57) Kay, E. The Corrosion of Steel in Contact with Molybdenum Disulphide. *Wear* **1968**, *12*, 165–171.
- (58) Prasad, S. V.; Zabinski, J. S. Tribology of Tungsten Disulphide (WS₂): Characterization of Wear-Induced Transfer Films. *J. Mater. Sci. Lett.* **1993**, *12*, 1413–1415.
- (59) Spychalski, W. L.; Pisarek, M.; Szoszkiewicz, R. Microscale Insight into Oxidation of Single MoS₂ Crystals in Air. *J. Phys. Chem. C* **2017**, *121*, 26027–26033.
- (60) Sliney, H. E. Solid Lubricant Materials for High Temperatures-a Review. *Tribol. Int.* **1982**, *15*, 303–315.
- (61) Li, R.; Yang, X.; Zhao, J.; Yue, C.; Wang, Y.; Li, J.; Meyer, E.; Zhang, J.; Shi, Y. Operando Formation of Van Der Waals Heterostructures for Achieving Macroscale Superlubricity on Engineering Rough and Worn Surfaces. *Adv. Funct. Mater.* **2022**, *32*, 1–11.
- (62) Ru, G.; Qi, W.; Tang, K.; Wei, Y.; Xue, T. Interlayer Friction and Superlubricity in Bilayer Graphene and MoS₂/MoSe₂ van Der Waals Heterostructures. *Tribol. Int.* **2020**, *151*, 106483.
- (63) Macknoja, A.; Ayyagari, A.; Zambrano, D.; Rosenkranz, A.; Shevchenko, E. V.; Berman, D. Macroscale Superlubricity Induced by MXene/MoS₂ Nanocomposites on Rough Steel Surfaces under High Contact

Stresses. *ACS Nano* **2023**, *17*, 2421–2430.

- (64) Boidi, G.; Zambrano, D.; Schwarz, S.; Marquis, E.; Varga, M.; Ripoll, R.; Badisch, E.; Clelia, M.; Gachot, C.; Grützmacher, G.; Rosenkranz, A. Solid Lubrication Performance of Hybrid Ti₃C₂T_x/MoS₂ Coatings. *Carbon N. Y.* **2024**, *225*, 119067.
- (65) Grützmacher, P. G.; Cutini, M.; Marquis, E.; Rodríguez Ripoll, M.; Riedl, H.; Kutrowatz, P.; Bug, S.; Hsu, C. J.; Bernardi, J.; Gachot, C.; Erdemir, A.; Righi, M. C. Se Nanopowder Conversion into Lubricious 2D Selenide Layers by Tribochemical Reactions. *Adv. Mater.* **2023**, *35*, 1–10.
- (66) Dadashi Firouzjaei, M.; Karimiziarani, M.; Moradkhani, H.; Elliott, M.; Anasori, B. MXenes: The Two-Dimensional Influencers. *Mater. Today Adv.* **2022**, *13*, 10–13.
- (67) Sokol, M.; Natu, V.; Kota, S.; Barsoum, M. W. On the Chemical Diversity of the MAX Phases. *Trends Chem.* **2019**, *1*, 210–223.
- (68) Wang, X.; Shen, X.; Gao, Y.; Wang, Z.; Yu, R.; Chen, L. Atomic-Scale Recognition of Surface Structure and Intercalation Mechanism of Ti₃C₂X. *J. Am. Chem. Soc.* **2015**, *137*, 2715–2721.
- (69) Amrillah, T.; Abdullah, C. A. C.; Hermawan, A.; Sari, F. N. I.; Alvani, V. N. Towards Greener and More Sustainable Synthesis of MXenes: A Review. *Nanomaterials* **2022**, *12*.
- (70) Anasori, B.; Naguib, M. Two-Dimensional MXenes. *MRS Bull.* **2023**, *48*, 238–244.
- (71) Anasori, B.; Lukatskaya, M. R.; Gogotsi, Y. 2D Metal Carbides and Nitrides (MXenes) for Energy Storage. *Nat. Rev. Mater.* **2017**, *2*.
- (72) Murali, G.; Rawal, J.; Modigunta, J. K. R.; Park, Y. H.; Lee, J. H.; Lee, S. Y.; Park, S. J.; In, I. A Review on MXenes: New-Generation 2D Materials for Supercapacitors. *Sustain. Energy Fuels* **2021**, *5*, 5672–5693.
- (73) Shahzad, F.; Alhabeb, M.; Hatter, C. B.; Anasori, B.; Hong, S. M.; Koo, C. M.; Gogotsi, Y. Electromagnetic Interference Shielding with 2D Transition Metal Carbides (MXenes). *Science (80-.)*. **2016**, *353*, 1137–1140.
- (74) Sun, Y.; Lu, J.; Li, S.; Dai, C.; Zou, D.; Jing, W. MXene-Based Membranes in Water Treatment: Current Status and Future Prospects. *Sep. Purif. Technol.* **2024**, *331*, 125640.
- (75) Khazaei, M.; Ranjbar, A.; Arai, M.; Sasaki, T.; Yunoki, S. Electronic Properties and Applications of MXenes: A Theoretical Review. *J. Mater. Chem. C* **2017**, *5*, 2488–2503.
- (76) Murali, G.; Reddy Modigunta, J. K.; Park, Y. H.; Lee, J. H.; Rawal, J.; Lee, S. Y.; In, I.; Park, S. J. A Review on MXene Synthesis, Stability, and Photocatalytic Applications. *ACS Nano* **2022**, *16*, 13370–13429.
- (77) Huang, H.; Dong, C.; Feng, W.; Wang, Y.; Huang, B.; Chen, Y. Biomedical Engineering of Two-Dimensional MXenes. *Adv. Drug Deliv. Rev.* **2022**, *184*, 114178.
- (78) Chhattal, M.; Rosenkranz, A.; Zaki, S.; Ren, K.; Ghaffar, A.; Gong, Z.; Grützmacher, P. G. Unveiling the Tribological Potential of MXenes-Current Understanding and Future Perspectives. *Adv. Colloid Interface Sci.* **2023**, *321*, 103021.
- (79) Wyatt, B. C.; Rosenkranz, A.; Anasori, B. 2D MXenes: Tunable Mechanical and Tribological Properties. *Adv. Mater.* **2021**, *33*, 1–15.
- (80) Shuck, C. E.; Sarycheva, A.; Anayee, M.; Levitt, A.; Zhu, Y.; Uzun, S.; Balitskiy, V.; Zahorodna, V.; Gogotsi, O.; Gogotsi, Y. Scalable Synthesis of Ti₃C₂T_x MXene. *Adv. Eng. Mater.* **2020**, *22*, 1–8.
- (81) Gogotsi, Y. The Future of MXenes. *Chem. Mater.* **2023**, *35*, 8767–8770.
- (82) Rosenkranz, A.; Righi, M. C.; Sumant, A. V.; Anasori, B.; Mochalin, V. N. Perspectives of 2D MXene Tribology. *Adv. Mater.* **2023**, *35*.
- (83) Lian, W.; Mai, Y.; Liu, C.; Zhang, L.; Li, S.; Jie, X. Two-Dimensional Ti₃C₂ Coating as an Emerging

Protective Solid-Lubricant for Tribology. *Ceram. Int.* **2018**, *44*, 20154–20162.

- (84) Yin, X.; Jin, J.; Chen, X.; Rosenkranz, A.; Luo, J. Ultra-Wear-Resistant MXene-Based Composite Coating via in Situ Formed Nanostructured Tribofilm. *ACS Appl. Mater. Interfaces* **2019**, *11*, 32569–32576.
- (85) Rosenkranz, A.; Grützmacher, P. G.; Espinoza, R.; Fuenzalida, V. M.; Blanco, E.; Escalona, N.; Gracia, F. J.; Villarroel, R.; Guo, L.; Kang, R.; Mücklich, F.; Suarez, S.; Zhang, Z. Multi-Layer Ti₃C₂Tx-Nanoparticles (MXenes) as Solid Lubricants – Role of Surface Terminations and Intercalated Water. *Appl. Surf. Sci.* **2019**, *494*, 13–21.
- (86) Marian, M.; Song, G. C.; Wang, B.; Fuenzalida, V. M.; Krauß, S.; Merle, B.; Tremmel, S.; Wartzack, S.; Yu, J.; Rosenkranz, A. Effective Usage of 2D MXene Nanosheets as Solid Lubricant – Influence of Contact Pressure and Relative Humidity. *Appl. Surf. Sci.* **2020**, *531*, 147311.
- (87) Wait, J.; Josephson, G.; Wyatt, B. C.; Anasori, B.; Çolak, A. Environmentally Stable Nanoscale Superlubricity of Multi-Layered Ti₃C₂Tx MXene. **2023**, 213.
- (88) Rodriguez, A.; Jaman, M. S.; Acikgoz, O.; Wang, B.; Yu, J.; Grützmacher, P. G.; Rosenkranz, A.; Baykara, M. Z. The Potential of Ti₃C₂TX Nano-Sheets (MXenes) for Nanoscale Solid Lubrication Revealed by Friction Force Microscopy. *Appl. Surf. Sci.* **2021**, 535.
- (89) Marian, M.; Tremmel, S.; Wartzack, S.; Song, G.; Wang, B.; Yu, J.; Rosenkranz, A. Mxene Nanosheets as an Emerging Solid Lubricant for Machine Elements – Towards Increased Energy Efficiency and Service Life. *Appl. Surf. Sci.* **2020**, *523*, 146503.
- (90) Marian, M.; Feile, K.; Rothhammer, B.; Bartz, M.; Wartzack, S.; Seynstahl, A.; Tremmel, S.; Krauß, S.; Merle, B.; Böhm, T.; Wang, B.; Wyatt, B. C.; Anasori, B.; Rosenkranz, A. Ti₃C₂Tx Solid Lubricant Coatings in Rolling Bearings with Remarkable Performance beyond State-of-the-Art Materials. *Appl. Mater. Today* **2021**, *25*, 101202.
- (91) Marquis, E.; Cutini, M.; Anasori, B.; Rosenkranz, A.; Righi, M. C. Nanoscale MXene Interlayer and Substrate Adhesion for Lubrication : A Density Functional Theory Study. *ACS Appl. Nano Mater.* **2022**, *5*, 10516–10527.
- (92) Marquis, E.; Benini, F.; Anasori, B.; Rosenkranz, A.; Righi, M. C. Effect of Vacancies and Edges in Promoting Water Chemisorption on Titanium-Based MXenes. *Nano Converge.* **2023**, *10*.
- (93) Boller, H.; Hiebl, K. Quaternary Pseudo-Intercalation Phases Tx [Nb₂S₂C] (TV, Cr, Mn, Fe, Co, Ni, Cu) and Metastable Nb₂S₂C Formed by Topochemical Synthesis. *J. Alloys Compd.* **1992**, *183*, 438–443.
- (94) Beckmann, O.; Boller, H.; Nowotny, H. Die Kristallstrukturen von Ta₂S₂C Und Ti₄S₅ (Ti_{0,81}S). *Monatshefte für Chemie* **1970**, *101*, 945–955.
- (95) Wally, P.; Ueki, M. Tribological Properties of Transition Metal Carbosulfides and Carbosulfide-Metal Composites. *Wear* **1998**, *215*, 98–103.
- (96) Grützmacher, P. G.; Majed, A.; Marquis, E.; Sui, X.; Righi, M. C.; Sauer, M.; Foelske, A.; Naguib, M.; Gachot, C. Transition Metal Carbo Chalcogenides: A Novel Family of 2D Solid Lubricants. *Carbon N. Y.* **2025**, *231*, 119695.
- (97) Iftimie, R.; Minary, P.; Tuckerman, M. E. Ab Initio Molecular Dynamics: Concepts, Recent Developments, and Future Trends. *Proc. Natl. Acad. Sci. U. S. A.* **2005**, *102*, 6654–6659.
- (98) Engel, E.; Dreizler, R. M. *Density Functional Theory - An Advanced Course*; Springer Berlin, Heidelberg, 2011.
- (99) Ustunel, H.; Toffoli, D. Tribology at the Atomic Scale with Density Functional Theory. *Electron. Struct.* **2022**, *4*.
- (100) Hohenberg, P.; Kohn, W. Inhomogeneous Electron Gas. *Phys. Rev.* **1964**, 136.
- (101) Kohn, W.; Sham, L. J. Self-Consistent Equations Including Exchange and Correlation Effects. *Phys. Rev.*

1965, 140, A1133.

- (102) Marzari, N.; Ferretti, A.; Wolverton, C. Electronic-Structure Methods for Materials Design. *Nat. Mater.* **2021**, 20, 736–749.
- (103) Perdew, J. P.; Burke, K.; Ernzerhof, M. Generalized Gradient Approximation Made Simple. *Phys. Rev. Lett.* **1996**, 77, 3865–3868.
- (104) Fatti, G.; Righi, M. C. Selenium Chemisorption Makes Iron Surfaces Slippery. *Tribol. Lett.* **2019**, 67, 1–9.
- (105) Wolloch, M.; Levita, G.; Restuccia, P.; Righi, M. C. Interfacial Charge Density and Its Connection to Adhesion and Frictional Forces. *Phys. Rev. Lett.* **2018**, 121, 26804.
- (106) Tran, N. V.; Tieu, A. K.; Zhu, H.; Ta, H. T. T.; Le, H. M.; Ta, T. D. An Ab Initio Study on the Effects of Na Passivation on Friction Reduction of an Iron Oxide Surface. *J. Appl. Phys.* **2020**, 127.
- (107) Villa, N. S.; Bonoldi, L.; Assanelli, G.; Notari, M.; Lucotti, A.; Tommasini, M.; Cuppen, H. M.; Galimberti, D. R. Digging into the Friction Reduction Mechanism of Organic Friction Modifiers on Steel Surfaces: Chains Packing vs. Molecule–Metal Interactions. *Tribol. Int.* **2024**, 195.
- (108) Villa, N. S.; Serra, G.; Bonoldi, L.; Assanelli, G.; Notari, M.; Lucotti, A.; Tommasini, M. Combining Micro-Infrared Reflection Absorption Spectroscopy with Density Functional Theory for Investigating the Adsorption of Organic Friction Modifiers on Steel Surfaces. *Vib. Spectrosc.* **2022**, 121, 103403.
- (109) Lai, H. E.; Yoo, R. M. S.; Djire, A.; Balbuena, P. B. Investigation of the Vibrational Properties of 2D Titanium Nitride MXene Using DFT. *J. Phys. Chem. C* **2024**, 128, 3327–3342.
- (110) Peng, Q.; Ji, W.; De, S. Mechanical Properties of the Hexagonal Boron Nitride Monolayer: Ab Initio Study. *Comput. Mater. Sci.* **2012**, 56, 11–17.
- (111) Levita, G.; Molinari, E.; Polcar, T.; Righi, M. C. First-Principles Comparative Study on the Interlayer Adhesion and Shear Strength of Transition-Metal Dichalcogenides and Graphene. *Phys. Rev. B - Condens. Matter Mater. Phys.* **2015**, 92, 1–8.
- (112) Wolloch, M.; Losi, G.; Ferrario, M.; Righi, M. C. High-Throughput Screening of the Static Friction and Ideal Cleavage Strength of Solid Interfaces. *Sci. Rep.* **2019**, 9, 1–10.
- (113) Benini, F.; Restuccia, P.; Righi, M. C. Zinc Dialkyldithiophosphates Adsorption and Dissociation on Ferrous Substrates: An Ab Initio Study. *Appl. Surf. Sci.* **2024**, 642, 158419.
- (114) Kohlhauser, B.; Ripoll, M. R.; Riedl, H.; Koller, C. M.; Koutna, N.; Amsüss, A.; Hutter, H.; Ramirez, G.; Gachot, C.; Erdemir, A.; Mayrhofer, P. H. How to Get NoWear? – A New Take on the Design of in-Situ Formed High Performing Low-Friction Tribofilms. *Mater. Des.* **2020**, 190, 108519.
- (115) Benini, F.; Bassoli, N.; Restuccia, P.; Ferrario, M.; Righi, M. C. Interaction of Water and Oxygen Molecules with Phosphorene: An Ab Initio Study. *Molecules* **2023**, 28, 1–13.
- (116) Cutini, M.; Forghieri, G.; Ferrario, M.; Righi, M. C. Adhesion, Friction and Tribochemical Reactions at the Diamond–Silica Interface. *Carbon N. Y.* **2023**, 203, 601–610.
- (117) Guan, Y.; Marquis, E.; Righi, M. C.; Galipaud, J.; Dubreuil, F.; Dufils, J.; Macron, E.; Dassenoy, F.; de Barros Bouchet, M. I. Friction Control by Load-Induced Structure Modification of Overbased Detergent in Fully Formulated Lubricant. *Tribol. Int.* **2024**, 192, 109307.
- (118) Righi, M. C.; Zilibotti, G.; Corni, S.; Ferrario, M.; Bertoni, C. M. First-Principle Molecular Dynamics of Sliding Diamond Surfaces: Tribochemical Reactions with Water and Load Effects. *J. Low Temp. Phys.* **2016**, 185, 174–182.
- (119) Kajita, S.; Pacini, A.; Losi, G.; Kikkawa, N.; Righi, M. C. Accurate Multiscale Simulation of Frictional Interfaces by Quantum Mechanics/Green’s Function Molecular Dynamics. *J. Chem. Theory Comput.* **2023**, 19, 5176–5188.

- (120) Peeters, S.; Losi, G.; Restuccia, P.; Righi, M. C. Unraveling the Mechanism to Form MoS₂ Lubricant Layers from MoDTC by Ab Initio Simulations. *Appl. Surf. Sci.* **2022**, *606*, 154880.
- (121) Long, Y.; Pacini, A.; Ferrario, M.; Van Tran, N.; Peeters, S.; Thiebaut, B.; Loehlé, S.; Martin, J. M.; Righi, M. C.; De Barros Bouchet, M. I. Superlubricity from Mechanochemically Activated Aromatic Molecules of Natural Origin: A New Concept for Green Lubrication. *Carbon N. Y.* **2024**, *228*.
- (122) Pacini, A.; Ferrario, M.; Loehle, S.; Righi, M. C. Advancing Tribological Simulations of Carbon-Based Lubricants with Active Learning and Machine Learning Molecular Dynamics. *Eur. Phys. J. Plus* **2024**, *139*.
- (123) He, J.; Tang, H.; Wang, C. Advances of Molecular Dynamics Simulation in Tribochemistry and Lubrication Investigations: A Review. *J. Ind. Eng. Chem.* **2023**, *126*, 1–19.
- (124) Yin, T.; Wang, G.; Guo, Z.; Pan, Y.; Song, J.; Ding, Q.; Zhao, G. Molecular Dynamics Simulation on Polymer Tribology: A Review. *Lubricants* **2024**, *12*.
- (125) Ta, H. T. T.; Ferrario, M.; Loehlé, S.; Righi, M. C. Ab Initio Informed Machine Learning Potential for Tribochemistry and Mechanochemistry: Application for Eco-Friendly Gallate Lubricant Additive. *Comput. Mater. Today* **2024**, *1*, 100005.
- (126) Yang, J.; Chen, B.; Song, H.; Tang, H.; Li, C. Synthesis, Characterization, and Tribological Properties of Two-Dimensional Ti₃C₂. *Cryst. Res. Technol.* **2014**, *49*, 926–932.
- (127) Zhang, H.; Wang, L.; Chen, Q.; Li, P.; Zhou, A.; Cao, X.; Hu, Q. Preparation, Mechanical and Anti-Friction Performance of MXene/Polymer Composites. *Mater. Des.* **2016**, *92*, 682–689.
- (128) Hope, M. A.; Forse, A. C.; Griffith, K. J.; Lukatskaya, M. R.; Ghidui, M.; Gogotsi, Y.; Grey, C. P. NMR Reveals the Surface Functionalisation of Ti₃C₂ MXene. *Phys. Chem. Chem. Phys.* **2016**, *18*, 5099–5102.
- (129) Harris, K. J.; Bugnet, M.; Naguib, M.; Barsoum, M. W.; Goward, G. R. Direct Measurement of Surface Termination Groups and Their Connectivity in the 2D MXene V₂CT_x Using NMR Spectroscopy. *J. Phys. Chem. C* **2015**, *119*, 13713–13720.
- (130) Persson, I.; Näslund, L. Å.; Halim, J.; Barsoum, M. W.; Darakchieva, V.; Palisaitis, J.; Rosen, J.; Persson, P. O. Å. On the Organization and Thermal Behavior of Functional Groups on Ti₃C₂ MXene Surfaces in Vacuum. *2D Mater.* **2017**, *5*, 015002.
- (131) Seredych, M.; Shuck, C. E.; Pinto, D.; Alhabeab, M.; Precetti, E.; Deysher, G.; Anasori, B.; Kurra, N.; Gogotsi, Y. High-Temperature Behavior and Surface Chemistry of Carbide MXenes Studied by Thermal Analysis. *Chem. Mater.* **2019**, *31*, 3324–3332.
- (132) Hu, T.; Hu, M.; Li, Z.; Zhang, H.; Zhang, C.; Wang, J.; Wang, X. Interlayer Coupling in Two-Dimensional Titanium Carbide MXenes. *Phys. Chem. Chem. Phys.* **2016**, *18*, 20256–20260.
- (133) Zhang, D.; Ashton, M.; Ostadhossein, A.; Van Duin, A. C. T.; Hennig, R. G.; Sinnott, S. B. Computational Study of Low Interlayer Friction in Tin+1C_n (n = 1, 2, and 3) MXene. *ACS Appl. Mater. Interfaces* **2017**, *9*, 34467–34479.
- (134) Zhang, H.; Fu, Z. H.; Legut, D.; Germann, T. C.; Zhang, R. F. Stacking Stability and Sliding Mechanism in Weakly Bonded 2D Transition Metal Carbides by van Der Waals Force. *RSC Adv.* **2017**, *7*, 55912–55919.
- (135) Serles, P.; Hamidinejad, M.; Demingos, P. G.; Ma, L.; Barri, N.; Taylor, H.; Singh, C. V.; Park, C. B.; Filleter, T. Friction of Ti₃C₂T_x MXenes. *Nano Lett.* **2022**.
- (136) Zhang, Y.; Chen, X.; Arramel; Augustine, K. B.; Zhang, P.; Jiang, J.; Wu, Q.; Li, N. Atomic-Scale Superlubricity in Ti₂CO₂@MoS₂ Layered Heterojunctions Interface: A First Principles Calculation Study. *ACS Omega* **2021**, *6*, 9013–9019.
- (137) Cao, F.; Zhang, Y.; Wang, H.; Khan, K.; Tareen, A. K.; Qian, W.; Zhang, H.; Ågren, H. Recent Advances in Oxidation Stable Chemistry of 2D MXenes. *Adv. Mater.* **2022**, *34*.
- (138) Li, X.; Huang, Z.; Zhi, C. Environmental Stability of MXenes as Energy Storage Materials. *Front. Mater.*

2019, 6, 2–10.

- (139) Giannozzi, P.; Baroni, S.; Bonini, N.; Calandra, M.; Car, R.; Cavazzoni, C.; Ceresoli, D.; Chiarotti, G. L.; Cococcioni, M.; Dabo, I.; Dal Corso, A.; De Gironcoli, S.; Fabris, S.; Fratesi, G.; Gebauer, R.; Gerstmann, U.; Gougoussis, C.; Kokalj, A.; Lazzeri, M.; Martin-Samos, L.; Marzari, N.; Mauri, F.; Mazzarello, R.; Paolini, S.; Pasquarello, A.; Paulatto, L.; Sbraccia, C.; Scandolo, S.; Sclauzero, G.; Seitsonen, A. P.; Smogunov, A.; Umari, P.; Wentzcovitch, R. M. QUANTUM ESPRESSO: A Modular and Open-Source Software Project for Quantum Simulations of Materials. *J. Phys. Condens. Matter* **2009**, 21, 395502.
- (140) Giannozzi, P.; Andreussi, O.; Brumme, T.; Bunau, O.; Nardelli, M. B.; Calandra, M.; Car, R.; Cavazzoni, C.; Ceresoli, D.; Cococcioni, M.; others. Advanced Capabilities for Materials Modelling with Quantum ESPRESSO. *J. Phys. Condens. Matter* **2017**, 29, 465901.
- (141) Giannozzi, P.; Baseggio, O.; Bonfà, P.; Brunato, D.; Car, R.; Carnimeo, I.; Cavazzoni, C.; De Gironcoli, S.; Delugas, P.; Ferrari Ruffino, F.; Ferretti, A.; Marzari, N.; Timrov, I.; Urru, A.; Baroni, S. Quantum ESPRESSO toward the Exascale. *J. Chem. Phys.* **2020**, 152, 154105.
- (142) Grimme, S. Semiempirical GGA-Type Density Functional Constructed with a Long-Range Dispersion Correction. *J. Comput. Chem.* **2006**, 27, 1787–1799.
- (143) Monkhorst, H. J.; Pack, J. D. Special Points for Brillouin-Zone Integrations. *Phys. Rev. B* **1976**, 13, 5188.
- (144) Gouveia, J. D.; Gomes, J. R. B. Structural and Energetic Properties of Vacancy Defects in MXene Surfaces. *Phys. Rev. Mater.* **2022**, 6, 024004.
- (145) Sang, X.; Xie, Y.; Lin, M. W.; Alhabeb, M.; Van Aken, K. L.; Gogotsi, Y.; Kent, P. R. C.; Xiao, K.; Unocic, R. R. Atomic Defects in Monolayer Titanium Carbide (Ti₃C₂T_x) MXene. *ACS Nano* **2016**, 10, 9193–9200.
- (146) Karlsson, L. H.; Birch, J.; Halim, J.; Barsoum, M. W.; Persson, P. O. Å. Atomically Resolved Structural and Chemical Investigation of Single MXene Sheets. *Nano Lett.* **2015**, 15, 4955–4960.
- (147) Zhao, S.; Kang, W.; Xue, J. MXene Nanoribbons. **2015**, 2, 879–888.
- (148) Anisimov, V. I.; Zaanen, J.; Andersen, O. K. Band Theory and Mott Insulators: Hubbard U Instead of Stoner I. *Phys. Rev. B* **1991**, 44, 943–954.
- (149) Wang, R. B.; Hellman, A. Initial Water Adsorption on Hematite (α -Fe₂O₃) (0001): A DFT + U Study. *J. Chem. Phys.* **2018**, 148.
- (150) Nguyen, M. T.; Seriani, N.; Gebauer, R. Water Adsorption and Dissociation on α -Fe₂O₃ (0001): PBE+U Calculations. *J. Chem. Phys.* **2013**, 138, 194709.
- (151) Dzade, N. Y.; Roldan, A.; de Leeuw, N. H. A Density Functional Theory Study of the Adsorption of Benzene on Hematite (α -Fe₂O₃) Surfaces. *Minerals* **2014**, 4, 89–115.
- (152) Stirner, T.; Scholz, D.; Sun, J. Convergence of Surface Energy Calculations for Various Methods: (0 0 1), (0 1 2), (1 0 0) Hematite and the Applicability of the Standard Approach. *J. Phys. Condens. Matter* **2020**, 32, 0–5.
- (153) Spencer, M. J. S.; Hung, A.; Snook, I. K.; Yarovsky, I. Density Functional Theory Study of the Relaxation and Energy of Iron Surfaces. *Surf. Sci.* **2002**, 513, 389–398.
- (154) Yu, M.; Trinkle, D. R. Accurate and Efficient Algorithm for Bader Charge Integration. *J. Chem. Phys.* **2011**, 134, 1–8.
- (155) Henkelman, G.; Arnaldsson, A.; Jónsson, H. A Fast and Robust Algorithm for Bader Decomposition of Charge Density. *Comput. Mater. Sci.* **2006**, 36, 354–360.
- (156) Tang, W.; Sanville, E.; Henkelman, G. A Grid-Based Bader Analysis Algorithm without Lattice Bias. *J. Phys. Condens. Matter* **2009**, 21, 084204.
- (157) Sanville, E.; Kenny, S. D.; Smith, R.; Henkelman, G. Improved Grid-Based Algorithm for Bader Charge

Allocation. *J. Comput. Chem.* **2007**, *28*, 899–908.

- (158) Grimme, S.; Antony, J.; Ehrlich, S.; Krieg, H. A Consistent and Accurate Ab Initio Parametrization of Density Functional Dispersion Correction (DFT-D) for the 94 Elements H–Pu. *J. Chem. Phys.* **2010**, *132*, 154104.
- (159) Tkatchenko, A.; Scheffler, M. Accurate Molecular van Der Waals Interactions from Ground-State Electron Density and Free-Atom Reference Data. *Phys. Rev. Lett.* **2009**, *102*, 6–9.
- (160) Tkatchenko, A.; Distasio, R. A.; Car, R.; Scheffler, M. Accurate and Efficient Method for Many-Body van Der Waals Interactions. *Phys. Rev. Lett.* **2012**, *108*, 1–5.
- (161) Steinmann, S. N.; Corminboeuf, C. A Generalized-Gradient Approximation Exchange Hole Model for Dispersion Coefficients. *J. Chem. Phys.* **2011**, *134*, 044117.
- (162) Lee, K.; Murray, É. D.; Kong, L.; Lundqvist, B. I.; Langreth, D. C. Higher-Accuracy van Der Waals Density Functional. *Phys. Rev. B* **2010**, *82*, 081101.
- (163) Sun, J.; Ruzsinszky, A.; Perdew, J. Strongly Constrained and Appropriately Normed Semilocal Density Functional. *Phys. Rev. Lett.* **2015**, *115*, 1–6.
- (164) Kaltak, M.; Klimeš, J.; Kresse, G. Cubic Scaling Algorithm for the Random Phase Approximation: Self-Interstitials and Vacancies in Si. *Phys. Rev. B - Condens. Matter Mater. Phys.* **2014**, *90*, 1–11.
- (165) Usvyat, D.; Maschio, L.; Schütz, M. Periodic Local MP2 Method Employing Orbital Specific Virtuals. *J. Chem. Phys.* **2015**, *143*, 102805.
- (166) Cutini, M.; Maschio, L.; Ugliengo, P. Exfoliation Energy of Layered Materials by DFT-D: Beware of Dispersion! *J. Chem. Theory Comput.* **2020**, *16*, 5244–5252.
- (167) Kresse, G.; Jürgen, F. Efficient Iterative Schemes for Ab Initio Total-Energy Calculations Using a Plane-Wave Basis Set. *Phys. Rev. B* **1996**, *54*, 11169.
- (168) Grimme, S.; Hansen, A.; Brandenburg, J. G.; Bannwarth, C. Dispersion-Corrected Mean-Field Electronic Structure Methods. *Chem. Rev.* **2016**, *116*, 5105–5154.
- (169) Caldeweyher, E.; Mewes, J. M.; Ehlert, S.; Grimme, S. Extension and Evaluation of the D4 London-Dispersion Model for Periodic Systems. *Phys. Chem. Chem. Phys.* **2020**, *22*, 8499–8512.
- (170) Li, Y.; Huang, S.; Wei, C.; Zhou, D.; Li, B.; Wu, C.; Mochalin, V. N. Adhesion between MXenes and Other 2D Materials. *ACS Appl. Mater. Interfaces* **2021**, *13*, 4682–4691.
- (171) Zilibotti, G.; Corni, S.; Righi, M. C. Load-Induced Confinement Activates Diamond Lubrication by Water. *Phys. Rev. Lett.* **2013**, *111*, 1–5.
- (172) Donnet, C.; Martin, J. M.; Le Mogne, T.; Belin, M. The Origin of Super-Low Friction Coefficient of MoS₂ Coatings in Various Environments. *Tribol. Ser.* **1994**, *27*, 277–284.
- (173) Panitz, J. K. G.; Pope, L. E.; Lyons, J. E.; Staley, D. J. Tribological Properties of MoS₂ Coatings in Vacuum, Low Relative Humidity and High Relative Humidity Environments. *J. Vac. Sci. Technol. A* **1988**, *6*, 1166.
- (174) Zhou, H.; Wang, F.; Wang, Y.; Li, C.; Shi, C.; Liu, Y.; Ling, Z. Study on Contact Angles and Surface Energy of MXene Films. *RSC Adv.* **2021**, *11*, 5512–5520.
- (175) Shen, J.; Liu, G.; Ji, Y.; Liu, Q.; Cheng, L.; Guan, K.; Zhang, M.; Liu, G.; Xiong, J.; Yang, J.; Jin, W. 2D MXene Nanofilms with Tunable Gas Transport Channels. *Adv. Funct. Mater.* **2018**, *28*, 1–13.
- (176) Wu, T.; Kent, P. R. C.; Gogotsi, Y.; Jiang, D. E. How Water Attacks MXene. *Chem. Mater.* **2022**, *34*, 4975–4982.
- (177) Lotfi, R.; Naguib, M.; Yilmaz, D. E.; Nanda, J.; Van Duin, A. C. T. A Comparative Study on the Oxidation of Two-Dimensional Ti₃C₂ MXene Structures in Different Environments. *J. Mater. Chem. A* **2018**, *6*, 12733–

12743.

- (178) Yang, Q.; Eder, S. J.; Martini, A.; Grützmacher, P. G. Effect of Surface Termination on the Balance between Friction and Failure of Ti₃C₂T_x MXenes. *npj Mater. Degrad.* **2023**, *7*, 1–8.
- (179) Lipatov, A.; Alhabeb, M.; Lukatskaya, M. R.; Boson, A.; Gogotsi, Y.; Sinitskii, A. Effect of Synthesis on Quality, Electronic Properties and Environmental Stability of Individual Monolayer Ti₃C₂ MXene Flakes. *Adv. Electron. Mater.* **2016**, *2*.
- (180) Habib, T.; Zhao, X.; Shah, S. A.; Chen, Y.; Sun, W.; An, H.; Lutkenhaus, J. L.; Radovic, M.; Green, M. J. Oxidation Stability of Ti₃C₂T_x MXene Nanosheets in Solvents and Composite Films. *npj 2D Mater. Appl.* **2019**, *3*, 1–6.
- (181) Zhang, C. J.; Pinilla, S.; McEvoy, N.; Cullen, C. P.; Anasori, B.; Long, E.; Park, S. H.; Seral-Ascaso, A.; Shmeliov, A.; Krishnan, D.; Morant, C.; Liu, X.; Duesberg, G. S.; Gogotsi, Y.; Nicolosi, V. Oxidation Stability of Colloidal Two-Dimensional Titanium Carbides (MXenes). *Chem. Mater.* **2017**, *29*, 4848–4856.
- (182) Huang, S.; Mochalin, V. N. Hydrolysis of 2D Transition-Metal Carbides (MXenes) in Colloidal Solutions. *Inorg. Chem.* **2019**, *58*, 1958–1966.
- (183) Xia, F.; Lao, J.; Yu, R.; Sang, X.; Luo, J.; Li, Y.; Wu, J. Ambient Oxidation of Ti₃C₂ MXene Initialized by Atomic Defects. *Nanoscale* **2019**, *11*, 23330–23337.
- (184) Feng, A.; Yu, Y.; Jiang, F.; Wang, Y.; Mi, L.; Yu, Y.; Song, L. Fabrication and Thermal Stability of NH₄HF₂-Etched Ti₃C₂ MXene. *Ceram. Int.* **2017**, *43*, 6322–6328.
- (185) Levita, G.; Restuccia, P.; Righi, M. C. Graphene and MoS₂ Interacting with Water: A Comparison by Ab Initio Calculations. *Carbon N. Y.* **2016**, *107*, 878–884.
- (186) Ferrer, S.; Rojo, J. M.; Salmerón, M.; Somorjai, G. A. The Role of Surface Irregularities (Steps, Kinks) and Point Defects on the Chemical Reactivity of Solid Surfaces. *Philos. Mag. A Phys. Condens. Matter, Struct. Defects Mech. Prop.* **1982**, *45*, 261–269.
- (187) Bourikas, K.; Kordulis, C.; Lycourghiotis, A. Titanium Dioxide (Anatase and Rutile): Surface Chemistry, Liquid-Solid Interface Chemistry, and Scientific Synthesis of Supported Catalysts. *Chem. Rev.* **2014**, *114*, 9754–9823.
- (188) Hamraoui, K.; Cristol, S.; Payen, E.; Paul, J. F. Computational Investigation of TiO₂-Supported Isolated Oxomolybdenum Species. *J. Phys. Chem. C* **2007**, *111*, 3963–3972.
- (189) Ghuman, K. K. Mechanistic Insights into Water Adsorption and Dissociation on Amorphous -Based Catalysts. *Sci. Technol. Adv. Mater.* **2018**, *19*, 44–52.
- (190) Doo, S.; Chae, A.; Kim, D.; Oh, T.; Ko, T. Y.; Kim, S. J.; Koh, D. Y.; Koo, C. M. Mechanism and Kinetics of Oxidation Reaction of Aqueous Ti₃C₂T_xSuspensions at Different PHs and Temperatures. *ACS Appl. Mater. Interfaces* **2021**, *13*, 22855–22865.
- (191) Natu, V.; Hart, J. L.; Sokol, M.; Chiang, H.; Taheri, M. L.; Barsoum, M. W. Edge Capping of 2D-MXene Sheets with Polyanionic Salts To Mitigate Oxidation in Aqueous Colloidal Suspensions. *Angew. Chemie* **2019**, *131*, 12785–12790.
- (192) Akinwande, D.; Brennan, C. J.; Bunch, J. S.; Egberts, P.; Felts, J. R.; Gao, H.; Huang, R.; Kim, J.-S.; Li, T.; Li, Y.; Liechti, K. M.; Lu, N.; Park, H. S.; Reed, E. J.; Wang, P.; Yakobson, B. I.; Zhang, T.; Zhang, Y.-W.; Zhou, Y.; Zhu, Y. A Review on Mechanics and Mechanical Properties of 2D Materials—Graphene and Beyond. *Extrem. Mech. Lett.* **2017**, *13*, 42–77.
- (193) Naumis, G. G.; Barraza-Lopez, S.; Oliva-Leyva, M.; Terrones, H. Electronic and Optical Properties of Strained Graphene and Other Strained 2D Materials: A Review. *Reports Prog. Phys.* **2017**, *80*, 096501.
- (194) Zhao, J.; Huang, Y.; He, Y.; Shi, Y. Nanolubricant Additives: A Review. *Friction* **2021**, *9*, 891–917.
- (195) Xiao, H.; Liu, S. 2D Nanomaterials as Lubricant Additive: A Review. *Mater. Des.* **2017**, *135*, 319–332.

- (196) Gao, Q.; Liu, S.; Hou, K.; Li, Z.; Wang, J. Graphene-Based Nanomaterials as Lubricant Additives: A Review. *Lubricants* **2022**, *10*, 273.
- (197) Minami, I. Molecular Science of Lubricant Additives. *Appl. Sci.* **2017**, *7*, 445.
- (198) Boidi, G.; João, J. C.; Profito, F. J.; Rosenkranz, A. Ti₃C₂T_x MXene Nanosheets as Lubricant Additives to Lower Friction under High Loads, Sliding Ratios, and Elevated Temperatures. *ACS Appl. Nano Mater.* **2023**, *6*, 729–737.
- (199) Yan, H.; Cai, M.; Li, W.; Fan, X.; Zhu, M. Amino-Functionalized Ti₃C₂T_x with Anti-Corrosive/Wear Function for Waterborne Epoxy Coating. *J. Mater. Sci. Technol.* **2020**, *54*, 144–159.
- (200) Zhang, H.; Wang, L.; Zhou, A.; Shen, C.; Dai, Y.; Liu, F.; Chen, J.; Li, P.; Hu, Q. Effects of 2-D Transition Metal Carbide Ti₂CT_x on Properties of Epoxy Composites. *RSC Adv.* **2016**, *6*, 87341–87352.
- (201) Grützmacher, P. G.; Suarez, S.; Tolosa, A.; Gachot, C.; Song, G.; Wang, B.; Presser, V.; Mücklich, F.; Anasori, B.; Rosenkranz, A. Erratum: Superior Wear-Resistance of Ti₃C₂T_x Multi-Layer Coatings (ACS Nano (2021) 15:5 (8216–8224) DOI: 10.1021/Acsnano.1c01555). *ACS Nano* **2022**, *16*, 3433.
- (202) Zhang, S.; Ma, T.; Erdemir, A.; Li, Q. Tribology of Two-Dimensional Materials: From Mechanisms to Modulating Strategies. *Mater. Today* **2019**, *26*, 67–86.
- (203) Huang, S.; Mutyala, K. C.; Sumant, A. V.; Mochalin, V. N. Achieving Superlubricity with 2D Transition Metal Carbides (MXenes) and MXene/Graphene Coatings. *Mater. Today Adv.* **2021**, *9*, 100133.
- (204) Rosenkranz, A.; Wang, B.; Zambrano, D.; Henríquez, J. M.; Aguilar-, J. Y.; Marquis, E.; Restuccia, P.; Wyatt, B. C.; Righi, M. C. Solid-Lubrication Performance of Ti₃C₂T_x - Effect of Tribo-Chemistry and Exfoliation. *arxiv version* **2023**.
- (205) Hurtado, J. Y. A.; Grützmacher, P. G.; Henríquez, J. M.; Zambrano, D.; Wang, B.; Rosenkranz, A. Solid Lubrication Performance of Few- and Multilayer Ti₃C₂T_x Coatings. *Adv. Eng. Mater.* **2022**, *24*, 2200755.
- (206) Peeters, S.; Restuccia, P.; Loehlé, S.; Thiebaut, B.; Righi, M. C. Tribochemical Reactions of MoDTC Lubricant Additives with Iron by Quantum Mechanics/Molecular Mechanics Simulations. *J. Phys. Chem. C* **2020**, *124*, 13688–13694.
- (207) Gachot, C.; Hsu, C. J.; Suárez, S.; Grützmacher, P.; Rosenkranz, A.; Stratmann, A.; Jacobs, G. Microstructural and Chemical Characterization of the Tribolayer Formation in Highly Loaded Cylindrical Roller Thrust Bearings. *Lubricants* **2016**, *4*, 1–11.
- (208) Ramirez, G.; Eryilmaz, O. L.; Fatti, G.; Righi, M. C.; Wen, J.; Erdemir, A. Tribochemical Conversion of Methane to Graphene and Other Carbon Nanostructures: Implications for Friction and Wear. *ACS Appl. Nano Mater.* **2020**, *3*, 8060–8067.
- (209) Erdemir, A.; Ramirez, G.; Eryilmaz, O. L.; Narayanan, B.; Liao, Y.; Kamath, G.; Sankaranarayanan, S. K. R. S. Carbon-Based Tribofilms from Lubricating Oils. *Nature* **2016**, *536*, 67–71.
- (210) Wu, Z.; Wang, D.; Sun, A. Preparation of MoS₂ by a Novel Mechanochemical Method. *J. Alloys Compd.* **2010**, *492*, 2009–2011.
- (211) Totolin, V.; Rodríguez Ripoll, M.; Jech, M.; Podgornik, B. Enhanced Tribological Performance of Tungsten Carbide Functionalized Surfaces via In-Situ Formation of Low-Friction Tribofilms. *Tribol. Int.* **2016**, *94*, 269–278.
- (212) Berman, D.; Erdemir, A. Achieving Ultralow Friction and Wear by Tribocatalysis: Enabled by In-Operando Formation of Nanocarbon Films. *ACS Nano* **2021**, *15*, 18865–18879.
- (213) Kohlhauser, B.; Vladu, C. I.; Gachot, C.; Mayrhofer, P. H.; Rodríguez Ripoll, M. Reactive In-Situ Formation and Self-Assembly of MoS₂ Nanoflakes in Carbon Tribofilms for Low Friction. *Mater. Des.* **2021**, *199*, 0–8.
- (214) Lince, J. R.; Loewenthal, S. H.; Clark, C. S. Tribological and Chemical Effects of Long Term Humid Air

Exposure on Sputter-Deposited Nanocomposite MoS₂ Coatings. *Wear* **2019**, 432–433.

- (215) Liu, H.; Yang, B.; Wang, C.; Han, Y.; Liu, D. The Mechanisms and Applications of Friction Energy Dissipation. *Friction* **2023**, 11, 839–864.
- (216) Vazirisereshk, M. R.; Hasz, K.; Zhao, M. Q.; Johnson, A. T. C.; Carpick, R. W.; Martini, A. Nanoscale Friction Behavior of Transition-Metal Dichalcogenides: Role of the Chalcogenide. *ACS Nano* **2020**, 14, 16013–16021.
- (217) Li, H.; Wang, J.; Gao, S.; Chen, Q.; Peng, L.; Liu, K.; Wei, X. Superlubricity between MoS₂ Monolayers. *Adv. Mater.* **2017**, 29, 2–7.
- (218) Khare, H. S.; Burris, D. L. Surface and Subsurface Contributions of Oxidation and Moisture to Room Temperature Friction of Molybdenum Disulfide. *Tribol. Lett.* **2014**, 53, 329–336.
- (219) Levita, G.; Righi, M. C. Effects of Water Intercalation and Tribochemistry on MoS₂ Lubricity: An Ab Initio Molecular Dynamics Investigation. *ChemPhysChem* **2017**, 18, 1475–1480.
- (220) Polcar, T.; Gustavsson, F.; Thersleff, T.; Jacobson, S.; Cavaleiro, A. Complex Frictional Analysis of Self-Lubricant W-S-C/Cr Coating. *Faraday Discuss.* **2012**, 156, 383–401.
- (221) Babuska, T. F.; Pitenis, A. A.; Jones, M. R.; Nation, B. L.; Sawyer, W. G.; Argibay, N. Temperature-Dependent Friction and Wear Behavior of PTFE and MoS₂. *Tribol. Lett.* **2016**, 63, 1–7.
- (222) Wahl, K. J.; Dunn, D. N.; Singer, I. L. Wear Behavior of Pb-Mo-S Solid Lubricating Coatings. *Wear* **1999**, 230, 175–183.
- (223) Hebbar Kannur, K.; Huminiuc, T.; Yaqub, T. Bin; Polcar, T.; Pupier, C.; Héau, C.; Cavaleiro, A. An Insight on the MoS₂ Tribo-Film Formation to Determine the Friction Performance of Mo-S-N Sputtered Coatings. *Surf. Coatings Technol.* **2021**, 408.
- (224) Morita, Y.; Onodera, T.; Suzuki, A.; Sahnoun, R.; Koyama, M.; Tsuboi, H.; Hatakeyama, N.; Endou, A.; Takaba, H.; Kubo, M.; Del Carpio, C. A.; Shin-yoshi, T.; Nishino, N.; Suzuki, A.; Miyamoto, A. Development of a New Molecular Dynamics Method for Tribochemical Reaction and Its Application to Formation Dynamics of MoS₂ Tribofilm. *Appl. Surf. Sci.* **2008**, 254, 7618–7621.
- (225) Nicolini, P.; Capozza, R.; Restuccia, P.; Polcar, T. Structural Ordering of Molybdenum Disulfide Studied via Reactive Molecular Dynamics Simulations. *ACS Appl. Mater. Interfaces* **2018**, 10, 8937–8946.
- (226) Zhou, M.; Andrews, L. Infrared Spectra and Density Functional Calculations of the CrO₂⁻, MoO₂⁻, and WO₂⁻ Molecular Anions in Solid Neon. *J. Chem. Phys.* **1999**, 111, 4230–4238.
- (227) Blau, P. J. On the Nature of Running-In. *Tribol. Int.* **2005**, 38, 1007–1012.
- (228) Baltrusaitis, J.; Mendoza-Sanchez, B.; Fernandez, V.; Veenstra, R.; Dukstiene, N.; Roberts, A.; Fairley, N. Generalized Molybdenum Oxide Surface Chemical State XPS Determination via Informed Amorphous Sample Model. *Appl. Surf. Sci.* **2015**, 326, 151–161.
- (229) Divya, S.; Johnston, J. H.; Nann, T. Molybdenum Dichalcogenide Cathodes for Aluminum-Ion Batteries. *Energy Technol.* **2020**, 8, 1–9.
- (230) Truong, Q. D.; Kempaiah Devaraju, M.; Nakayasu, Y.; Tamura, N.; Sasaki, Y.; Tomai, T.; Honma, I. Exfoliated MoS₂ and MoSe₂ Nanosheets by a Supercritical Fluid Process for a Hybrid Mg-Li-Ion Battery. *ACS Omega* **2017**, 2, 2360–2367.
- (231) Miakota, D. I.; Unocic, R. R.; Bertoldo, F.; Ghimire, G.; Engberg, S.; Geohegan, D.; Thygesen, K. S.; Canulescu, S. A Facile Strategy for the Growth of High-Quality Tungsten Disulfide Crystals Mediated by Oxygen-Deficient Oxide Precursors. *Nanoscale* **2022**, 14, 9485–9497.
- (232) Li, W.; Hu, L.; Wang, M.; Tang, H.; Li, C.; Liang, J.; Jin, Y.; Li, D. Synthesis and Tribological Properties of Mo-Doped WSe₂ Nanolamellars. *Cryst. Res. Technol.* **2012**, 47, 876–881.

- (233) Zazpe, R.; Charvot, J.; Krumpolec, R.; Hromádka, L.; Pavlíňák, D.; Dvorak, F.; Knotek, P.; Michalicka, J.; Přikryl, J.; Ng, S.; Jelínková, V.; Bureš, F.; Macak, J. M. Atomic Layer Deposition of MoSe₂ Using New Selenium Precursors. *FlatChem* **2020**, *21*, 100166.
- (234) Reguzzoni, M.; Righi, M. C. Size Dependence of Static Friction between Solid Clusters and Substrates. *Phys. Rev. B - Condens. Matter Mater. Phys.* **2012**, *85*, 201412.
- (235) Berman, D.; Erdemir, A.; Sumant, A. V. Approaches for Achieving Superlubricity in Two-Dimensional Materials. *ACS Nano* **2018**, *12*, 2122–2137.
- (236) Zaharin, H. A.; Ghazali, M. J.; Thachnatharen, N.; Ezzah, F.; Walvekar, R.; Khalid, M. Progress in 2D Materials Based Nanolubricants: A Review. *FlatChem* **2023**, *38*, 100485.
- (237) Guo, Y.; Zhou, X.; Lee, K.; Yoon, H. C.; Xu, Q.; Wang, D. Recent Development in Friction of 2D Materials: From Mechanisms to Applications. *Nanotechnology* **2021**, *32*, 312002.
- (238) Jeffrey R. Lince. Effective Application of Solid Lubricants in Spacecraft Mechanisms. *Lubricants* **2020**, *8*, 74.
- (239) Wang, G.; Hou, H.; Yan, Y.; Jagatramka, R.; Shirsalimian, A.; Wang, Y.; Li, B.; Daly, M.; Cao, C. Recent Advances in the Mechanics of 2D Materials. *Int. J. Extrem. Manuf.* **2023**, *5*, 032002.
- (240) Wait, J.; Josephson, G.; Wyatt, B. C.; Anasori, B.; Çolak, A. Environmentally Stable Nanoscale Superlubricity of Multi-Layered Ti₃C₂T_x MXene. *Carbon N. Y.* **2023**, *213*, 118284.
- (241) Li, Y.; Huang, S.; Wei, C.; Zhou, D.; Li, B.; Mochalin, V. N.; Wu, C. Friction between MXenes and Other Two-Dimensional Materials at the Nanoscale. *Carbon N. Y.* **2022**, *196*, 774–782.
- (242) Aouadi, S. M.; Gao, H.; Martini, A.; Scharf, T. W.; Muratore, C. Lubricious Oxide Coatings for Extreme Temperature Applications: A Review. *Surf. Coatings Technol.* **2014**, *257*, 266–277.
- (243) Maclucas, T.; Daut, L.; Grützmacher, P.; Guitar, M. A.; Presser, V.; Gachot, C.; Suarez, S.; Mücklich, F. Influence of Structural Depth of Laser-Patterned Steel Surfaces on the Solid Lubricity of Carbon Nanoparticle Coatings. *Friction* **2023**, *11*, 1276–1291.
- (244) Shirley, D. A. High-Resolution x-Ray Photoemission Spectrum of the Valence Bands of Gold. *Phys. Rev. B* **1972**, *5*, 4709–4714.
- (245) Tougaard, S. Universality Classes of Inelastic Electron Scattering Cross-Sections. *Surf. Interface Anal.* **1997**, *25*, 137–154.
- (246) Wagner, C. D. Sensitivity Factors for XPS Analysis of Surface Atoms. *J. Electron Spectros. Relat. Phenomena* **1983**, *32*, 99–102.
- (247) Terwisscha-Dekker, H.; Hogenelst, T.; Bliem, R.; Weber, B.; Bonn, D. Why Teflon Is so Slippery While Other Polymers Are Not. *Phys. Rev. E* **2023**, *107*, 24801.
- (248) Zilibotti, G.; Righi, M. C. Ab Initio Calculation of the Adhesion and Ideal Shear Strength of Planar Diamond Interfaces with Different Atomic Structure and Hydrogen Coverage. *Langmuir* **2011**, *27*, 6862–6867.
- (249) Grützmacher, P. G.; Schranz, M.; Hsu, C. J.; Bernardi, J.; Steiger-Thirsfeld, A.; Hensgen, L.; Rodríguez Ripoll, M.; Gachot, C. Solid Lubricity of WS₂ and Bi₂S₃ Coatings Deposited by Plasma Spraying and Air Spraying. *Surf. Coatings Technol.* **2022**, *446*, 128772.
- (250) Zhou, M.; Tong, R.; Zhang, T.; Liu, G. Application of MoS₂ in the Space Environment: A Review. *Front. Mech. Eng.* **2023**, *18*, 1–31.
- (251) Shi, J.; Ma, G.; Han, C.; Li, G.; Liu, Y.; Liu, Q. Tribological Properties and Bearing Application of Mo-Based Films in Space Environment. *Vacuum* **2021**, *188*, 110217.